Device physics on single-layer organic light-emitting diodes (OLEDs) with wide bandgap emitters

Dissertation

Zur Erlangung des Grades

“Doktor der Naturwissenschaften”

am Fachbereich Chemie, Pharmazie, Geographie und Geowissenschaften der

Johannes Gutenberg-Universität in Mainz

Xiao Tan

Geboren in Anhui, China

Mainz, 2024

Affidavit

I hereby declare that I completed the dissertation independently and without any external support. Except for the places mentioned and referenced in the thesis, no external sources were used.

Furthermore, I confirm that this thesis has not yet been submitted as part of another examination process neither in identical nor in similar form.

Ort, Datum: Unterschrift

Abstract

Organic light-emitting diodes (OLEDs) are widely used in display technology. Achieving a full-color display necessitates blue OLEDs to complement red and green primary colors. However, blue OLEDs pose a significant challenge due to the higher energy gap of the emitter, making them more susceptible to impurities such as oxygen molecules. These impurities form traps for charge transport, leading to significant electrical losses as energy is converted to heat instead of light, a phenomenon known as charge trapping. This issue is prevalent in OLEDs with wide bandgap emitters, reducing their efficiency.

While complex and costly multilayer device layouts can partly address this problem, there is increasing interest in single-layer OLEDs with blue emission, due to their compatibility with solution processing (only one emissive layer sandwiched by two electrodes). This simplicity imposes stringent requirements on the development of materials and device configurations. This thesis aims to understand charge trapping in single-layer OLEDs, particularly those with wide bandgap (>2.4 eV) emitters, and proposes three strategies from material design to device engineering to enhance blue OLED performance.

From the material perspective, chapter 2 investigates a new class of thermally activated delayed fluorescence (TADF) emitters to address charge trapping. These emitters consist of carbazole units for hole transport and triazine units for electron transport. By varying the chemical structure, a special molecular arrangement is achieved where triazine shows π-π stacking preference, and carbazole shields the electron-conducting core from potential impurities like oxygen molecules. Consequently, these new TADF emitters avoid losses due to electron trapping by impurities, resulting in efficient electron transport, which holds great potential for single-layer blue OLEDs.

From the device perspective, chapter 3 proposes an inverted device architecture to improve the efficiency of single-layer OLEDs with imbalanced charge transport. Many wide bandgap TADF emitters exhibit trap-limited electron transport, leading to hole-dominated characteristics and light emission occurring close to the metallic cathode, thereby enabling photon absorption by the metal. For these emitters, an inverted single-layer device architecture with ohmic bottom-electron and top-hole contacts shifts the emission zone away from the metal top electrode, thereby more than doubling the optical outcoupling efficiency. This architecture achieved a high external quantum efficiency (EQE) of 19% in inverted single-layer OLEDs with blue emission, demonstrating that balanced charge transport is not a prerequisite for highly efficient single-layer OLEDs.

From the emissive layer perspective, chapter 4 presents an efficient blue single-layer OLED without using high-triplet-energy materials, which are typically employed to confine triplet excitons to the emitter but can compromise charge transport and stability. By incorporating a narrow-band terminal emitter in a blue TADF emitter with hole-dominated transport, charge balance is manipulated by the hole-trapping effect arising from the ionization energy offset between the TADF sensitizer and the terminal emitter. As such, electron-dominated OLEDs can be created, where the terminal emitter ensures narrow-band blue emission via energy transfer. These single-layer hyperfluorescent OLEDs achieved an EQE of 21.1% with pure blue emission and minimal efficiency roll-off. The results demonstrate the feasibility of efficient pure-blue single-layer OLEDs without auxiliary high-triplet-energy materials, featuring a simple design and enhanced operational stability.

Zusammenfassung

Organische Leuchtdioden (OLEDs) werden häufig in der Display-Technologie eingesetzt. Um ein vollfarbiges Display zu erreichen, sind blaue OLEDs erforderlich, die die Primärfarben Rot und Grün ergänzen. Blaue OLEDs stellen jedoch eine erhebliche Herausforderung dar, da die Emitter eine höhere Energielücke aufweisen müssen was sie anfälliger für Verunreinigungen durch Sauerstoff macht. Diese Verunreinigungen bilden Fallen für die Ladungsträger, was zu erheblichen elektrischen Verlusten führt. Die in den Fallen gefangen Ladungsträger können nicht mehr in Licht umgewandelt werden, und verringern somit die Effizienz der OLED Dieses Phänomen ist als Ladungsfalle bekannt und tritt häufig bei OLEDs mit Emittern mit großer Energielücke auf.

Obwohl komplexe und kostspielige Mehrschichtige Layouts für OLEDs dieses Problem teilweise lösen können, besteht ein wachsendes Interesse an einlagigen OLEDs mit blauer Emission. Der Vorteil einlagiger OLEDs ist die Möglichkeit, den Emitter, der zwischen zwei Elektroden eingeschlossen wird, aus Lösung zu prozessieren. Das einfache Design der OLED stellt strenge Anforderungen an die verwendeten Emitter und das Design der OLED. Diese Dissertation zielt darauf ab, Ladungsfallen in einlagigen OLEDs, insbesondere solchen mit Emittern mit großer Energielücke (>2,4 eV), zu verstehen und schlägt drei Strategien vor, um die Effizienz von blauen OLEDs durch Materialdesign und Geräteentwicklung zu verbessern.

In Kapitel 2 wird eine neue Klasse von Emittern untersucht, welche eine thermisch aktivierte verzögerte Fluoreszenz (TADF) zeigen und dabei die Anzahl der Ladungsfallen reduzieren. Diese Emitter bestehen aus Carbazoleinheiten für den Lochtransport und Triazineinheiten für den Elektronentransport. Durch Variation der chemischen Struktur wird eine spezielle molekulare Anordnung erreicht, bei der Triazin eine Präferenz für π-π-Stapelung zeigt und Carbazol den elektronenleitenden Kern vor möglichen Verunreinigungen wie Sauerstoffmolekülen abschirmt. Folglich vermeiden diese neuen TADF-Emitter Verluste durch Elektronenfallen aufgrund von Verunreinigungen und ermöglichen einen effizienten Elektronentransport, was großes Potenzial für einlagige blaue OLEDs bietet.

Um einlagige und effiziente OLEDs mit Emittern herzustellen, welche einen unausgeglichenen Ladungstransport haben, wird eine invertierte Struktur von OLEDs vorgeschlagen, wie sie in Kapitel 3 vorgestellt wird. Viele TADF-Emitter mit großer Energielücke zeigen transportbegrenzten Elektronentransport, was zu lochdominierten Ladungstransport führt und zu einer Lichtemission nahe an der metallischen Kathode führt, wodurch Photonen vom Metall absorbiert werden können. Für diese Emitter verschiebt eine invertierte einlagige OLED-Architektur mit ohmschen Kontakten die Emissionszone von der Metalloberelektrode weg, wodurch die optische Auskopplungseffizienz mehr als verdoppelt wird. Diese Architektur erreichte eine hohe externe Quanteneffizienz (EQE) von 19% in invertierten einlagigen OLEDs mit blauer Emission und zeigt, dass ein ausgeglichener Ladungstransport keine Voraussetzung für hocheffiziente einlagige OLEDs ist.

Aus der Perspektive der Emissionsschicht präsentiert Kapitel 4 eine effiziente, blaue, einlagige OLED ohne die Verwendung von Materialien mit hoher Triplett-Energie. Solche werden typischerweise eingesetzt, um Triplett-Exzitonen im Emitter zu halten, aber den Ladungstransport und die Stabilität beeinträchtigen können. Durch die Mischung eines schmalbandigen terminalen Emitters in einen blauen

TADF-Emitter mit lochdominiertem Transport wird das Ladungsgleichgewicht durch den Lochfalleneffekt manipuliert. Dieser ergibt sich aus dem Unterschied zwischen den Ionisierungsenergien des TADF-Emitter und dem terminalen Emitter.Auf diese Weise können elektronendominierte OLEDs hergestellt werden, bei denen der terminale Emitter eine schmalbandige blaue Emission durch Energietransfer sicherstellt. Diese einlagigen hyperfluoreszenten OLEDs erreichten eine EQE von 21,1% mit reiner blauer Emission und minimalem Effizienzabfall. Die Ergebnisse demonstrieren die Machbarkeit effizienter, rein blauer einlagiger OLEDs ohne zusätzliche Materialien mit hoher Triplett-Energie, die ein einfaches Design und eine verbesserte Betriebsstabilität aufweisen.

Contents

1. Introduction

Organic electronic devices[1,2], in the form of numerous commercial products, have been integrated into our daily life over last a few years, playing a crucial role in supporting the development of various technologies. For instance, organic photovoltaics contribute to green energy initiatives[3–5], organic transistors enable the creation of self-healing electronic skins[6,7], and organic light-emitting devices facilitate the production of foldable displays for smartphones[8]. Among these diverse applications, significant research efforts have been devoted to the study of organic light-emitting diodes (OLEDs), encompassing both fundamental physics and materials science.

The OLED story began in 1963, when the first direct-current driven OLED was fabricated by Pope et al[9]. They used crystalline anthracene as an emitter, observing electroluminescence at 400 volts during operation. Another important milestone occurred in 1987, when Tang and VanSlyke introduced the first-ever evaporated small molecule OLED, laying the groundwork for the commercialization of OLEDs[10]. A significant breakthrough occurred in 1990 with the introduction of conjugated polymers to OLEDs, enlightening their great potential for flexible applications[11]. As research continues to advance, so does our understanding of OLEDs in terms of charge transport, light extraction, and photophysical studies. These developments have led to more stable and improved OLED device performance[12].

Efforts in OLED materials research are motivated by the goal of achieving higher efficiency, longer lifetime, and gaining a better understanding of the underlying physics[13]. Initially, electroluminescence was associated with fluorescent materials, which had a limited internal quantum efficiency (IQE) of up to 25%, due to spin statistics. However, in 1998, a groundbreaking discovery revealed that emitters containing heavy metals could achieve 100% IQE through phosphorescence[14,15]. The utilization of high-efficiency emitters, coupled with advancements in thermal evaporation technology, significantly boosted the commercialization of OLEDs. By 2012, the third generation of OLED materials demonstrated 100% IQE without the need for additional heavy metal dopants[16,17]. This achievement was enabled by the design of molecular structures that exhibit thermally activated delayed fluorescence (TADF). TADF materials are also considered promising alternatives for OLED applications[18]. In addition to improving colorful emitters, scientists are also exploring related functional materials such as electrodes, or facilitate the injection, transport, and blocking of charge carriers.

This chapter introduces the basic concepts of organic semiconductors emphasizing on OLEDs. Device physics and material developments will be explained systematically to provide an overarching perspective.

1.1 Organic semiconductors

Semiconductors represent a class of materials characterized by tunable conductivity between that of a conductor and an insulator, achieved through energy excitation in the energy gap. These materials exhibit variable characteristics when subjected to an electrical field, light, and other stimuli, making them indispensable in various devices such as solar cells, LEDs, and field-effect transistors (FETs). Initially, semiconducting properties were predominantly observed in inorganic materials, with rapid advancements seen in materials like silicon, germanium, and gallium arsenide. Silicon remains the most widely used material in commercial electronics. In inorganic semiconductors, atoms form a lattice structure with covalent or ionic bonds, facilitating electron delocalization across the entire lattice, thereby resulting in high conductivity. However, due to the inherent rigidity of inorganic materials and the high production costs associated with industry applications, organic semiconductors have emerged as a viable alternative. The discovery of photoconductivity and electroluminescence in organic crystals during the 1960s sparked significant interest in organic semiconductors[9,19–21]. Subsequently, the synthesis of the first amorphous organic semiconductor film in 1974 further propelled research in this field[22].

1.1.1 Conjugation

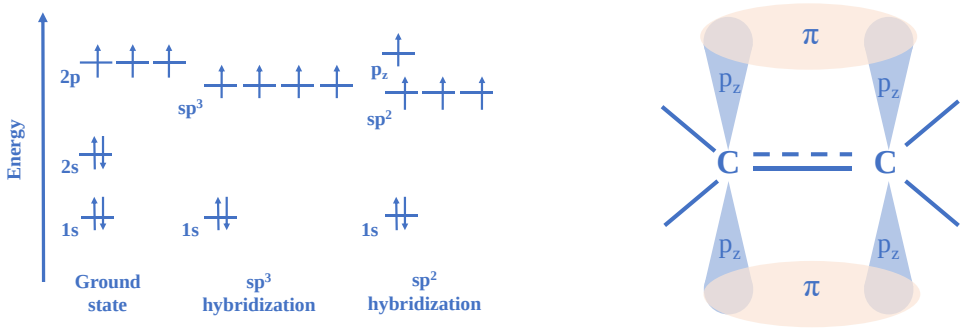

Figure 1.1: Hybridization processes in carbon atom. a) Energy level of ground state, sp^2 and sp^3 hybridized orbitals and b) Formation of σ (solid line) and π (dashed line) bonds in an ethene molecule.

Conjugation occurs when one p orbital overlaps with another p orbital on an adjacent σ bond. For instance, in **Figure 1.1**, in a carbon atom forming four single bonds, the valence-shell s orbital combines with three valence-shell p orbitals to form four equivalent sp^3 hybrid orbitals. These orbitals arrange themselves tetrahedrally around the carbon atom to bond with four different atoms. When a carbon atom forms a double bond, the valence-shell s orbital combines with two valence-shell p orbitals to form three equivalent sp^2 hybrid orbitals. These orbitals arrange themselves in a triangular planar arrangement, leaving one unhybridized valence-shell p orbital, which is known as the p_z orbital. The p_z orbital lies perpendicular to the plane formed by the sp^2 orbitals. The p_z orbital with the highest energy can overlap with another nearby p_z orbital, forming a π-bond.

The hybrid orbitals of carbon atoms possess identical energy levels and engage in strong σ-bond formation with neighboring atoms, such as in C-C and C-H bonds, leading to significant electron localization owing to extensive orbital overlap. Conversely, in the formation of π-bonds using p_z orbitals, there is comparatively less overlap and weaker interaction, resulting in the delocalization of π-electrons

across aligned p orbitals of adjacent atoms. Consequently, in carbon atoms interconnected by alternating single and double bonds, all π-electrons are shared, thereby contributing to the semiconducting properties exhibited by the material.

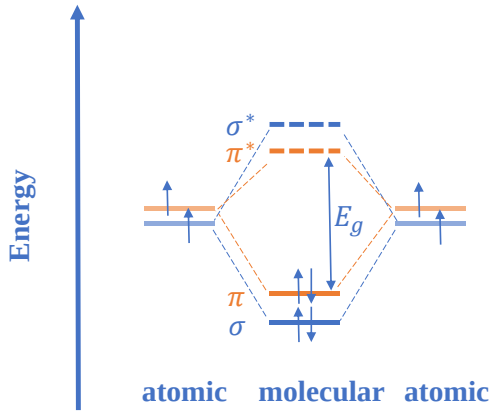

Figure 1.2: Bonding between two carbon atoms in ethene depicted in an energy level diagram, arrows represent the electrons with different spin magnetic quantum numbers (m_s = +1/2, -1/2). Modified from reference[23].

Organic semiconductors are mainly composed of carbon and hydrogen atoms, although sometimes fluorine, boron, silicon, etc. are also incorporated as heteroatoms. These organic materials possess semiconducting properties mainly due to their carbon-based conjugated structure, regardless of whether they are in the form of small molecules or polymers. Depending on their conjugation length, organic semiconductors enable the delocalization of electron wave functions to adjacent molecules or polymer branches, driven by van der Waals forces bonding in the solid state.

When discussing bond formation between atoms, molecular orbital theory commonly distinguishes between two types of orbitals. Bonding orbitals maintain the electron density concentrated between two nuclei, holding them together, whereas anti-bonding orbitals simultaneously concentrate electron vacancies (resulting from electron transfer), thereby exerting a pull on each nucleus away from the other and consequently weakening the bond[23,24]. In **Figure 1.2**, the molecular orbitals are depicted as a distribution of energy, with electrons arranged in accordance with Pauli's exclusion principle. In the ground state, electron pairs occupy energy levels akin to a staircase until the frontier orbital is filled; this orbital is known as the highest occupied molecular orbital (HOMO), often composed of π orbitals in organic semiconductors. Subsequently, the next unfilled orbital possessing higher energy is termed the lowest unoccupied molecular orbital (LUMO), often comprising π^* orbitals. The narrow bands are formed between neighboring molecules due to the weak Van der Walls' forces, thus the HOMO and LUMO levels of organic semiconductors can be considered as quasi-continuous bands corresponding to the valence band and the conduction band of inorganic semiconductors, though energy levels of each molecule in the same layer are discrete and slightly different. The energy difference defines the energy band gap. Additionally, mention is often made of the optical bandgap E_g,[24] which is an optical π-π* transition and can be experimentally determined from the onset value of the absorption spectrum, typically exhibiting a difference of approximately the exciton binding energy (~0.4 eV) as compared to the electrical bandgap[25].

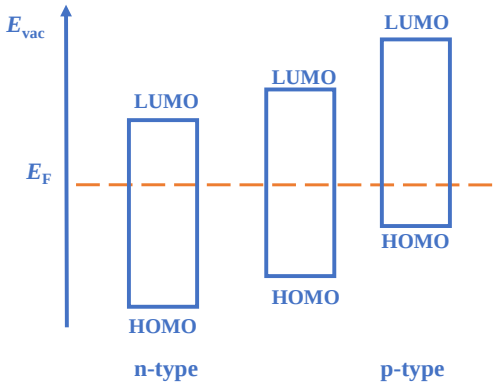

Figure 1.3: Band structure figures of different semiconductors.

According to band structure theory in solid-state physics, the Fermi energy level (E_F) represents a theoretical energy level close to in the middle of the bandgap for an intrinsic undoped semiconductor, indicating the thermodynamic equilibrium with a 50% probability of being occupied by electrons. The value of E_F represents the maximum energy of the states that an electron can occupy at $T = 0$ K, and the work function (WF) of a metal is defined by the energy difference between the E_F and vacuum energy level (E_{vac}). Organic semiconductors that are doped with an electron donor possess a conduction band positioned close to E_F and exhibit a preference (>50%) for electron occupancy, such materials are classified as n-type semiconductors. Conversely, the valence band of organic semiconductors is in close proximity to E_F when doped with an acceptor and displays a preference (>50%) for hole occupancy, these materials are categorized as p-type semiconductors as shown in **Figure 1.3**.

An advantage of organic semiconductors lies in their tunable bandgap, which can be adjusted within a range of 1 to 4 eV through modifications in their chemical structure. By increasing the length of conjugation, the energy difference between π and π*-orbitals is lowered due to the quantum size effect, thereby narrowing the bandgap of organic semiconductors. This phenomenon is applicable to both small molecules and polymers, enabling the realization of desirable characteristics across a wide range of wavelengths. For most organic semiconductors, local variations in energy levels arise due to diverse surroundings within amorphous structures[23,24,26], such as kinks and defects in polymers, or molecular packing arrangements. These variations can be effectively described by a Gaussian distribution. Further elaboration on this topic will be provided in the charge transport section.

1.1.2 Charge transport model

A fundamental distinction exists in the charge transport mechanisms between organic and inorganic semiconductors. Inorganic semiconductors typically exhibit classical crystal structures, whereas organic semiconductors are well-recognized for their amorphous states[27]. Notably, the charge transport characteristics of organic semiconductors display significant variability due to diverse chemical structures[28,29]. Even within a pristine film, the packing preference of small molecules induces energetic disorder resulting in a broadening of the density of states (DOS), commonly referred to as "static disorder," which pertains to the morphological disorder in the microenvironment of organic semiconductors[30,31].

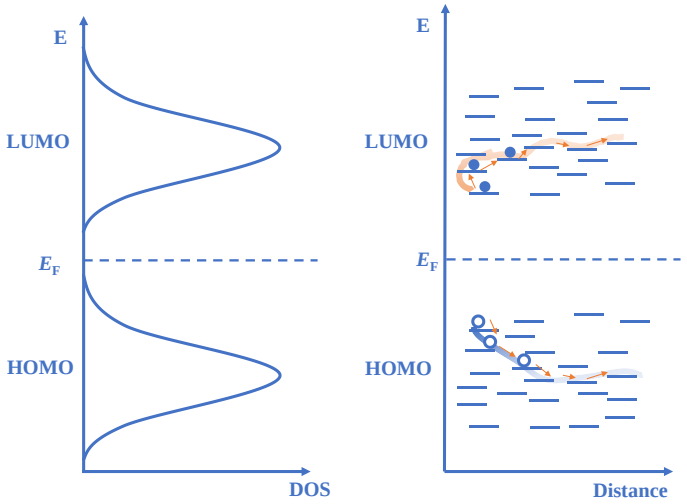

Figure 1.4: The Gaussian disorder model. Left shows the Gaussian distribution of HOMO and LUMO energy levels and right shows the hopping process among charge transport sites.

Consequently, the conventional description of valence and conduction bands becomes inadequate. To capture the intrinsic random energetic disorder of transporting sites in organic semiconductors, a Gaussian distribution is specifically selected as shown in **Figure 1.4**. This choice is made considering that the coupling between a charge carrier and induced dipoles or a random distribution of static disorder leads to a Gaussian DOS function, as proposed by Bässler et al.[30]. Here, the energetic variations, and the DOS $g(\varepsilon)$ is represented by

$$g(\varepsilon) = \frac{N_C}{(2\pi\sigma)^2}\exp\left(-\frac{\varepsilon^2}{2\sigma^2}\right) \tag{1.1}$$

Where N_C represents the total number of conducting states, σ denotes the width of the Gaussian DOS and ε signifies energy.

Given the relatively weak van der Waals interactions between organic molecules, the charge carrier's mean free path is much shorter due the absence of a broad bandwidth in organic semiconductors, meaning the carriers are localized in specific states[12]. A wave-function overlap is required to transport carriers from individual localized sites. To overcome the energy barrier between these sites, carriers emit or absorb phonons, known as phonon-assisted hopping process. A single-phonon jump rate description was proposed by Miller and Abrahams[32]:

$$W_{ij} = \nu_0 \exp(-2\alpha R_{ij}) \begin{cases} \exp\left(-\dfrac{\varepsilon_j - \varepsilon_i}{k_B T}\right), & \varepsilon_j \geq \varepsilon_i \\ 1 \quad , & \varepsilon_j \geq \varepsilon_i \end{cases} \tag{1.2}$$

The hopping rate from occupied site *i* to unoccupied site *j* depends on the energetic difference and spatial distance, where ν_0 is the attempt-to-hop frequency. The first exponential term accounts for the tunneling probability, signifying the decrease of wave function overlap as the distance between two sites increases. The second term accounts for the temperature dependence of the phonon density, which is related to the

hopping upward in energy, whereas the hopping rate remains constant when hopping downward in energy.

In general, while the hopping rate is used to describe the hopping probability, it is not representative for characterizing the charge transporting ability of semiconductors. Instead, an expression for the charge carrier mobility (μ) is required to compare how quickly charge carriers hop between transport sites, taking into account the dependence on energetic difference (Gaussianly distributed) and spatial distance. With Monte Carlo simulations, it has been observed that carriers possessing arbitrary energy within a Gaussian DOS tend to relax to an equilibrium energy level (E_{eq}) under thermal equilibrium, located at an energy $\frac{\sigma^2}{k_B T}$ below the center of the DOS distribution[33]. Considering the transport sites at E_{eq} are limited, carriers require certain energy to undergo thermally activated hopping to other transporting sites, predominantly situated at higher energies, and ultimately contributing to the transport and forming the electronic current. The activation energy for this process is theoretically predicted to be $\frac{4\sigma^2}{9k_B T}$, elucidating the temperature dependence of the mobility of organic semiconductors in the limit of zero electric field[12].

Furthermore, subsequent investigations have demonstrated that the majority of carriers contributing to the transport level primarily originate from the energy level $E_a = \frac{\sigma^2}{2k_B T}$, rather than the equilibrium level. This observation arises from calculations indicating that most carriers at E_{eq} undergo thermal activation and promptly relax back, resulting in a higher probability of unsuccessful processes. The transport level entails a simultaneous consideration of activation energy and available sites, thereby remaining independent of the initial energy of the charge carriers[33,34]. Consequently, the energy level of transport sites is predominantly inferred to situate at $\frac{\sigma^2}{18k_B T}$, close to the center of Gaussian DOS as shown in **Figure 1.5**.

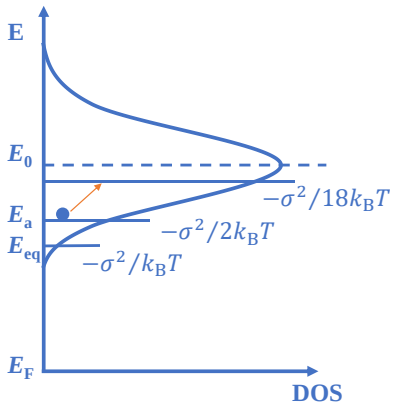

Figure 1.5: Electron hopping in a Gaussian DOS. Gaussian DOS of the material depicted in energy diagram (left), dash line sits at the center of the DOS as baseline of 0 eV, three lines with relevant energy levels correspond to the most transporting sites, source for transporting carriers (E_a) and equilibrium energy level (E_{eq})[12].

From Monte Carlo (MC) simulations, the temperature dependence of mobility is firstly determined with the thermal activation energy. Subsequently, this understanding is extended to encompass the electric field dependence[35]. When an external electric field is applied, the energy gap between the

hopping sites in the field direction gets smaller thus lowering the average energy barrier for upward hopping, while downward hopping remains unchanged. The temperature (T) and electric field (E) dependent mobility can then be summarized from MC simulations as[35]:

$$\mu_{GDM} = \mu_{\infty}\exp\left[-\left(\frac{2\sigma}{3k_{\mathrm{B}}T}\right)^2\right] \times \begin{cases} \exp\left[c\left(\left(\frac{\sigma}{k_{\mathrm{B}}T}\right)^2 - \Sigma^2\right)\sqrt{E}\right], for\ \Sigma \geq 1.5 \\ \exp\left[c\left(\left(\frac{\sigma}{k_{\mathrm{B}}T}\right)^2 - 2.25\right)\sqrt{E}\right], for\ \Sigma < 1.5 \end{cases} \quad (1.3)$$

Where μ_{∞} represents the mobility in the limit of $T\rightarrow\infty$, and the value ranges from 10^{-6} to 10^{-5} m^2/Vs, C is a constant that depends on the site spacing and Σ describes the degree of positional disorder of the hopping sites. This charge transport model is also known as the Gaussian disorder model (GDM). These empirical relations, inherent in the GDM, directly establish a connection between the physically measurable quantity of charge-carrier mobility (μ) and the microscopic disorder parameter (σ), and capture the experimental observations on temperature and electric field dependence of the charge transport in organic semiconductors[35].

1.1.3 Extended gaussian disorder model (EDGM)

To describe the charge carrier mobility in organic semiconductors fully, it is essential to include a third factor: its dependence on charge carrier density (n for electrons, p for holes). This model is termed as extended gaussian disorder model (EGDM)[36]. Upon filling the DOS with charges, the average energy difference between the Fermi level and transport energy decreases, leading to a higher hopping rate and consequentially increased mobility. For instance, the enhanced mobility observed in thin organic diodes (<100 nm) can be elucidated by the increase in average carrier density due to charge diffusion from metal contacts[37]. Another example is the discrepancy in mobility determined from OLEDs and OFETs, attributed to the orders of magnitude difference in charge carrier density[36]. It has been observed in the EGDM that at room temperature and low field, the mobility is strongly determined by the density (n, p) dependence, which becomes more pronounced with increasing disorder in the materials. By contrast, the electrical field (E) dependence of the mobility becomes significant at low temperatures or high fields. The EGDM description[36] of the mobility can be described as:

$$\mu(T,p,E) \approx \mu_p(T,p)\mu_E(T,E) \quad (1.4)$$

Where the density and field dependence are separated into two distinct functions because the two are generally not correlated until extremely high fields or densities exist.

$$\mu_P(T,p) = \mu_0\exp\left(-0.42\left(\frac{\sigma}{k_{\mathrm{B}}T}\right)^2 + \frac{1}{2}\left(\left(\frac{\sigma}{k_{\mathrm{B}}T}\right)^2 - \frac{\sigma}{k_{\mathrm{B}}T}\right)(2pa^3)^{\delta}\right) \quad (1.5)$$

With:

$$\delta = 2\frac{\ln((\sigma k_B T)^2 - \sigma/k_B T) - \ln(\ln(4))}{(\sigma/k_B T)^2} \tag{1.6}$$

$$\mu_E(T,E) = \exp\left(0.44\left(\left(\frac{\sigma}{k_B T}\right)^{3/2} - 2.2\right) \times \sqrt{1 + 0.8\left(\frac{E_{ea}}{\sigma}\right)^2 - 1}\right) \tag{1.7}$$

From EGDM, μ_0(T) can be calculated, which represents the charge carrier mobility in the limit of zero field and zero charge carrier density depending on the temperature. At zero charge carrier density, the mobility scales with $1/T^2$, then at a certain threshold of charge density it modifies to 1/T, reflecting the universal Arrhenius behavior[38], as observed for various organic semiconductors.

In conclusion, three fit parameters are included to describe the mobility in the EGDM. μ_0 with units of [$m^2\ V^{-1}\ s^{-1}$] represents the mobility prefactor, which reflecting the electronic coupling related to the molecular packing and wave function overlap, σ with units of [eV] represents the energetic disorder and mainly influences the *T* dependence of mobility, and a with units of [nm] represents the average hopping distance, affecting the *E* dependence of the mobility.

1.2 Basic processes in OLEDs

Since the discovery of electroluminescence from organic crystals[9], the device concept of two silver electrodes sandwiching the organic material inspired the original design of the OLED structure. In 1987, C.W. Tang et al reported an OLED with a double-layer structure sandwiched between a semitransparent anode indium tin oxide (ITO) and Mg: Ag cathode, demonstrating the feasibility of thin-film OLEDs with the operation voltage under 10 V[10]. Subsequently, researchers devoted decades of effort to optimize OLED performance, employing various fabrication techniques such as thermal evaporation and spin coating for film deposition. Nevertheless, the fundamental operational principles underlying OLEDs remained consistent.

Primarily, OLEDs comprise an emissive layer sandwiched between two electrodes. Under electrical bias, the cathode injects electrons into the LUMO, while the anode extracts electrons, a process known as hole-injection. Electron flow is predominantly unidirectional due to a significant energetic barrier against reverse flow. To facilitate electron injection, cathodes commonly utilize low-work function materials such as Al, Ba, Ca, Cs, CsF, ZnO, and Cs_2O_3. To enable light output from the planar device, at least one electrode must be transparent. Given the limited transmittance of the common cathodes, the anode material is typically selected for both high work function and high transparency. Transparent substrates (typically glass or plastic) with an ITO layer are commonly employed as the anode in OLEDs. ITO exhibits an extraordinary balance of optical transparency and conductivity, moreover, it can be pre-patterned through lithography or shadow mask. Generally, a layer of PEDOT: PSS is spin-coated on top of the ITO to serve as a highly conductive buffer layer, smoothing the rough ITO surface and facilitating hole-injection. A typical OLED with double layer structure is showed in **Figure 1.6**.

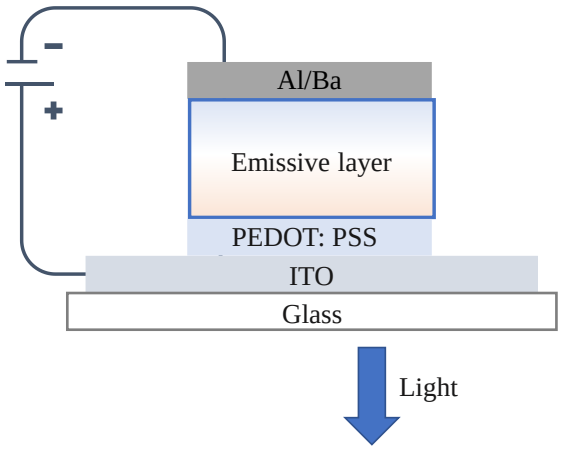

Figure 1.6: Typical OLED device configuration.

1.2.1 OLED current voltage characteristics

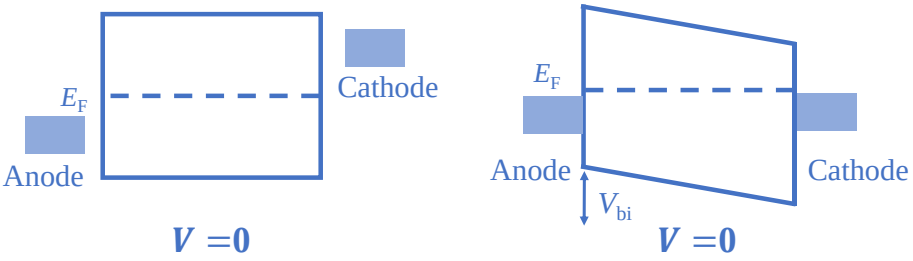

Figure 1.7: Band diagram when putting two electrodes in contact with semiconductor.

OLEDs consist of two metal electrodes with different work functions. When two metals are brought into contact with a semiconductor, especially with different Fermi energy levels (E_F), electrons will flow from via the external circuit from the metal with the low work function to the metal with the high work function, establishing an equilibrium condition known as Fermi level alignment, as shown in **Figure 1.7**. This alignment implies that the E_F for electrons from both sides are equal at the contact. Introducing an organic emissive layer between these two electrodes thus induces the alignment of chemical potentials throughout the device, resulting in the existence of a built-in voltage (V_{bi}). When the applied voltage is increased, there are three situations to consider with respect to the value of V_{bi}.[12]

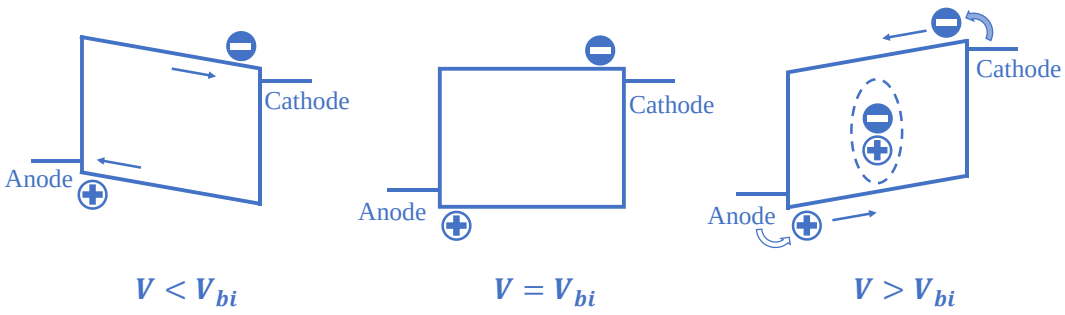

Figure 1.8: Energy band diagram of OLED at different biased voltage with respect to built-in voltage (V_{bi}).[39]

As shown in **Figure 1.8**, when a voltage is initially applied, the electric field points in the opposite direction of the current flow, indicating that the current is diffusion-dominated when $V < V_{bi}$. Upon increasing the applied voltage to V_{bi} (flat band condition), the applied electrical field neutralizes the internal field completely, representing the minimum bias required for charge injection. Beyond this point, the electric field aligns with the direction of the current flow, signifying effective charge injection, resulting in a drift-dominated current.

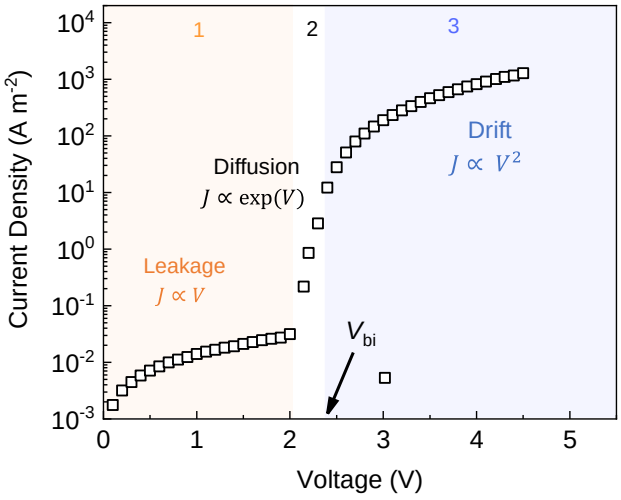

Figure 1.9: Typical Current density-voltage (*J-V*) characteristic of trap-free OLED.[12]

The current density-voltage (*J-V*) characteristic of an OLED is often discussed in three regimes depending on the applied voltage. In **Figure 1.9**, a depiction is provided to elucidate the case of an ideal trap-free OLED scenario. Regime 1 represents leakage current arises from localized shorts of the films, and the magnitude of the leakage current surpasses that of the diffusion current at early stage[38]. Therefore, the current-voltage relationship typically follows Ohm's law, displaying linearity, and exhibits temperature independence.

$$J = \sigma \frac{V}{L} \tag{1.8}$$

Where σ represents the metallic conductivity of the local short-circuit. For comprehensive device analysis aimed at discerning the diffusion current more distinctly, it is preferable to minimize the leakage current. For regime 2, an exponential dependence of current-on voltage occurs, indicating the dominance of a diffusion-driven current, where the exponential dependence on voltage can be represented with the classical Shockley diode equation[40].

$$J = J_0 \left[\exp\left(\frac{qV}{\eta k_B T} \right) - 1 \right] \tag{1.9}$$

Where η is the ideality factor[41] that typically ranges in between 1 to 2, J_0 is the saturation current density, determined by extrapolating the *J-V* curve to zero applied voltage, T is temperature and k_B is Boltzmann constant. When $V > V_{bi}$, the transition marks the onset of regime 3 which is the drift-dominated regime. In this case, the current-voltage relationship is described by a space-charge-limited current (SCLC),

provided that the injecting contact is ohmic. For a trap-free semiconductor, neglecting diffusion, the SCLC can be described by the Mott-Gurney equation[42].

$$J = \frac{9}{8}\varepsilon\mu\frac{(V - V_{\mathrm{bi}})^2}{L^3} \tag{1.10}$$

Where ε is the dielectric constant, and L is the sample thickness.

It is noteworthy that the charge carrier density of OLEDs often exceeds that of single-carrier diodes. This is attributed to the compensatory electrostatic interaction between holes and electrons in a double-carrier device, enhancing the buildup of space charge.

1.2.2 Charge injection

When discussing the charge injection from individual electrodes in OLEDs, it is important to recognize that this concept applies to all organic semiconductor devices, not just OLEDs. Organic semiconductors typically have a low concentration of intrinsic charge carriers due to their notable energy bandgap, rendering high resistivity (~10^{15} Ω cm) for device operation[43]. In the absence of impurities or chemical doping, there is no net charge in organic semiconductors. Even with existing impurities, the number of intrinsic charge carriers (n_i) typically range from 10^5 to 10^{10} cm^{-3}, which is close to the intrinsic carrier concentration of silicon[44]. Therefore, injection from both anodic and cathodic contacts supplies extrinsic charge carriers, enabling a high current density of 1 A/cm^2 for practical operation in most organic semiconductor devices[44].

It is well known that when injected charges flow from metal to metal an ohmic (low resistance) contact is formed in between these metal layers due to the existence of large amount of free electrons. However, when putting metal into contact with an organic semiconductor for charge injection purpose, a potential barrier occurs due to the energetic difference between the E_F of the metal and the HOMO/LUMO (for hole/electron injection) of the semiconductor[45–48]. The potential is termed the contact potential, which also known as the original charge injection barrier Φ_b, inducing the conduction band tilting when an electrical field is applied[49].

Simultaneously, an equal positive charge, referred to as the image charge, is induced when an electron is injected from the metal to the organic layer[50]. The image potential is given by $\Phi_i = -\mathrm{q}/(16\pi\varepsilon\mathrm{x})$ representing an electron with charge q at a distance -x from the metal surface. The injection barrier Φ_b at the interface is then lowered by $\Delta\Phi = \sqrt{(qF)/(4\pi\varepsilon)}$ under an applied electrical field of F, resulting in the effective injection barrier $\Phi_{\mathrm{eff}} = \Phi_b - \Delta\Phi$, known as Image-Force barrier lowering[51]. For inorganic semiconductors the charge injection occurs via thermionic emission, thus the injection current follows the Richardson-Schottky equation. For low mobility materials as most organic semiconductors also diffusion effects need to be included in the injection current[52]. When the temperature is too low to overcome the injection barrier, charge injection can also occur through Fowler-Nordheim tunneling if the applied electric field is very high (thin-layer of organic semiconductor)[53], depicted by a triangle barrier as show in **Figure 1.10**.

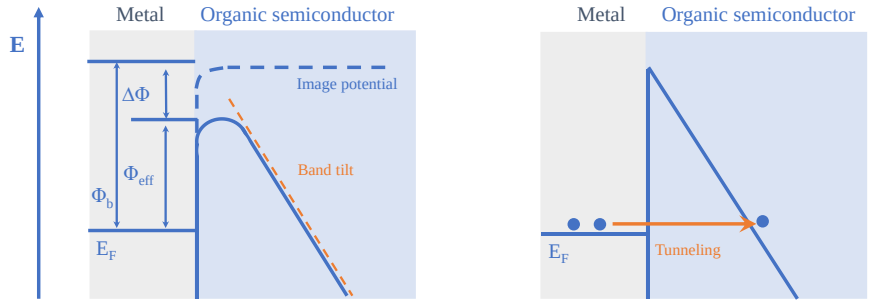

Figure 1.10: Energy band diagram at the metal/organic semiconductor interface. At low electric field (right), the band tilts when applied electrical field (orange dashed line), with the existence of image potential (blue dashed line), the injection barrier is lowered from Φ_b to the Φ_{eff} at the interface. At high electrical field, charge injection via tunneling with a triangle barrier to the right[53,54].

Since an injection barrier is generally not preferable for charge injection into organic semiconductors, an ohmic contact is widely desired for eliminating it[55,56]. In this scenario, the contact serves as a reservoir of carriers, injecting a quantity of carriers that overwhelms the thermally generated intrinsic ones inside the semiconductor. As a result, the electric conduction of the semiconductor becomes extrinsic and space-charge limited in nature[57]. A successful strategy developed in our group involves inserting an interlayer of approximately 4 nm thick at the metal/organic interface, which effectively dismisses the injection barrier through electrostatic decoupling[55]. The key point in constructing the electron ohmic contact is carefully selecting the interlayer material with a lower electron affinity (electrons) or higher ionization potential (holes) than the organic layer.

1.2.3 Single carrier devices

To comprehensively investigate the electrical performance of OLEDs, it is necessary to first distinguish the individual contribution of hole and electron transport separately. For an OLED as a double carrier device, this poses an inherent challenge due to the simultaneous injection of both holes and electrons. Therefore, single carrier devices are designed to study the charge injection and charge transport characteristics of electrons and holes separately, avoiding the complexity introduced by double-carrier recombination processes[58].

The working principle of a single carrier device is to ensure the presence of only one type of charge carrier, i.e. an electrode for charge injection and a counter electrode to prevent charge injection of the opposite sign. Therefore, the electrode materials must be carefully selected with their WF aligning the HOMO/LUMO energy level of organic materials. For example, in a hole-only device (HOD), efficient hole injection and extraction can be achieved by introducing electrodes with a WF equal to or higher than the HOMO of the semiconductor on both sides, such that electron injection cannot occur due to the large injection barrier to the LUMO. The determination of the injection and extraction sides depends on the applied electric field direction. In addition, a single carrier device with both electrodes forming an ohmic contact is considered a symmetric device, while with only one ohmic contact it is an asymmetric device with an extraction barrier. Due to the presence of only one type of carrier parameters related to charge transport, such as mobility and trap densities, can be linked to the current density-voltage (*J-V*) characteristic of the device, and further quantified for organic semiconductors.

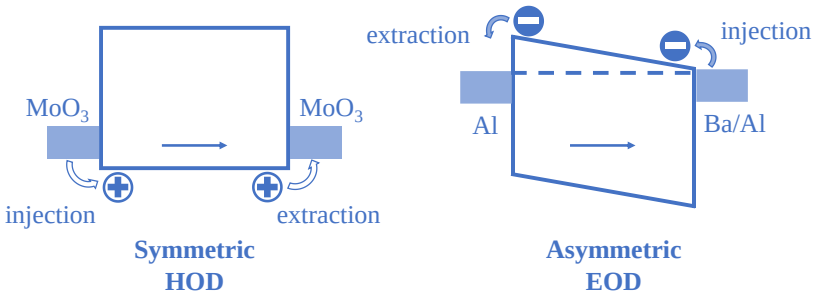

Figure 1.11: Single carrier devices architecture. The band diagrams of symmetric HOD (left) and asymmetric EOD (right) after reaching thermal equilibrium, with arrow inside suggesting the electric field direction.

The hole-only device (HOD) or electron-only device (EOD), wherein an organic layer is sandwiched between two electrodes with specific work functions, are depicted in **Figure 1.11**. In the symmetric HOD, both electrodes exhibit high work functions to establish ohmic hole injection, indicating that hole injection is the same in both electric field directions. In the asymmetric EOD, the Ba/Al side has a low work function for ohmic electron injection, leading to a device current reaching the space charge limit, whereby in the absence of trapping, the mobility can be determined by the Mott-Gurney equation.

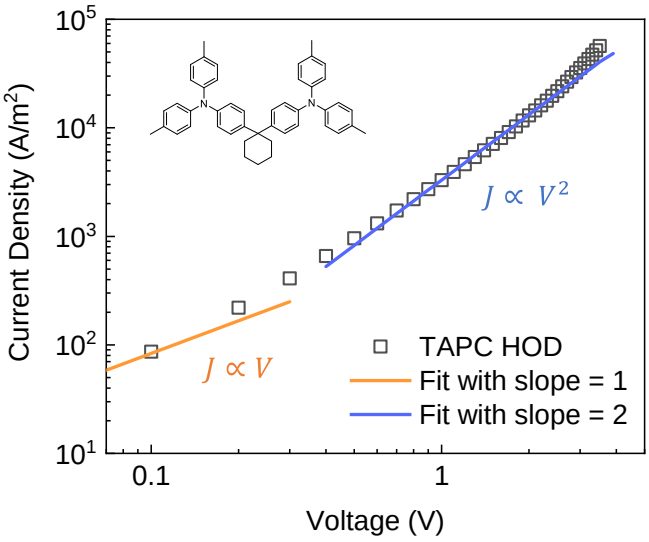

Figure 1.12: Current density-Voltage characteristic of TAPC hole only device.

Here, a simple example is illustrated in **Figure 1.12**, depicting a typical *J-V* curve for a HOD with symmetric device structure[59]. The absence of V_{bi} implies that at zero bias already holes diffuse into the organic semiconductor for Fermi-level alignment. This background hole density then upon applying a voltage[37], leads to a linear dependence at the initial part of the *J-V* curve, which can be described by Ohm's Law (equation 1.8).

In the higher voltage regime, the injected carriers overwhelm the background density and their net charge creates a gradient in potential that prevents additional injection of charge carriers, which leads to the buildup of space charge. When the build-up of space charge saturates throughout the device, indicating that SCLC is reached, the *J-V* curve exhibits a typical quadratic dependence, following the

Mott-Gurney relation (equation 1.2) as mentioned before[42]. SCLC represents the maximum current that a HOD or EOD can sustain.

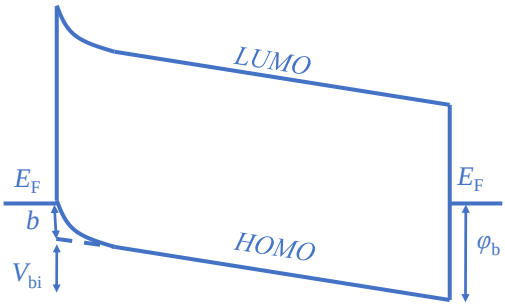

Figure 1.13: Energy diagram of an organic hole-only device, with HOMO and LUMO. b denotes the band bending parameter.

As mentioned above, a V_{bi} exists in an asymmetric diode when devices contain electrodes with two different WFs, which is typically subtracted from the applied voltage to correct the *J-V* analysis. However, as mentioned above for ohmic contacts on non-doped semiconductor, charge carriers diffuse from the electrode into the organic layer, forming an accumulation region close to the injection contact, which causes band bending and a reduction of V_{bi}. This phenomenon is known as the band bending effect as shown in **Figure 1.13**, the reported value for this effect is described as b which typically amounts to 0.2~0.3 eV. The actual built-in voltage should be expressed as $V_{bi} = \Phi_b - b$, where Φ_b represents the injection barrier on the extracting electrode and the value equals to WF difference in an ohmic contacts scenario.

$$b = \frac{k_B T}{q}\left[\ln\left(\frac{q^2 N_C L^2}{2k_B T\varepsilon}\right) - 2\right] \qquad (1.11)$$

Where N_C represents the total number of conducting states, q is the elementary charge and L for thickness.

1.2.4 Trap-limited electron transport

The EGDM model for mobility mentioned in section 1.2.3 can describe the charge transport in organic semiconductors. To simulate the *J-V* characteristics, the EGDM mobility function is incorporated in 1D drift-diffusion model. However, most organic semiconductors typically show a more pronounced voltage dependence than as expected for a trap-free scenario[60] (equation 1.2), indicative of trapping behavior of either holes or electrons. This behavior arises from the presence of energy states in the bandgap (traps) that charge carriers preferentially occupy over transport sites.

Organic semiconductors generally have a transport site density of around 10^{26} m^{-3}, while the trap densities are much lower (10^{22}-10^{23} m^{-3}), however with significant impact on the charge transport characteristics[12]. Due to the lower trap density, trapped charge carriers do not participate to the transport due to the energy barrier to transport states and the large distance to other trapping sites, resulting in a reduced contribution to the device current. Thus, the drift current remains lower than the trap-free case until all traps are filled, leading to trap-limited transport with stronger voltage dependence. The current regime before all traps are filled is termed trap-limited current (TLC) in **Figure 1.14**.

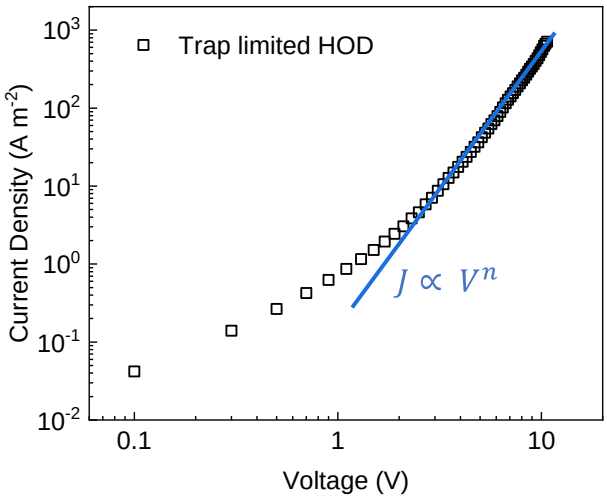

Figure 1.14: Current density-voltage characteristic for trap-limited HOD.

An early description was proposed by Mark and Helfrich[42] for trap limited currents, where trapping sites were assumed to be exponentially distributed in energy, particularly below the conduction band for electron trapping.

$$N_{\mathrm{t}}(E) = \left(\frac{N_{\mathrm{t}}}{k_{\mathrm{B}}T_{\mathrm{t}}}\right) exp\left[\frac{E - E_{\mathrm{c}}}{k_{\mathrm{B}}T_{\mathrm{t}}}\right] \tag{1.12}$$

$N_{\mathrm{t}}(\mathrm{E})$ is the trap density at certain energy E, E_{c} denotes the conduction band energy, N_{t} stands for the total number of traps, and $\mathrm{T_t}$ is the temperature of traps defining the characteristic energy of trap distribution. The expression for the trap-limited current-voltage characteristics is given by:

$$J_{TLC} = N_C e\mu \left(\frac{\varepsilon}{eN_t}\right)^r \left[\left(\frac{2r+1}{r+1}\right)^{r+1} \left(\frac{r}{(r+1)}\right)^r\right] \frac{V^{r+1}}{L^{2r+1}}, \quad \mathrm{r} = T_t/T \tag{1.13}$$

Where N_{c} is the total density of states in the conduction band (around 10^{26} m^{-3} as mentioned above), $\varepsilon = \varepsilon_0\varepsilon_r$ is the dielectric constant and e is the elementary charge, μ is the charge carrier mobility and L is organic layer thickness. r is a constant that is determined from the *J-V* curve, plotted on a log-log scale, and thickness dependence of the trap limited currents according to $J \propto V^{r+1}/L^{2r+1}$. The value of r depends on the trap distribution. For the case of $r = 1$, $J \propto V^2$ indicates a slope of 2, as the fingerprint of SCLC (according to Mott-Gurney law) suggesting trap free transport. For the case of $r > 1$, $J \propto V^m$ and $m > 2$ indicates a slope higher than 2, suggesting trap limited transport.

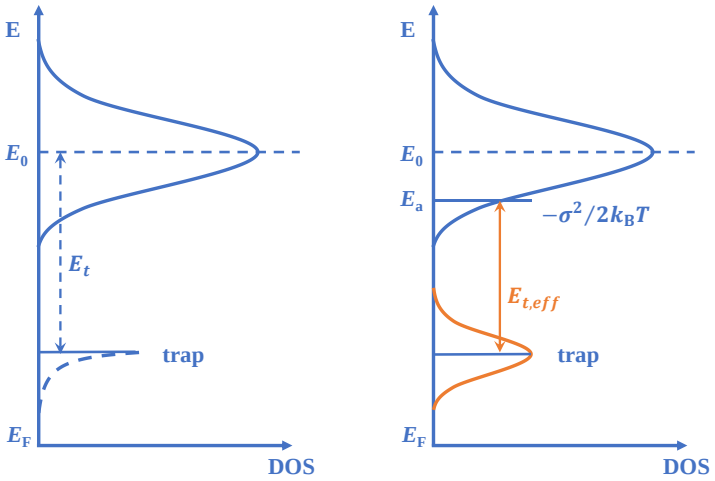

Figure 1.15: Electron trap DOS below the material DOS (LUMO) with exponential distribution (left) in Mark and Helfrich's description, and Gaussian distribution to the right. Two modifications were marked in orange.

Two modifications were later included in this description when applied to organic semiconductors as shown in **Figure 1.15**. The first modification accounts for the fact that organic semiconductors generally exhibit a DOS following a Gaussian distribution[61,62]. Carriers occupying the energy level $E_a = \sigma^2/2k_BT$ below the middle of the DOS (E_0) contribute significantly to the transport, as mentioned previously. In contrast, the original expression by Mark and Helfrich considered only a single conduction band edge. Therefore, for organic semiconductors with a Gaussian DOS the effective trap depth is no longer $E - E_c$ but

$$E_{t,eff} = E - E_a \tag{1.14}$$

Where E represents the original trap depth. Considering the disorder and temperature dependence of E_a, the effective trap depth will now exhibit a temperature dependence effect, which has been experimentally proven to result in a smaller effective trap depth with decreasing temperature[63].

Secondly, Mark and Helfrich's expression assumed that the traps are exponentially distributed in energy, whereas for organic semiconductors, a Gaussian distribution is more suitable[62], similar to the HOMO/LUMO DOS. Although there is no big difference for the analytical solutions when comparing these two profiles, the description of effective trapping sites is modified as

$$N'_{t(eff)} = \frac{N_t}{2}\exp\left[\frac{E_t}{r' k_B T}\right], \qquad r' = \sqrt{1 + 2\pi\left(\frac{\sigma_T}{4k_BT}\right)^2} \tag{1.15}$$

Traps for organic semiconductors exhibits a strong correlation with energy levels among all different kind of materials. Generally, it is observed that hole transport becomes trap-limited when the organic compound has an ionization energy (IE or HOMO) larger than 6.0 eV, while electron transport becomes trap-limited when the electron affinity (EA or LUMO) is smaller than 3.6 eV as shown in **Figure 1.16**. This universal definition of a trap-free energy window[64] suggests that organic semiconductors with bandgap inside this window are less susceptible to charge trapping. Additionally, the trap-free energy window indicates a common extrinsic source for traps. Oxygen-related impurities are proposed as sources for electron traps while water clusters are proposed as hole traps. Other proposed

origins of charge trapping include kinks and defects in polymer chains, or chemical residues from synthesis, among others.

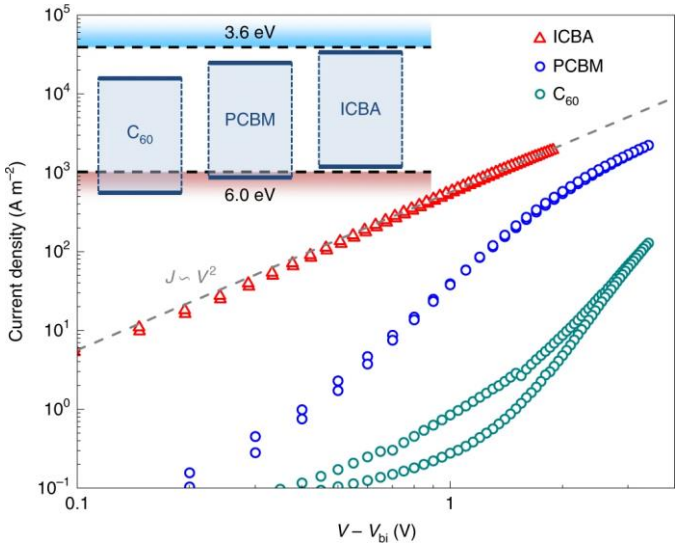

Figure 1.16: Current density-voltage characteristics of ICBA, PCBM and C_{60} hole-only devices, with the voltage corrected for V_{bi}. The grey dashed line suggests a quadratic voltage dependence ($m = 2$). The inset of the plot shows a schematic energy diagram indicating the IE and EA of the organic semiconductors with respect to the trap-free window (horizontal dashed lines)[64]. Reproduced from reference [64].

1.2.5 Charge recombination

Following an in-depth study of charge transport, another crucial process in a double-carrier device (OLED) is charge recombination. In general, organic semiconductors have a low dielectric constant, which means that free electrons and holes tend to form a bound state known as an exciton when they are in close proximity. This process is termed charge recombination (depicted in **Figure 1.17**). Subsequently, the exciton can decay radiatively or non-radiatively. The non-radiative decay of excitons is undesirable in an OLED as it does not contribute to the photon emission but instead wastes excitons, thereby decreasing the internal quantum efficiency (IQE).

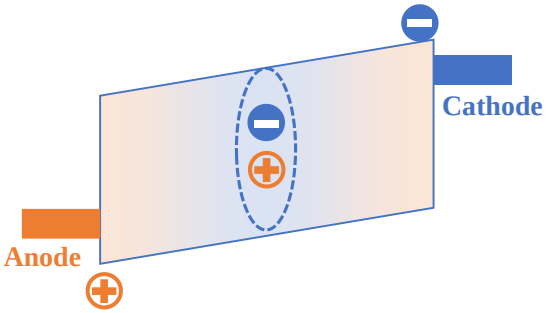

Figure 1.17: Illustration of charge recombination process in an OLED. Electrons (holes) are injected from cathode (anode) and transport via the functional layers to recombine within the emissive layer, forming an exciton.

The bimolecular recombination process in OLEDs is referred to as Langevin recombination[65–67]. The recombination rate (R_L) is determined by the mobility and density of charge carriers, and is expressed as follows:

$$R_L = \frac{q}{\varepsilon_0 \varepsilon_R}(\mu_n + \mu_p)(np - {n_i}^2) \tag{1.16}$$

The intrinsic carrier concentration n_i is given by ${n_i}^2 = N_{CV}\exp(-E_{gap}/k_BT)$, where N_{CV} represents the DOS in the valence band and conduction band. R_L depends on the joint mobility of both charge carriers. Two prerequisites are listed when applying the Langevin equation: 1) the recombination is diffusion-limited, and 2) material should be homogeneous. It is important to note that, charge carriers can be impeded between organic-organic interfaces, thus impacts on the uniform distribution of charge carriers.

Competing with bimolecular recombination, another significant process in OLEDs is trap-assisted recombination, also known as Shockley-Read-Hall (SRH) recombination[68,69]. In the presence of trap states, a carrier becomes immobile upon falling into the trap states and subsequently recombines with a free carrier of the opposite species. Generally, SRH recombination is considered non-radiative, which is unfavorable in devices. For a current density-voltage (*J-V*) measurement, an equilibrium between trapping, de-trapping, and trap-assisted recombination is assumed. The SRH recombination rate (R_{SRH}) is then described as follows:

$$R_{SRH} = \frac{C_p C_n N_t}{C_n(n + n_1) + C_p(p + p_1)}(np - {n_i}^2) \tag{1.17}$$

$$C_{n/p} = \frac{q}{\varepsilon_0 \varepsilon_R}\mu_{n/p} \tag{1.18}$$

Where $C_{n/p}$ represents the capture coefficient, n_1 (p_1) is the concentration of trapped electrons (holes), and ${n_i}^2 = n_1 p_1$. Additionally, when discussing hole traps, N_t should be replaced by P_t. For an organic semiconductor with low mobility specifically, where recombination is diffusion limited, the $C_{n/p}$ can be determined as equation 1.18. To distinguish between these two recombination mechanisms, one can extract the ideality factor from the diffusion-limited regime of the current in a *J-V* plot or the light in an *L-V* (luminance-voltage) plot:

$$\eta = \left(\frac{k_B T}{q}\frac{\partial \ln J}{\partial V}\right)^{-1} \tag{1.19}$$

The value of η amounts to 1 for Langevin recombination and 2 for SRH recombination[39].

As mentioned earlier, recombination in OLEDs primarily occurs due to the low dielectric constant, causing electrons and holes to recombine predominantly within a strong Coulomb attraction rather than passing each other. Moreover, recombination typically occurs across a distributed area, not confined to a single plane[70]. In a typical OLED, blocking layers are often incorporated to confine the recombination zone within the emissive layer, thereby maximizing exciton utilization. In the case of single-layer OLEDs, where recombination is more sensitive to the transport properties of the emitter, ideally balanced transport results in electrons and holes meeting in the middle of the device, where recombination occurs. However, imbalanced transport, where one carrier type dominates (e.g., due to differences in electron and hole mobility, with $\mu_n < \mu_p$ or $\mu_n > \mu_p$), can shift the location of Langevin

recombination towards either the cathode or anode side, as shown in **Figure 1.18**. More details on this will be discussed later in chapter 3 when comparing the multilayer OLEDs with single-layer OLEDs.

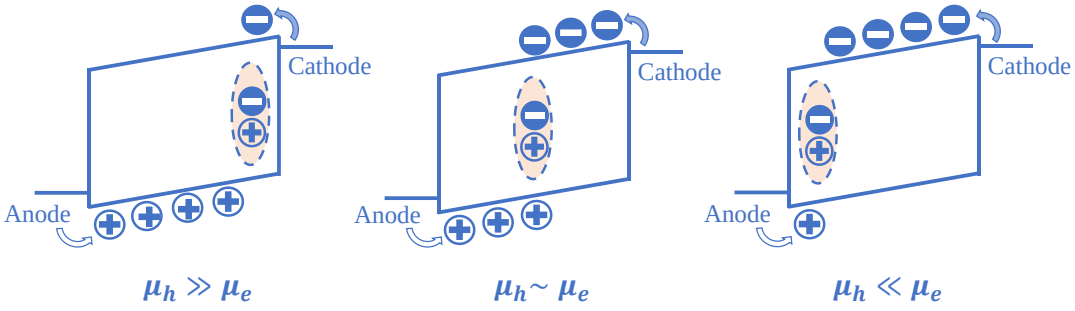

Figure 1.18: Exciton recombination at different locations within the device depending on different transport characteristics of electrons and holes of the emitter.

1.2.6 Excitons

In organic semiconductors, when an electron in the HOMO gets excited to the LUMO, leaving a positive charge behind (called a hole), the low dielectric constant allows the electron and hole to effectively form a bound pair due to the presence of the coulomb force. This bound electron-hole pair is referred to as an exciton[71]. Excitons can be generated either optically or electrically, causing a different distribution among singlet and triplet states. Optical excitation means when organic materials absorb a photon from the surroundings (laser or lamp), Frenkel excitons (only singlets) are formed, typically exhibiting a binding energy of around 0.4 to 1 eV and are localized within a small spatial region with a radius ~ 1 nm[72–74]. During optical excitation, only the transitions within the same spin manifold are allowed. Therefore, transitions from the ground state (singlet) can only result in a singlet excited state (S = 0). However, during electrical excitation, triplet excitons (S = 1) can also form as shown in **Figure 1.19**. While singlet excitons can only exist in one spin state (m_s = 0), triplet excitons can exist in three spin states (m_s = -1, 0, 1). Therefore, under electrical excitation, the statistical probability for forming excitons is 25% for singlets and 75% for triplets. [75]

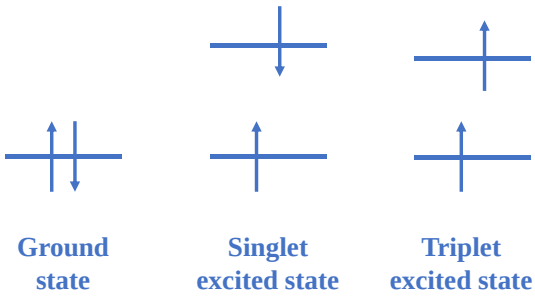

Figure 1.19: Spin configuration of electrons in the ground as well as excited singlet and triplet state.

Once excitons are generated, several transitions may occur, which are well depicted in the Jablonski diagram (**Figure 1.20**). Singlet excitons, with lifetimes in the nanoseconds range, can undergo radiative decay to the ground state, emitting a photon in a process known as fluorescence with a nanosecond (ns) scale lifetime. This decay is allowed according to Fermi's golden rule, as the ground state exhibits a singlet character. Direct radiative decay of triplet excitons to the ground state is forbidden due to the

Pauli exclusion principle, for this process a spin flip would be required that in organic semiconductors has a very low probability. Therefore, this transition typically leads to non-radiative decay. However, the spin-flip becomes possible with strong spin-orbit coupling, achieved by incorporating heavy metal atoms into the chemical structure of emitters. This allows triplet excitons to undergo radiative decay, emitting photons in a process known as phosphorescence with a microsecond (μs) scale lifetime.

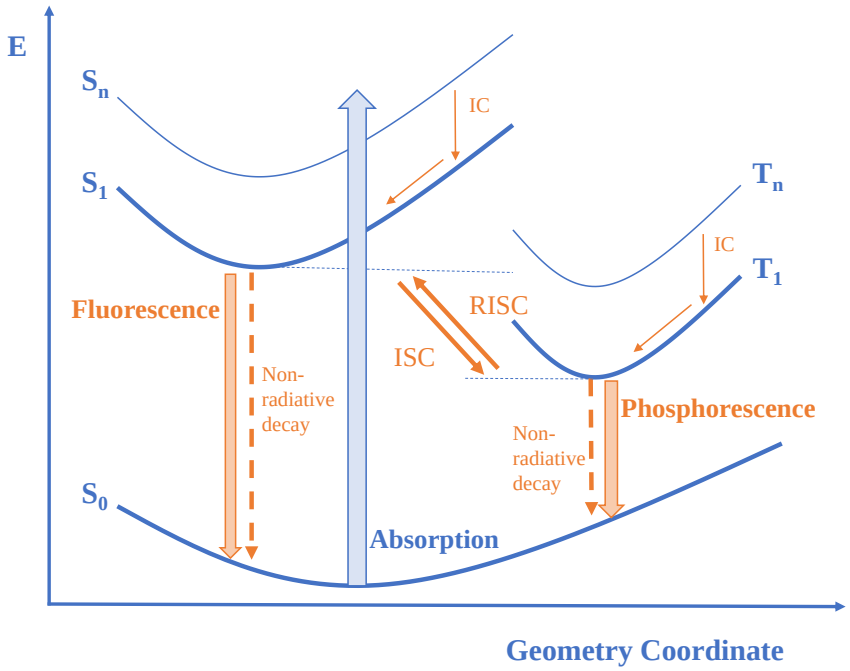

Figure 1.20: Jablonski diagram for organic molecules, illustrating energy transitions like absorption, internal conversion (IC), intersystem crossing (ISC), reverse intersystem conversion (RISC), fluorescence, phosphorescence, and non-radiative relaxations. The geometry coordinate indicates the configuration change of the molecule. [76]

Photoluminescence quantum yield (PLQY) is defined as the ratio of radiative decay rate (k_r^*) to the sum of radiative and non-radiative decay rate (k_{nr}) under photo excitation[77]. The non-radiative decay

$$PLQY = \eta_{rad}^* = \frac{k_r^*}{k_r^* + k_{nr}} \qquad (1.20)$$

often results from processes like vibrational relaxation[78,79].

Photophysical transitions between singlet and triplet states occur when a spin flip is permitted, facilitated by spin-orbit coupling. This process is more favorable when there is overlap between the vibrational levels. The transition from a higher energy excited state to a lower one with different spin multiplicity is termed intersystem crossing (ISC), while the reversed transition is known as reverse intersystem crossing (RISC). Excitons move via diffusion as charge-neutral species, and their motion can be elucidated by using either Förster or Dexter energy transfer models[80].

1.3 Development of OLED emitters

Carbon-based conjugated polymers with light-emitting properties have been extensively studied. The first polymer LED used poly-phenylene vinylene (PPV)[11], primarily composed of benzene rings and hydrocarbon chains. By integrating various side chains, the emission color of PPV derivatives can be tailored, leading to corresponding adjustments in optoelectronic characteristics and solubility.[81,82] Additionally, polymers such as polyfluorene (PFO)[83] have gained significant attention for their remarkable blue emission. PPV-class polymers and polyfluorenes are regarded as the typical representatives of the first generation of PLEDs. The versatility afforded by chemical modifications renders PLEDs promising candidates for flexible applications, particularly in terms of low-cost and large-area fabrication via techniques such as bar or spin-coating.[2]

Small molecules possessing conjugated systems have been a focal research point in recent years, owing to their exceptional semiconducting properties.[10] When subjected to thermal evaporation, these molecules tend to exhibit higher purity, resulting in enhanced charge transport and device performance compared to PLEDs. In 1987, the first evaporated OLED was developed,[10] featuring two layers of small molecules. An emissive layer composed of Alq_3 was utilized, with a diamine-based layer serving to block electrons injected from the cathode. Subsequent advancements in designing small molecule emitters enabled the creation of a full visible color range and achieved 100% IQE by harvesting triplets. However, addressing the short operational lifetime has been a crucial challenge for the sustainable growth of OLEDs. Notably, significant progress has been made in this regard, particularly for green and red emitters. However, the widespread utilization of OLEDs is currently limited by the stability of blue pixels, whether used for illumination or display purposes. The formidable challenge arises from the high photon energy required for blue emission, which can lead to photochemical instability.

Overall, maximizing photon harvest remains a significant objective, as it contributes significantly to device performance by mitigating rapid degradation. The ultimate performance of OLEDs depends on the emitter's exciton utilization efficiency. As material and device development are mutually reinforcing, the following section provides a brief overview of OLED emitters with different emission mechanisms (**Figure 1.21**)[13].

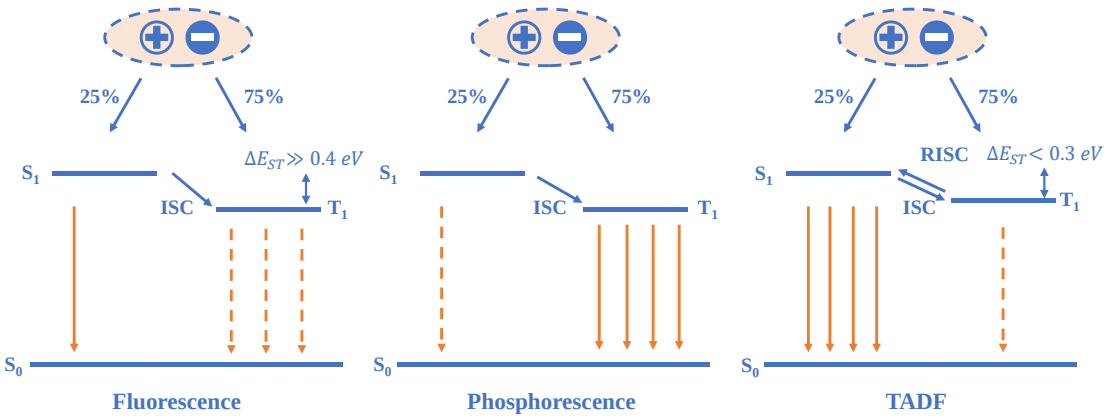

Figure 1.21: Schematic diagrams of singlet and triplet emission mechanisms for fluorescence, phosphorescence and thermally activated delayed fluorescence (TADF).

1.3.1 Fluorescence

The first generation of emitters comprise of fluorescence materials, meaning that only singlet excitons undergo radiative decay to the singlet ground state ($S_1 \rightarrow S_0$), while other transitions related to triplet excitons are all non-radiative. Consequently, the maximum internal quantum efficiency (IQE) of a traditional fluorescent emitter is only 25% for electroluminescence. This implies that the upper limit of external quantum efficiency (EQE) of OLEDs with fluorescent emitters is approximately 5% without additional optical engineering techniques.

The most well-known fluorescent emitter, 8-hydroxyquinoline aluminum (Alq_3), was first reported in 1987[10]. It was employed in vacuum-deposited OLEDs with an external quantum efficiency (EQE) of approximately 1% and a green emission wavelength of 550 nm. The brightness of the device exceeded 1000 cd/m^2 with an operating voltage of less than 10 V, which represented a significant achievement in the field of OLEDs. Subsequent reports have documented comparable achievements in the field of red emitters. For instance, 4-(dicyanomethylene)-2-methyl-6-[4(dimethylaminostyryl)-4H-pyran] (DCM) and its derivatives have been employed in doping OLEDs, with an EQE of approximately 2% and an emission wavelength of 610-650 nm[84]. However, the device performance for such red emitters was found to be highly dependent on the doping concentration. This is because the majority of red emitters exhibit a severe quenching effect from molecular aggregation in the film, which is attributed to the structure polarity or π-conjugated molecular design[85]. One notable exception is a non-doped red OLED with a fluorescent emitter reported in 2000[86].

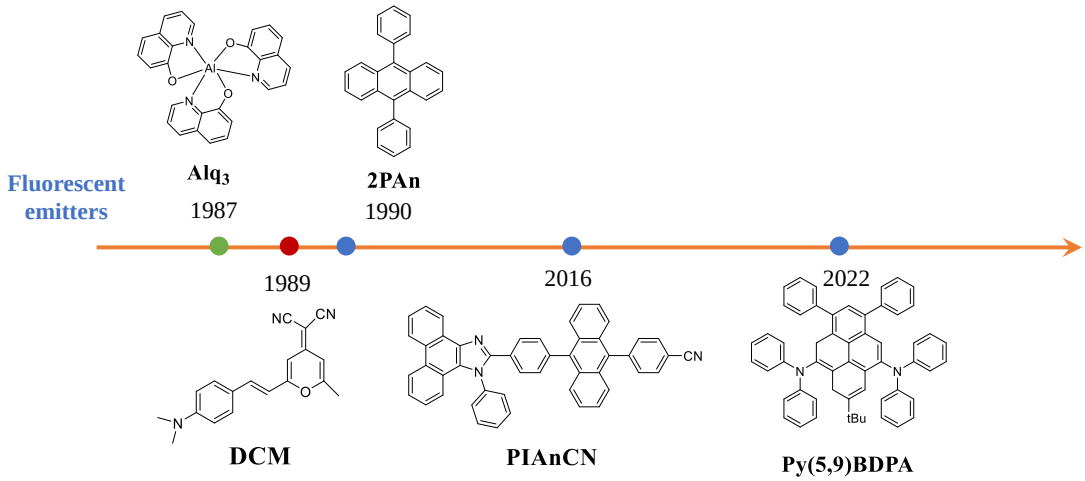

Figure 1.22: A selection of OLED emitters based on fluorescent molecules.

Anthracene derivatives stand out as noteworthy blue fluorescent emitters due to their wide bandgap and commendable thermal stability arising from their rigid chemical structure[87]. The compound 2PAn in **Figure 1.22**, for instance, demonstrated a blue emission peak at 452 nm with an EQE of 2.82% in a non-doped multilayer OLED[88]. Subsequent modifications involved the introduction of bulky substituents at the 9- or 10-position to fine-tune the emission towards the deep blue spectrum (444 nm). This adjustment not only shifted the emission wavelength but also contributed to an improved EQE of 5.17%, attributed to mitigated self-aggregation effects[89]. Irrespective of the limitations in efficiency, fluorescent materials capitalize on extended lifetimes, particularly noteworthy for stable blue emitters[90].

Another category characterized by singlet emission is known as delayed fluorescence. This process involves the merging of two triplets into a singlet through a process known as triplet-triplet annihilation (TTA), resulting in an increased theoretical maximum IQE of 62.5%[91]. In the TTA process, two triplet excitons combine to generate a higher energy triplet exciton and a ground state. This high-energy triplet exciton undergoes intersystem crossing (ISC) to reach a singlet-excited state, producing fluorescence with an extended lifetime. Consequently, TTA emitters exhibit both prompt (ns) and delayed (μs) components in exciton lifetime, contributing to nearly tripled singlet emission. Given that the accumulation of triplets is essential for efficient TTA-OLED, it could also induce serious roll-off in device efficiency[92]. An early strategy to address this issue involves introducing a host matrix. In 2016, Hsin et al. reported a blue delayed fluorescence (TTA-OLED) with an extended operation time (LT_{95} @ 2000 cd/m²) reaching up to 53 hours[93]. A 10% assistant host was doped into the emissive layer (EML), effectively reducing triplet quenching under highly accumulated conditions and blocking triplet diffusion. In 2017[94], a commercial blue TTA-OLED was developed by the same group for mass production, which shows LT_{90} of 550 hours at 2000 cd/m². In 2018, the compound PIAnCN was reported without the assistance of host materials, and the non-doped blue OLED exhibited an impressive EQE of 9.4% at 1000 cd/m², demonstrating suppressed efficiency roll-off in rigid planar pi-conjugated phenanthroimidazole anthracene structure[92].

Meanwhile, pyrene derivatives featuring a classic donor-acceptor structure were reported with comparable device performance in TTA-OLEDs. In 2022, Py(5,9)BDPA was reported in a multilayer OLED with an ADN host, showing a remarkable operational lifetime (LT_{95} @ 1000 cd/m²) of 534 hours with blue emission characterized by Commission Internationale de l'éclairage (CIE) coordinates (0.13, 0.27), but a relatively low EQE of 4.3% [95]. In summary, TTA-OLEDs present a notable enhancement in device efficiency for fluorescent emitters, although the theoretical upper limit efficiency is only 62.5%. Despite decent device stability, the device efficiency of TTA-OLEDs is generally lower compared to that of phosphorescent or TADF OLEDs[96].

1.3.2 Phosphorescence

One significant disadvantage of fluorescent emitters is that the remaining triplet excitons do not participate in the photon generation process. In order to maximize the utilization of all excitons, phosphorescent heavy-metal complexes have been developed as the second generation of emitters[97]. The incorporation of heavy atoms into the organic skeletons played a crucial role: firstly, ensuring the radiative transition from the first excited triplet state (T_1) to the ground singlet state (S_0), and secondly, promoting the intersystem crossing (ISC) process, both facilitated by the strong spin-orbit coupling effect[98]. Consequently, phosphorescent emitters often achieve 100% IQE, indicating the complete utilization of excitons.

In 1998, the first PhOLED has been reported with the red emitter PtOEP achieving 4% EQE[14] as shown in **Figure 1.23**. Since then, considerable efforts have been made to improve the red phosphorescent emitters. A variety of ligands has been developed with the objective of facilitating the radiative decay of MLCT states and suppressing the TTA process[99]. One notable example is $Pt(fprpz)_2$, which was reported by Chi et al. in 2016[100]. This compound exhibited the highest EQE (24%) emission at near infrared (NIR) wavelengths. In 2018, Wong et al. reported the highest EQE value (28%) for Ir(III)-based red PhOLEDs using PyThIr with the emission peak at 604 nm, which incorporated a strong electron-deficient effect of the diarylboron group and a notable electron-transporting capacity[101].

In 1999, Forrest and colleagues reported a phosphorescent OLED (PhOLED) with a peak EQE of 8% using a green emitter fac-Ir(ppy)$_3$[102]. Subsequent research has focused on derivatives of bis- and tri-cyclometallated Ir(III) complexes[103]. One of the most remarkable green OLEDs with 32.3% EQE was reported in 2014[104], which employed Ir(ppy)$_2$tmd (ppy = 2-phenylpyridine, tmd = 2,2,6,6-tetramethylheptane-3,5-diketonate) as a green emitter. The high EQE was the result of a combination of a high PLQY of 96% and its 78% horizontal dipole ratio. In addition to the success of Ir-based complexes, Pt (platinum)-based complexes have demonstrated comparable performance. In 2015, several pincer Pt(II) complexes with different ligands were reported by Che and colleagues[105]. The phosphorescent emitter [Pt(tBuPh-C^N^N-Qu)][C≡CC$_6$F$_5$] exhibited an EQE of 22.8% and green emission with CIE coordinates of (0.368,0.598). Moreover, a novel class of metal complexes, including alkynyl Au(III)[106] and three-coordinate Cu(I) complexes[107], has been synthesized with remarkable optical properties, and their strongly luminescent performance has been demonstrated.

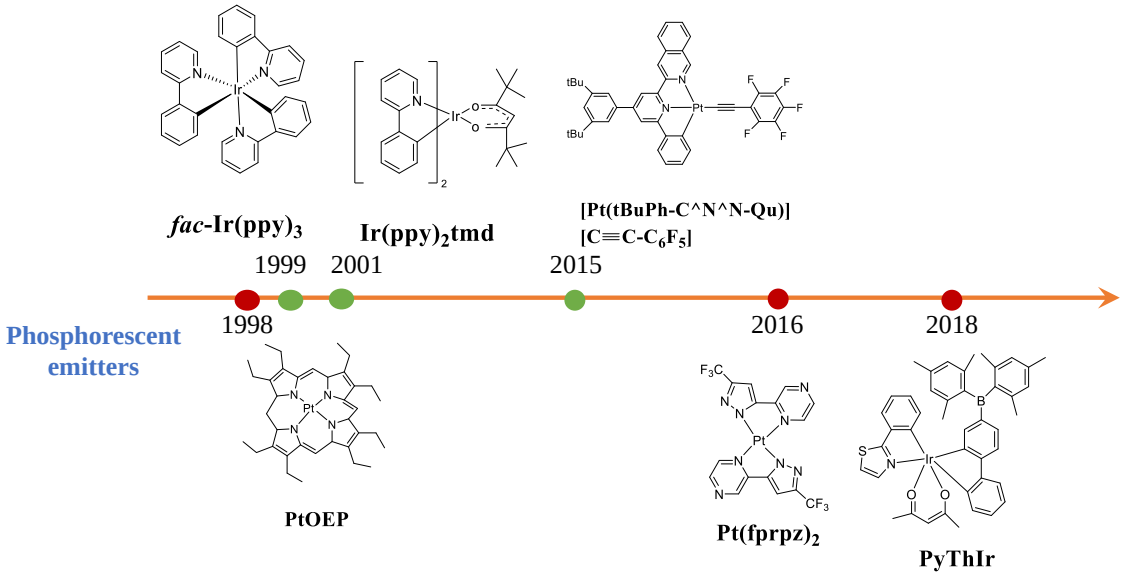

Figure 1.23: A selection of red and green OLED emitters based on phosphorescent molecules.

The blue phosphorescent emitters emerged around 1999 when Forrest and coworkers observed electroluminescence from the triplet emitting OLEDs based on FIrpic with an EQE of 5.7%[108]. As shown in in **Figure 1.24**, Kim and colleagues reported a noteworthy development in the realm of deep blue PhOLED with Ir-2, which demonstrated an impressive EQE of 31.9% within a doped matrix comprising mCBP and TSPO1, although no device lifetime data was mentioned[109]. Additionally, another blue PhOLED incorporating an electroplex host (mCBP and SiCzTrz) coupled with Ir(cb)$_3$ was reported with an EQE of 27.6% and emission CIE coordinates of (0.12, 0.13). Notably, the device showcased a half-lifetime (LT_{50}) of 170 hours, attributed to the high polaron stability of the host materials[110]. Pt complexes have emerged as competitive alternatives for phosphorescent emitters. A significant breakthrough occurred in 2014 by Li and co-workers, PtON7-dtb with a rigid tetradentate structure showed a deep blue emission peak at 451 nm, along with a remarkable narrow FWHM of 20 nm and the associated PH-OLED realized an EQE of 24.8%[111]. Subsequent enhancements in stability were accomplished through minor adjustments to tetradentate Pt complexes. Specifically, the blue emitter PtON-TBBI demonstrated notable performance in a PH-OLED, incorporating an exciplex host matrix (SiCzCz:SiTrzCz2). This configuration not only yielded a high EQE of 25.4% but also exhibited a remarkable lifetime LT_{95} of 150 hours[112]. Furthermore, other heavy atoms such as Cu-based complexes have also been incorporated

in phosphorescent OLEDs. Although these emitters showed limited EQE of 9%, their performance is hindered by inadequate device stability[113].

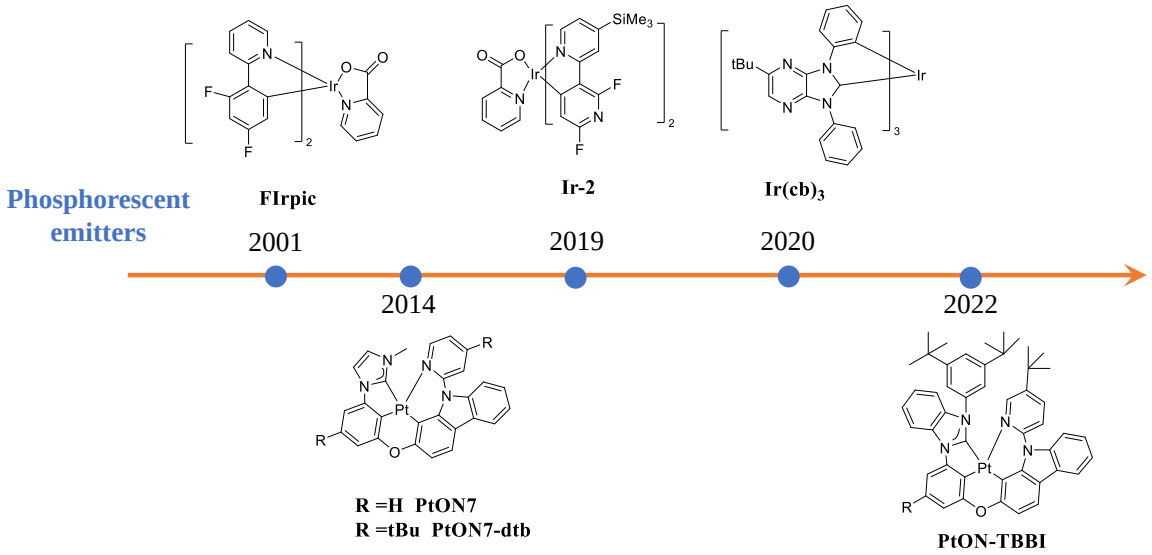

Figure 1.24: A selection of blue OLED emitters based on phosphorescent molecules.

In summary, both Ir and Pt phosphorescent emitters have demonstrated high efficiency in multicolor emission, with IQE approaching 100% and EQE exceeding 25%. Noteworthy enhancements in device performance have been achieved through the integration of various ligand structures, optimized host matrix, and adjacent layers, which have drawn continuous attention to PhOLEDs in pursuit of stability and high performance. However, the incorporation of heavy-metal atoms raises concerns regarding cost and environmental implications, particularly in the context of large-scale production for subsequent market expansion. Last but not the least, the performance of the phosphorescent emitter is intricately linked to its interactions with the surrounding host matrix. Especially for blue emitters, the matrix is required to have a large bandgap and high triplet energy (approximately ~3 eV) to prevent the loss channel of triplet transfer from the emitter to the host material[114]. However, the elevated energy levels associated with host triplets pose a challenge, as they can be detrimental to many bonds in organic semiconductors. This complication adds an additional layer of complexity in the search for a compatible host matrix for PhOLEDs[110].

1.3.3 Thermally activated delayed fluorescence (TADF)

TADF emitters, the third generation emitters, are widely acknowledged as the most promising mechanism for highly efficient OLEDs due to achieving 100% IQE without heavy metal atoms[115]. Molecular design frequently involves the careful separation of the HOMO and LUMO with minimal overlap, resulting in a narrow energy gap (<0.2 eV) between the S_1 and T_1. This facilitates the efficient endothermic up-conversion of T_1 to S_1 at room temperature. The Boltzmann distribution relation is aptly applied to describe the rate constant for RISC (k_{RISC}):

$$k_{\mathrm{RISC}} \propto \exp\left(-\frac{\Delta E_{\mathrm{ST}}}{k_{\mathrm{B}}T}\right) \qquad (1.21)$$

In 2012, the first class of TADF emitters with multiple carbazolyl units as donor groups and benzonitriles as acceptor groups, published by Adachi and co-workers[17], are generally considered as the milestone in TADF emitter development. The green emitter 4CzIPN as depicted in **Figure 1.25** showed an outstanding device performance with EQE of 19.3%, proving an efficient TADF mechanism in achieving both singlet and triplet exciton harvesting. The same year, the first class of blue TADF emitters was published by the same group, which demonstrated a deep blue emission at 423 nm and EQE of 9.9% by incorporating the emitter DTC-DPS into a DPEPO host matrix[116]. Subsequent years witnessed rapid advancements in molecular design strategies and associated improvements in TADF OLEDs.

A noteworthy example in 2014 is the device employing DMAC-DPS as the blue emitter, achieving an EQE of 19.5% with emission centered at 470 nm[117], which was the first time that TADF blue emitters surpassed the performance of phosphorescent OLEDs by addressing efficiency roll-off issues. TADF emitters featuring similar rod-shaped Donor-Acceptor (D-A) structures gained prominence, for example DMAC-TRZ [118](26.5% @ 490 nm) and spiroAC-TRZ[119] (36.7% @ 480 nm). Another remarkable emitter named CzDBA was reported in 2018, which shows a typical D-A-D structure possessing carbazole and 9,10-dihydro-9,10-diboraanthracene groups as donor and acceptor. The OLED based on CzDBA achieved a record-high EQE of 37.8% due to the very small ΔE_{ST} and 100% PLQY when doped in a host matrix.

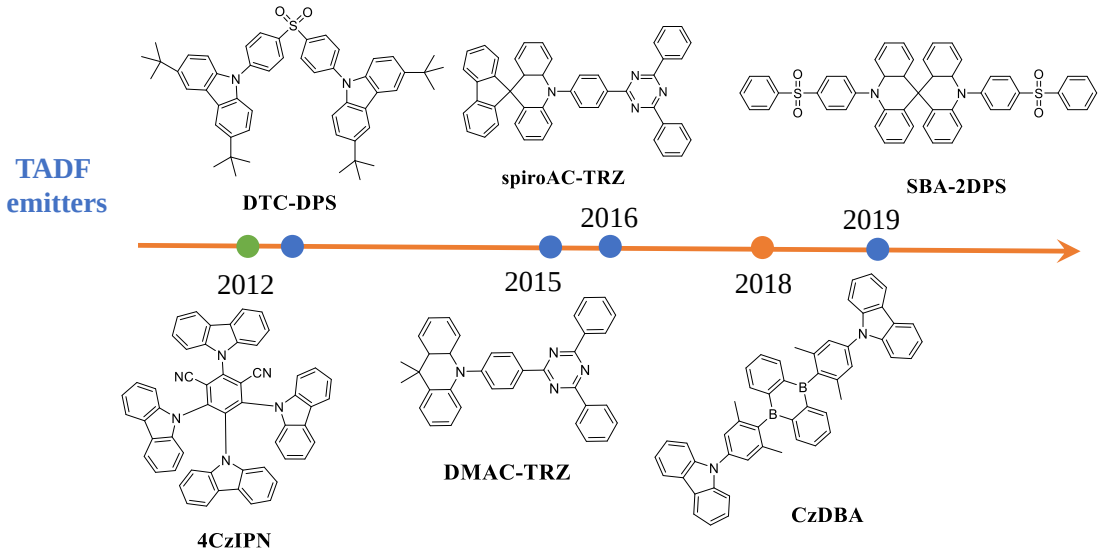

Figure 1.25: The third generation OLED emitters based on TADF molecules.

However, most of the emitters at that time encountered challenges related to color purity, as blue emitters reflected in CIE y-coordinates frequently exceeding 0.2. A transformative development occurred in 2019 when Yang's group reported the emitter SBA2DPS, which exhibited exceptional performance in an OLED with EQE of 25.5% and emission peak at 467 nm[120]. Notably, it was stated as the superior efficiency as compared to the majority of TADF OLED with y-coordinates below 0.2. This milestone marked a significant improvement in addressing color purity concerns within the realm of TADF emitters.

The subsequent consideration pertains to device stability for TADF OLEDs, which is typically discussed in conjunction with the choice of the host matrix[121]. Despite the prevalent design of TADF emitters within a purely organic structure, they commonly contend with the pronounced concentration-quenching effect. This necessitates a stringent requirement for a wide bandgap and stable host to ensure prolonged operational durability. For instance, commonly used host materials such as DPEPO and

mCBP-CN with high triplet energy contribute to most of the high efficiency of blue OLEDs, though the phosphine oxide-based structure (DPEPO) has intrinsic poor stability. A comparative analysis was conducted with the mCBP-CN host, wherein an OLED utilizing BDpyInCz as the emitter demonstrated an LT_{80} of 6h with a tiny compromise of EQE (13.6%), while a DPEPO host OLED as a reference showed LT_{80} of only 8 minutes[122]. This underscores the critical role of the host matrix in influencing the stability of TADF OLEDs, with careful consideration regarding its own chemical stability and the impact on charge balance within the EML.

1.3.4 Hyperfluorescence (HF)

Based on the aforementioned reports, achieving a harmonious combination of high efficiency, narrow emission spectra, and satisfactory stability appears to be a formidable challenge for a simple TADF system. To address this issue, the sensitization strategy has been introduced as a promising avenue to construct hyperfluorescent OLEDs, presenting itself as a viable and experimental approach worthy of exploration[123]. The proposed mechanism involves the incorporation of a TADF-type assistant as a dopant into the host matrix, serving as a sensitizer through its TADF properties, which facilitates energy transfer to the terminal emitter. Simultaneously, the terminal emitter with rapid radiative decay and narrowed EL spectrum characteristics emits as the final process.

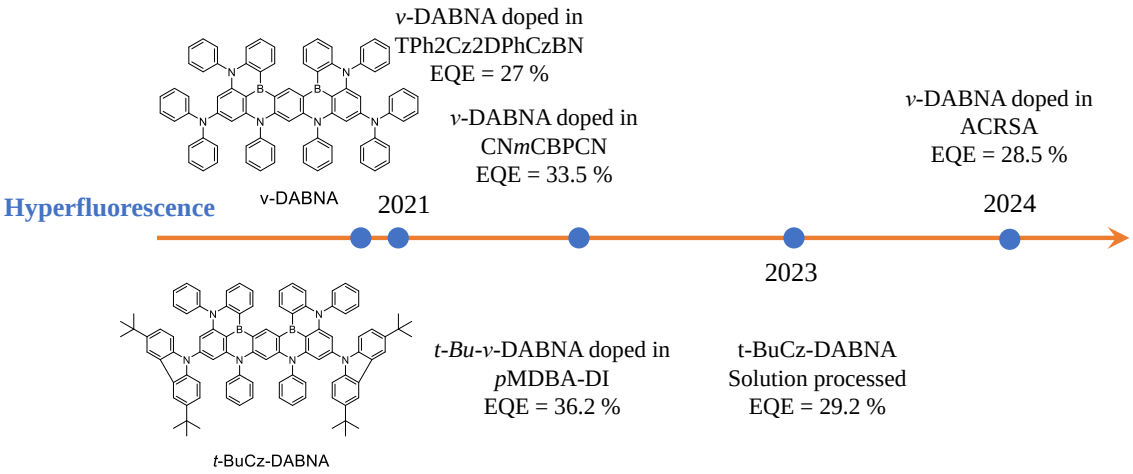

Figure 1.26: A selection of emitters applied in Hyperfluorescence OLEDs.

A successful example of HF-OLED with blue emission was documented in 2021 (**Figure 1.26**), employing an Emissive Layer (EML) composed of v-DABNA:TPh2Cz2DPhCzBN:mCBP[123]. The resulting device exhibited an impressive EQE of 27% and CIE coordinates of (0.15, 0.20). Notably, the device demonstrated an LT_{95} of 11 hours, which represents a significant improvement for blue TADF OLEDs. However, it is mentioned that the charge trapping effect induced by the terminal emitter may pose challenges to achieving optimal charge balance and overall device stability. At the same time, studies on efficient TADF sensitizers or terminal emitter have also gained massive attention[124–126]. For example, a HF-OLED was reported in 2022 using a different TADF sensitizer, pMDBA-DI, with an EQE of 36.2% and CIE coordinates of (0.13,0.20) and LT_{50} of 440 hours[127].

The examples provided serve as compelling evidence, indicating that the segregation of exciton harvesting and emission on distinct photoactive compounds prove effective in enhancing device stability without a trade-off in efficiency. The successful implementation of this strategy in HF-OLEDs

underscores its potential to address challenges related to charge balance and stability, thereby contributing to the advancement of more robust and efficient organic light-emitting devices

1.4 Device architectures

1.4.1 Multilayer OLEDs

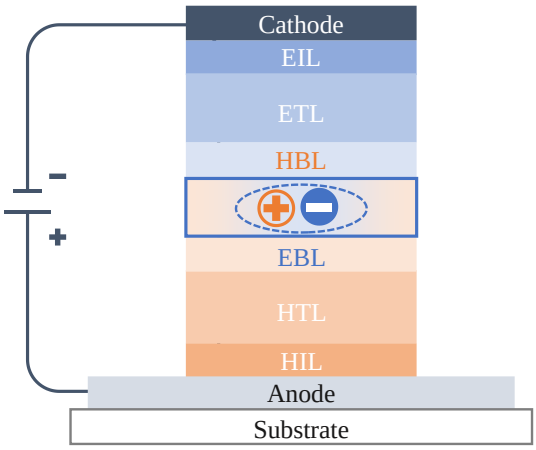

Figure 1.27: Representative multi-layer device structures for OLEDs with bottom emission.

A breakthrough in the development of OLED device structure was achieved by Tang and VanSlyke in 1987[10], when they demonstrated a double-layer OLED resulting in a significant drop in operating voltage. Since then, multilayer strategy was widely developed over the next years.

A typical multilayer OLED is depicted in **Figure 1.27** with bottom emission, comprising seven functional layers sandwiched between two electrodes. Since one electrode must be transparent to allow photons to escape, the metallic cathode positioned on top is highly reflective, while the anode on the glass substrate serves as the pathway for light emission. In this configuration, Indium tin oxide (ITO) is commonly used as the transparent anode, especially when pre-patterned on a glass substrate with a low refractive index. However, ITO has intrinsic limitations[128]. Its high transmittance and low sheet resistance are achieved through high-temperature treatment on the glass substrate, which hinders its application in flexible devices. Hence, continued research into alternative transparent electrodes that can meet a wide range of requirements remains imperative[129,130].

Substantial functional layers have been inserted between the respective electrode and emissive layer, to enhance OLED performance, feature materials with suitable energy levels for charge carrier injection or superior mobility for charge carrier transport. Functional layers such as the hole injection layer (HIL), hole transporting layer (HTL), electron blocking layer (EBL), hole blocking layer (HBL), electron transport layer (ETL), and electron injection layer (EIL) have massively boosted the OLED developments within finely-designed multilayer device configurations. The sophisticated selection of these functional layers is paramount to achieving optimal device performance. Generally, electrons are injected from the cathode and EIL, transported via the ETL, through the emissive layer, and blocked by the EBL, while holes are injected from the anode and HIL, transported via the HTL, through the emissive layer, and blocked by the HBL. Charge carriers flow through and meet in the emissive layer, leading to the generation of excitons. These excitons can undergo two primary decay processes: radiative decay

(resulting in the emission of light) or non-radiative decay (dissipating energy as heat within the device). Ultimately, the emitted light traverses through the transparent layers and substrate to be perceived by the observer.

As such, the supply of electrons and holes to the central emissive layer could be balanced, with the blocking layers ensuring that all charges and excitons recombine within the emissive layer, and thereby maximizing the internal quantum efficiency for photon generation. Furthermore, the emissive layer could be placed at an optically optimal position within the multilayer stack, resulting in maximum light extraction from the optical microcavity. The development of the multilayer OLED architecture, along with the harvesting of triplet excitons with phosphorescent or thermally activated delayed fluorescence (TADF) emitters has led to OLEDs with high external quantum efficiencies (EQEs)[14,131], practically only limited by the light-outcoupling efficiency of typically 20-30%[132].

Despite the successful development of multilayer OLEDs, the multilayer architecture has some major drawbacks. Firstly, many organic materials and deposition steps are required to fabricate such an OLED, which is costly and excludes the possibility of inkjet-printed OLEDs. Second, all layers and materials have to work in conjunction, to accomplish effective charge injection, charge transport, and charge and exciton confinement within the emissive layer, which makes the design and material selection cumbersome. Third, the many heterojunctions in the device lead to voltage losses and may be potential sources of device degradation. Fourth, understanding of the device physics is complicated, since the many layers and heterojunctions introduce unknown parameters, such as heights of the internal barriers and charge transport properties, making the device analysis and optimization a trial-and-error process.

1.4.2 Single-layer OLEDs

Initially, OLEDs based on conjugated polymers were highly attractive due to their simple device structure, consisting of a single layer of emitter sandwiched between two electrodes as shown in **Figure 1.28**.

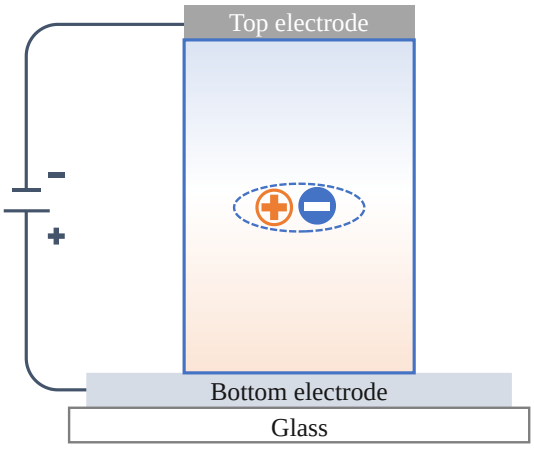

Figure 1.28: Representative single-layer device structures for OLEDs with bottom emission.

However, challenges arose when attempting to extend the application of this simple device design to most small molecular emitters. Firstly, it is challenging to inject holes and electrons from conventional

electrodes to wide bandgaps molecules, especially as used for blue emission. Considering ITO or PEDOT:PSS are often used for anode, finding a stable cathode material with high electron affinity (2~3 V) is the first challenge, with options like reactive metals (Ba, LiF) often requiring stringent encapsulation for decent OLED performance[133]. Secondly, most emitters with finely-tuned chemical structures often demonstrate superior hole transport characteristics but suffer from significant electron trapping, as their LUMO energy levels exceed the trap-free energy window[134]. This results in extreme imbalance in charge transport within the device.

In addition to the multilayer strategy, our research group is dedicated to developing single-layer OLEDs, achieving notable successes across a wide color range. This endeavor was initially showcased through a single-layer OLED featuring a yellow TADF emitter (CzDBA)[133], which was subsequently extended to green (DMAC-BP)[135] and blue (SpiroAc-TRZ)[136] emissions, all exhibiting device performance comparable to their multilayer counterparts but with much better stability. These achievements underscore the promise of single-layer OLEDs, particularly when accompanied by a comprehensive study of device physics, including charge injection and trapping.

Furthermore, the single-layer structure offers additional potential benefits. For instance, extending the recombination zone can reduce exciton concentration and mitigate exciton bimolecular interactions, thereby resulting in reduced efficiency roll-off and longer device lifetimes[137]. Admittedly, significant challenges remain in consolidating various requirements such as high PLQY, balanced transport, stability, and tunable color emission within a single layer. However, the simplicity inherent in the single-layer approach renders it a worthwhile pursuit for the future of OLED technology.

1.4.3 Extensive OLEDs structures

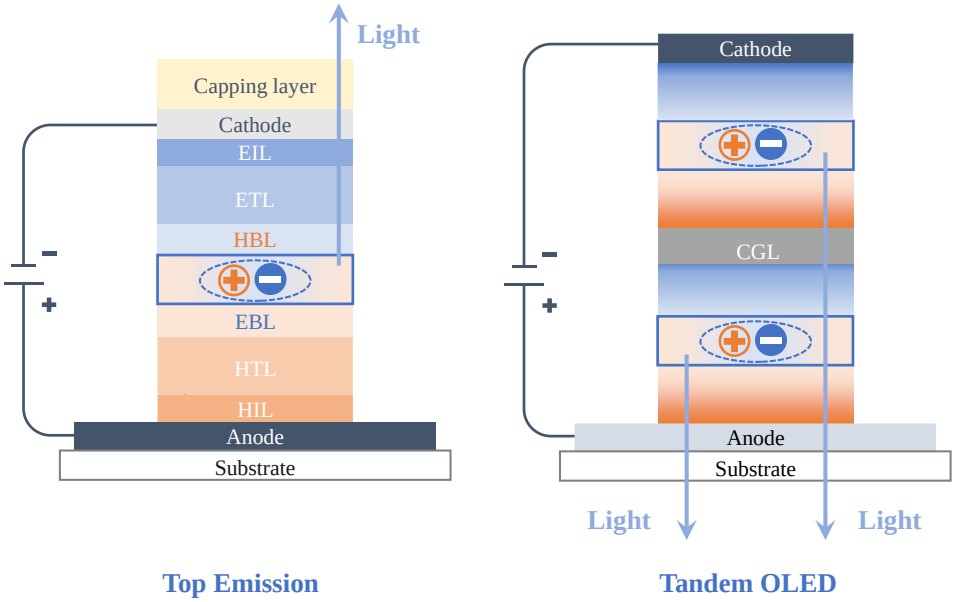

Figure 1.29: Representative device structures for OLEDs with top emission (left), and two units tandem configuration (right), some functional layers are omitted for simplification.

The other configuration shown in **Figure 1.29** (left) consists of a top-emission OLED[138], characterized by comparable functional layers but distinguished by a semi-transparent top cathode,

which is typically composed of thermally deposited metal films such as pure silver (Ag) or magnesium-silver (Mg:Ag) alloy. Indium tin oxide (ITO) is generally deemed unsuitable for the top electrode due to the detrimental impact of the sputtering process on the organic layers. However, recent advancements in sputtering technology have been reported, claiming reduced adverse effects on device performance[139]. In this arrangement, the bottom anode commonly comprises an opaque metallic electrode. This architectural configuration has seen widespread adoption in the OLED industry owing to the feasibility of integrating the driving panel beneath the bottom anode[140]. Furthermore, the performance of the top-emission OLED is intricately linked to the semi-transparent cathode, primarily due to the microcavity effect[138]. This phenomenon can amplify light out-coupling through constructive resonance and potentially exert a more pronounced influence on the angular dependence of light emission. It is noteworthy that a capping layer is frequently incorporated atop the device to fine-tune cavity resonance and transmittance, resulting in competitive efficiency compared to the bottom-emission structure.

The tandem OLED structure[141], as illustrated in **Figure 1.29** right, is composed of at least two emissive units, with a charge generation layer (CGL) situated between these individual units. Typically, the CGL comprises both p-type and n-type layers. In principle, OLEDs operate as current-driven devices, signifying that under the same current density, the EL intensity of a tandem OLED is directly proportional to the number of emissive units[142]. However, it is noteworthy that the applied voltage correspondingly increases due to the presence of multiple layers. In other words, a tandem OLED theoretically requires half the current density to achieve the equivalent luminance of an individual OLED unit, which holds potential appeal for enhancing device stability at high luminance levels. It is pertinent to highlight that the intermediate CGL significantly influences the efficacy of stacked units, as it governs internal charge generation and subsequent charge injection into adjacent EL units[142]. Moreover, the stringent transparency requirements of this layer pose considerable challenges in terms of material selection.

1.5 Device efficiency and energy loss

Once charges recombine inside the OLED emissive layer, the generated excitons undergo radiative decay to emit photons. Thus, for OLED efficiency determination, several concepts are introduced to quantify the energy loss processes and providing hints for improving OLED performance.

1.5.1 Internal quantum efficiency (IQE)

The Internal quantum efficiency (IQE) is defined as the ratio of the total number of photons generated to the total number of injected charge pairs, and can be expressed as:

$$\eta_{IQE} = \gamma \times \gamma_r \times \eta_{S/T} \times PLQY \qquad (1.22)$$

Here, γ is the "charge-balance factor" representing the fraction of injected electrons and holes which recombine to form excitons[143]. In an OLED with ohmic contacts for both electrons and holes, the high density of majority carriers near the ohmic contacts ensures that minority carriers cannot exit the device without recombining, resulting in negligible escape of charges, thus γ remains 1 in such situation. γ_r is the recombination factor that indicates the ratio of excitons generated via bimolecular recombination among all types of recombination, including trap assisted exciton quenching or interface recombination. In general, Langevin recombination is quite efficient in a trap-free OLED where most

of the injected charges generate excitons without trapping, which means the recombination factor $\gamma_r \approx 1$. In a trap-limited OLED, such as a conjugated polymer based LED, the value of γ_r can reduce significantly, reaching maximum values of 0.8 with increasing applied voltage due to the presence of electron traps[144].

As previously noted, excitons manifest in distinct ratios when subjected to either optical or electrical excitation. Thus, a spin factor $\eta_{S/T}$ is incorporated in the determination of the IQE for OLEDs, delineating the proportion of emissive excitons under electrical excitation. In the case of OLEDs employing conventional fluorescent emitters, the value of $\eta_{S/T}$ is 0.25. Conversely, for OLEDs utilizing phosphorescent emitters, $\eta_{S/T}$ attains a value of 1[75]. In a slightly complicated scenario like OLEDs based on Triplet-Triplet Annihilation (TTA)[145–148], $\eta_{S/T} = 0.25 + 0.75 \times 0.2 = 0.625$ [91,149]. The situation is more complex in the case of TADF OLEDs, where the non-radiative decay can affect both the PLQY as well as $\eta_{S/T}$, potentially resulting in lower values than 1[150].

1.5.2 External quantum efficiency (EQE)

$$\eta_{ext} = \eta_{IQE} \times \eta_{out} \tag{1.23}$$

The External quantum efficiency (EQE) is defined as the ratio of the total number of emitted photons reaching the user to the total number of injected charge pairs[77]. In the ideal scenario of OLEDs possessing 100% IQE, achieving unity EQE in OLED devices remains the ultimate goal. The main reason attributed to the difference between IQE and EQE is the photon trapping phenomenon within device architectures, where η_{out} denotes the out-coupling efficiency. Photons are initially generated within the emissive layer following charge recombination, then they may traverse through transparent layers such as ITO, or they may undergo reflection by metallic electrodes toward the glass substrate, before eventually reaching the ambient air.

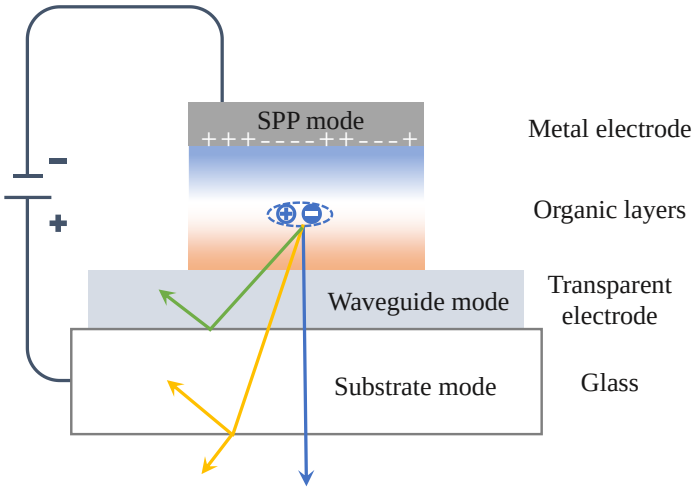

Figure 1.30: Energy trapping mechanism in OLEDs with functional layers omitted, the mismatch refractive indices induced substrate mode, waveguide mode and SPP mode at the metal/organic interface[151].

As illustrated in **Figure 1.30**, the pathway of light is influenced by variances in the refractive index (n) of each layer; for instance, organic layers typically exhibit a refractive index of 1.7~1.8, whereas the

glass substrate possesses a refractive index of 1.5, and air has a refractive index of 1.0[152]. One of the primary mechanisms leading to photon loss is total internal reflection within OLEDs, which occurs when photons propagate from a medium of higher refractive index to one of lower refractive index. This phenomenon manifests as waveguide modes when photons become trapped within the organic layer and ITO anode[153], and as substrate modes when photons are confined within the substrate[154]. Furthermore, an additional energy dissipation pathway arises when photons encounter the metallic electrode, as the electromagnetic waves of photons propagate along the metal surface, inducing a strong interaction with free electrons known as surface plasmon polariton (SPP) modes[155]. A simplified approximation has been proposed to estimate the out-coupling efficiency, assuming isotropic light emission within the emissive layer, where n represents the refractive index of the emissive layers (~1.7)[156].

$$\eta_{out} \approx \frac{1}{2n^2} \tag{1.24}$$

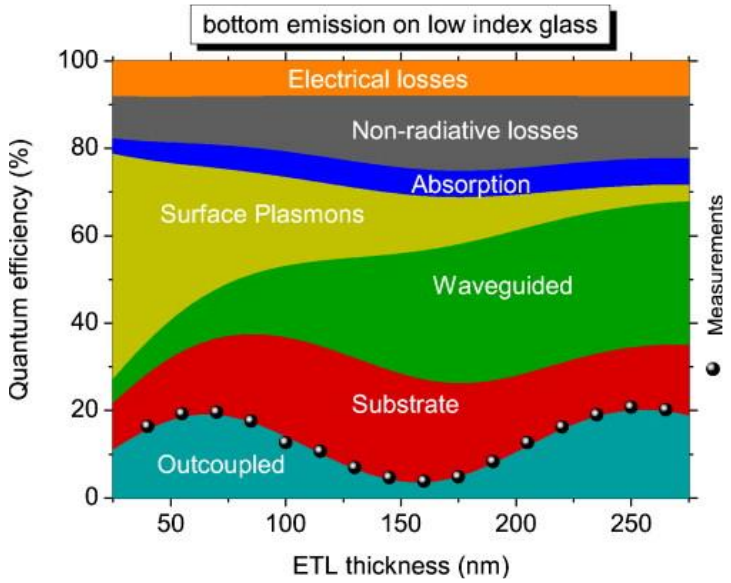

Figure 1.31: Quantification of different loss channels for conventional multilayer OLEDs with bottom emission, vary upon the change of n-doped ETL thickness. Reproduced from reference [159].

For state-of-the-art OLEDs the IQE can approach 100%, multiplied by an estimated η_{out} of approximately 20%[157,158], suggesting a theoretical upper limit for conventional OLED EQE around 20%. Consequently, enhancing OLED outcoupling efficiency has become a significant objective within this field, underscoring the importance of quantifying each energy loss mechanism. **Figure 1.31** presents an illustration of a bottom-emitting phosphorescent OLED as an example[159]. Given that most conventional OLEDs exhibit superior hole mobility compared to electron mobility, the position of charge recombination strongly correlates with the thickness of the electron transport layer (ETL) rather than the hole transport layer (HTL). **Figure 1.31** demonstrates the fraction of quantum efficiency with variations in the thickness of the n-doped ETL, showing the impact of the various optical effects. Within the first-order cavity effect regime (40-150 nm), the EQE within the out-coupled region peaks at 20% for an optimized ETL thickness of 60 nm, where around 20% loss is attributed to electrical, non-radiative, and absorptive losses, which are inherent to IQE limitations. Approximately 30% of the loss is attributed to surface plasmon polariton (SPP) modes, while another 30% is attributed to waveguide and substrate modes.

The analysis offers insights into potential avenues for improving OLED performance[160]. Firstly, optimizing emitter design to facilitate efficient radiative decay is essential for minimizing losses in IQE. Fine-tuning the orientation of emitter dipoles also enhances the light out-coupling efficiency. Additionally, enhancing photon extraction presents another effective solution. This may involve integrating micro-lens arrays to mitigate total internal reflection (TIR) at interfaces, thereby mitigating the predominant impact of substrate modes. Alternatively, carefully designing device stacks to account for second-order cavity effects can help to avoid the occurrence of surface plasmon polariton (SPP) modes, etc.

It is important to note, firstly, that the optical effects vary across different OLED device structures. For instance, the substrate mode is absent for top-emitting OLEDs as light does not traverse through the substrate (details are provided in Chapter 1.4.2). Secondly, such analyses meticulously exclude the electrical impact of the device, given that the highly n-doped ETL optimizes charge balance considerably. However, in a single-layer OLED, the recombination zone is closely linked to charge balance of the device, as previously mentioned. Furthermore, SPP modes are highly sensitive to the distance between recombination zone and the metallic electrode. Hence, the electrical efficiency is not solely correlated with the IQE but also with out-coupling efficiency in a single-layer OLED structure.

1.5.3 Efficiency roll-off

Another significant challenge in OLED development is the efficiency roll-off observed during device operation. This phenomenon signifies a decrease in OLED efficiency with increasing current density or luminance (**Figure 1.32**), primarily attributed to exciton interactions and unbalanced charge carriers. The dominant exciton interactions vary depending on the emission mechanism employed. For example, factors including singlet-singlet, singlet-triplet annihilation (STA) and singlet-polariton quenching (SPQ) are intensively studied in a fluorescence OLEDs. However, efficiency roll-off is more severe for phosphorescent and TADF OLEDs[161]. In a fluorescent OLED triplet-triplet annihilation (TTA) enhances the efficiency, which becomes more pronounced at higher current densities due to the increased triplet concentration, thus limiting the roll-off. In contrast, in phosphorescent and TADF OLEDS where ideally every triplet contributes to the light emission TTA is a loss process since now only one photon is generated from two triplets, resulting in a stronger roll-off. As a result, exciton interactions such as triplet-triplet annihilation (TTA) and triplet-polariton quenching (TPQ)[162] become more pronounced at higher current density compared to their fluorescent counterparts.

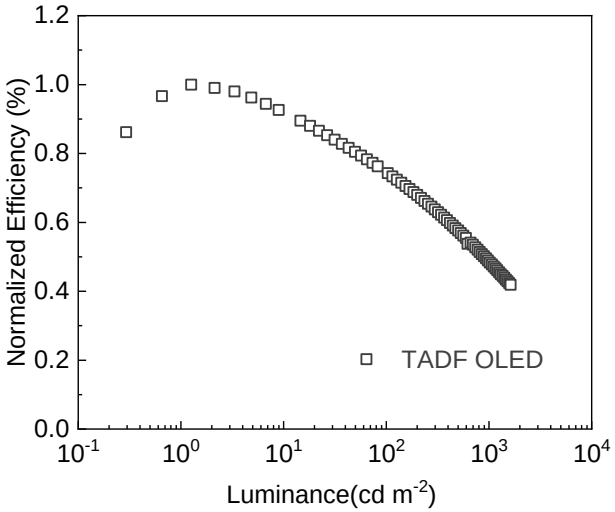

Figure 1.32: Simulated typical efficiency curves of a trap-free TADF OLED.

Given the high IQE of phosphorescent and TADF OLEDs, extensive research focuses on triplet-related exciton interactions to provide a detailed analysis of the associated photophysical processes. This research aims to unravel the correlations between molecular structure and inherent limitations of the final light output and the ultimate goal is to optimize emitter and device design. A general strategy for understanding the causes of roll-off involves quantifying the triplet lifetime and population, through photophysical studies in plain films comprising only the emissive layer. This approach is valuable because both parameters can be manipulated by engineering the emitter materials, which has been proved successfully in phosphorescent OLEDs.

A short description is offered to explain where triplets come and go. Firstly, triplets originate from singlets via intersystem crossing (ISC) with a rate constant k_{ISC} under photo-excitation. Although the initial conditions differ between optical and electrical excitation, we consider the rate constant to be identical for both. Once triplets are generated, they can undergo non-radiative decay (k_{nr}^{T}), radiative decay (k_{r}^{T}) or bimolecular processes such as STA, TTA, TPQ, as mentioned above. For phosphorescent OLEDs, higher k_{ISC} and k_{r}^{T} are desirable to increase triplet generation and fast consumption. For example, in Ir-complex based phosphorescent OLEDs a large radiative rate constant from triplets or a shorter triplet lifetime (~1μs), results in fast consumption of triplets, which is desired for minimizing the roll-off.

Especially for organic TADF emitters which have delayed fluorescence lifetimes ranging from 1 μs to 500 μs, there is a dominating pathway for triplet consumption known as reverse intersystem crossing (RISC) with a rate constant k_{RISC}[16]. Thus, an intrinsic competition exists among k_{ISC}, k_{RISC} and singlet radiative decay (k_{r}^{S}) for many TADF emitters, where k_{ISC} is substantially faster than k_{r}^{S}. On the one hand, increasing the k_{RISC} relative to k_{ISC} by minimizing the energy difference between singlet and triplet excited state (ΔE_{ST}) is advocated in the literature to maximize the triplet conversion to singlet and reduce roll off. On the other hand, maximizing the k_{r}^{S} is also a useful strategy achieved either by optimizing the chemical structure of the emitter itself or by introducing a doping system to facilitate other compounds that assist in singlet exit, such as in hyperfluorescent OLEDs[163]. It is worth noting that bimolecular processes of excitons are also a main mechanism of device degradation when considering intrinsic causes[164].

1.6 Scope of this thesis

This thesis seeks to advance the understanding of OLEDs within a single-layer structure, focusing on both molecular and device design aspects. As outlined earlier, a deeper exploration into the fundamental properties of wide bandgap emitters and device physics is crucial to achieving state-of-the-art performance in single-layer OLEDs. Addressing this challenge represents a significant bottleneck in the advancement of OLED technology.

In chapter 2, we address the electron trapping issue observed in blue-emitting organic semiconductors by optimizing the molecular organization. We adopted a molecular strategy involving spatial separation of HOMO and LUMO of TADF blue emitters aimed at eliminating charge trapping caused by extrinsic impurities. Experimental evidence demonstrates trap-free electron transport within 3CzTrz-F, wherein the donor serves as steric shielding units to safeguard the acceptor core, thereby protecting the electron transport from potential trapping effects.

In chapter 3, we applied a comprehensive analysis addressing the fundamental challenge encountered when applying a single-layer OLED structure to TADF emitters characterized by superior hole transport but afflicted with severe electron trapping. Broadly, TADF emitters with wide bandgaps and imbalanced charge transport often exhibit charge carriers recombining near the metal cathode, giving rise to the generation of SPP modes. This phenomenon leads to a significant loss of light output when ohmic injection takes place at both electrodes. To surmount this obstacle, we propose an inverted structure designed to relocate the charge recombination zone away from the metal electrode. By leveraging the superior hole transport characteristics inherent in these emitters, this approach effectively doubles the device efficiency within the single-layer structure.

In chapter 4, we advance the color purity in blue OLEDs within a single-layer structure by incorporating the hyperfluorescence strategy. We successfully achieved a pure blue emission in a single-layer OLED with an EQE of up to 19% by doping v-DABNA into a TADF matrix. Furthermore, we conducted a comprehensive study on the charge transport properties of the doping system, elucidating the hole-trapping effect induced by v-DABNA. Our findings not only demonstrate the efficacy of the hyperfluorescence strategy in single-layer OLEDs but also provide valuable insights into the electrical characteristics of the doping system. We believe that this charge transport analysis would further support the investigations of blue hyperfluorescent OLEDs.

References

1. Forrest, S. R. The path to ubiquitous and low-cost organic electronic appliances on plastic. *Nature* **428**, 911–8 (2004).
2. Blom, P. W. M. Polymer Electronics: To Be or Not to Be? *Adv. Mater. Technol.* **5**, 1–14 (2020).
3. Sun, L., Fukuda, K. & Someya, T. Recent progress in solution-processed flexible organic photovoltaics. *npj Flex. Electron.* **6**, 89 (2022).
4. Li, G., Zhu, R. & Yang, Y. Polymer solar cells. *Nat. Photonics* **6**, 153–161 (2012).
5. Chen, H. *et al.* A guest-assisted molecular-organization approach for >17% efficiency organic solar cells using environmentally friendly solvents. *Nat. Energy* **6**, 1045–1053 (2021).
6. Larson, C. *et al.* Highly stretchable electroluminescent skin for optical signaling and tactile sensing. *Science (80-.).* **351**, 1071–1074 (2016).
7. Tee, B. C. K., Wang, C., Allen, R. & Bao, Z. An electrically and mechanically self-healing composite with pressure- and flexion-sensitive properties for electronic skin applications. *Nat. Nanotechnol.* **7**, 825–832 (2012).
8. Zhang, Z. *et al.* High-brightness all-polymer stretchable LED with charge-trapping dilution. *Nature* **603**, 624–630 (2022).
9. Pope, M., Kallmann, H. P. & Magnante, P. Electroluminescence in organic crystals [16]. *J. Chem. Phys.* **38**, 2042–2043 (1963).
10. Tang, C. W. & Vanslyke, S. A. Organic electroluminescent diodes. *Appl. Phys. Lett.* **51**, 913–915 (1987).
11. Burroughes, J. H. *et al.* Light-emitting diodes based on conjugated polymers. *Nature* **347**, 539–541 (1990).
12. Kuik, M. *et al.* 25th Anniversary Article: Charge Transport and Recombination in Polymer Light-Emitting Diodes. *Adv. Mater.* **26**, 512–531 (2014).
13. Hong, G. *et al.* A Brief History of OLEDs—Emitter Development and Industry Milestones. *Adv. Mater.* **33**, (2021).
14. Baldo, M. A. *et al.* Highly efficient phosphorescent emission from organic electroluminescent devices. *Nature* **395**, 151 (1998).
15. Adachi, C., Baldo, M. A., Thompson, M. E. & Forrest, S. R. Nearly 100% internal phosphorescence efficiency in an organic light emitting device. *J. Appl. Phys.* **90**, 5048–5051 (2001).
16. Goushi, K., Yoshida, K., Sato, K. & Adachi, C. Organic light-emitting diodes employing efficient reverse intersystem crossing for triplet-to-singlet state conversion. *Nat. Photonics* **6**, 253–258 (2012).
17. Uoyama, H., Goushi, K., Shizu, K., Nomura, H. & Adachi, C. Highly efficient organic light-emitting diodes from delayed fluorescence. *Nature* **492**, 234–238 (2012).
18. Shi, Y.-Z. *et al.* Recent progress in thermally activated delayed fluorescence emitters for nondoped organic light-emitting diodes. *Chem. Sci.* **13**, 3625–3651 (2022).

19. Kallmann, H. & Pope, M. Bulk Conductivity in Organic Crystals. *Nature* **186**, 31–33 (1960).

20. Kallmann, H. & Pope, M. Positive hole injection into organic crystals. *J. Chem. Phys.* **32**, 300–301 (1960).

21. Sano, M., Pope, M. & Kallmann, H. Electroluminescence and band gap in anthracene. *J. Chem. Phys.* **43**, 2920–2921 (1965).

22. Mcginness, J., Corry, P. & Proctor, P. Amorphous semiconductor switching in melanins. *Science (80-.).* **183**, 853–855 (1974).

23. Köhler, A. & Bässler, H. *Electronic Processes in Organic Semiconductors*. (Wiley, 2015). doi:10.1002/9783527685172.

24. Brütting, W. Introduction to the Physics of Organic Semiconductors. in *Physics of Organic Semiconductors* 1–14 (Wiley, 2005). doi:10.1002/3527606637.ch.

25. Bredas, J.-L. Mind the gap! *Mater. Horiz.* **1**, 17–19 (2014).

26. Braun, S., Salaneck, W. R. & Fahlman, M. Energy-Level Alignment at Organic/Metal and Organic/Organic Interfaces. *Adv. Mater.* **21**, 1450–1472 (2009).

27. Brédas, J.-L., Beljonne, D., Coropceanu, V. & Cornil, J. Charge-Transfer and Energy-Transfer Processes in π-Conjugated Oligomers and Polymers: A Molecular Picture. *Chem. Rev.* **104**, 4971–5004 (2004).

28. Bronstein, H., Nielsen, C. B., Schroeder, B. C. & McCulloch, I. The role of chemical design in the performance of organic semiconductors. *Nat. Rev. Chem.* **4**, 66–77 (2020).

29. Fratini, S., Nikolka, M., Salleo, A., Schweicher, G. & Sirringhaus, H. Charge transport in high-mobility conjugated polymers and molecular semiconductors. *Nat. Mater.* **19**, 491–502 (2020).

30. Bässler, H. & Köhler, A. Charge Transport in Organic Semiconductors. in 1–65 (2011). doi:10.1007/128_2011_218.

31. Hulea, I. N. *et al.* Wide Energy-Window View on the Density of States and Hole Mobility in Poly(p-Phenylene Vinylene). *Phys. Rev. Lett.* **93**, 166601 (2004).

32. Miller, A. & Abrahams, E. Impurity Conduction at Low Concentrations. *Phys. Rev.* **120**, 745–755 (1960).

33. Baranovskii, S. D., Thomas, P. & Adriaenssens, G. J. The concept of transport energy and its application to steady-state photoconductivity in amorphous silicon. *J. Non. Cryst. Solids* **190**, 283–287 (1995).

34. Arkhipov, V. I., Wolf, U. & Bässler, H. Current injection from a metal to a disordered hopping system. II. Comparison between analytic theory and simulation. *Phys. Rev. B* **59**, 7514–7520 (1999).

35. Bässler, H. Charge Transport in Disordered Organic Photoconductors a Monte Carlo Simulation Study. *Phys. status solidi* **175**, 15–56 (1993).

36. Pasveer, W. F. *et al.* Unified Description of Charge-Carrier Mobilities in Disordered Semiconducting Polymers. *Phys. Rev. Lett.* **94**, 206601 (2005).

37. Craciun, N. I., Brondijk, J. J. & Blom, P. W. M. Diffusion-enhanced hole transport in thin polymer light-emitting diodes. *Phys. Rev. B* **77**, 035206 (2008).

38. Craciun, N. I., Wildeman, J. & Blom, P. W. M. Universal Arrhenius Temperature Activated

Charge Transport in Diodes from Disordered Organic Semiconductors. *Phys. Rev. Lett.* **100**, 056601 (2008).

39. Wetzelaer, G. A. H., Kuik, M., Nicolai, H. T. & Blom, P. W. M. Trap-assisted and Langevin-type recombination in organic light-emitting diodes. *Phys. Rev. B* **83**, 165204 (2011).

40. Wetzelaer, G. A. H., Kuik, M., Nicolai, H. T. & Blom, P. W. M. Trap-assisted and Langevin-type recombination in organic light-emitting diodes. *Phys. Rev. B* **83**, 165204 (2011).

41. Wetzelaer, G. A. H., Koster, L. J. A. & Blom, P. W. M. Validity of the Einstein Relation in Disordered Organic Semiconductors. *Phys. Rev. Lett.* **107**, 066605 (2011).

42. Mark, P. & Helfrich, W. Space-Charge-Limited Currents in Organic Crystals. *J. Appl. Phys.* **33**, 205–215 (1962).

43. Méhes, G., Sandanayaka, A. S. D., Ribierre, J.-C. & Goushi, K. Physics and Design Principles of OLED Devices. in *Handbook of Organic Light-Emitting Diodes* 1–73 (Springer Japan, 2020). doi:10.1007/978-4-431-55761-6_49-1.

44. Adachi, C. & Tsutsui, T. Molecular LED: Design Concept of Molecular Materials for High-Performance OLED. in *Organic Light-Emitting Devices* 43–69 (Springer New York, 2004). doi:10.1007/978-0-387-21720-8_2.

45. Ishii, H., Sugiyama, K., Ito, E. & Seki, K. Energy Level Alignment and Interfacial Electronic Structures at Organic/Metal and Organic/Organic Interfaces. *Adv. Mater.* **11**, 605–625 (1999).

46. Fahlman, M. *et al.* Interfaces in organic electronics. *Nat. Rev. Mater.* **4**, 627–650 (2019).

47. Simmons, J. G. Conduction in thin dielectric films. *J. Phys. D. Appl. Phys.* **4**, 202 (1971).

48. Blakesley, J. C. & Greenham, N. C. Charge transfer at polymer-electrode interfaces: The effect of energetic disorder and thermal injection on band bending and open-circuit voltage. *J. Appl. Phys.* **106**, (2009).

49. de Bruyn, P., van Rest, A. H. P., Wetzelaer, G. A. H., de Leeuw, D. M. & Blom, P. W. M. Diffusion-Limited Current in Organic Metal-Insulator-Metal Diodes. *Phys. Rev. Lett.* **111**, 186801 (2013).

50. Sze, S. M. & Ng, K. K. *Physics of Semiconductor Devices*. (Wiley, 2006). doi:10.1002/0470068329.

51. Arkhipov, V. I., Emelianova, E. V., Tak, Y. H. & Bässler, H. Charge injection into light-emitting diodes: Theory and experiment. *J. Appl. Phys.* **84**, 848–856 (1998).

52. Simmons, J. G. Richardson-Schottky Effect in Solids. *Phys. Rev. Lett.* **15**, 967–968 (1965).

53. Sze, S. M. & Ng, K. K. *Physics of Semiconductor Devices*. (Wiley, 2006). doi:10.1002/0470068329.

54. Appenzeller, J., Radosavljević, M., Knoch, J. & Avouris, P. Tunneling Versus Thermionic Emission in One-Dimensional Semiconductors. *Phys. Rev. Lett.* **92**, 048301 (2004).

55. Kotadiya, N. B. *et al.* Universal strategy for Ohmic hole injection into organic semiconductors with high ionization energies. *Nat. Mater.* **17**, 329–334 (2018).

56. de Bruyn, P., van Rest, A. H. P., Wetzelaer, G. A. H., de Leeuw, D. M. & Blom, P. W. M. Diffusion-Limited Current in Organic Metal-Insulator-Metal Diodes. *Phys. Rev. Lett.* **111**, 186801 (2013).

57. Robertson, J. H. Electrical transport in solids, with particular reference to organic semiconductors by K. C. Kao and W. Hwang. *Acta Crystallogr. Sect. B Struct. Crystallogr. Cryst. Chem.* **38**, 350–350 (1982).

58. Blom, P. W. M. & Vissenberg, M. C. J. M. Charge transport in poly(p-phenylene vinylene) light-emitting diodes. *Mater. Sci. Eng. R Reports* **27**, 53–94 (2000).

59. Wetzelaer, G. A. H. & Blom, P. W. M. Ohmic current in organic metal-insulator-metal diodes revisited. *Phys. Rev. B* **89**, 241201 (2014).

60. Blom, P. W. M., de Jong, M. J. M. & Vleggaar, J. J. M. Electron and hole transport in poly(p -phenylene vinylene) devices. *Appl. Phys. Lett.* **68**, 3308–3310 (1996).

61. Kuik, M. *et al.* Optical detection of deep electron traps in poly(p -phenylene vinylene) light-emitting diodes. *Appl. Phys. Lett.* **99**, (2011).

62. Nicolai, H. T., Mandoc, M. M. & Blom, P. W. M. Electron traps in semiconducting polymers: Exponential versus Gaussian trap distribution. *Phys. Rev. B* **83**, 195204 (2011).

63. Mandoc, M. M., de Boer, B., Paasch, G. & Blom, P. W. M. Trap-limited electron transport in disordered semiconducting polymers. *Phys. Rev. B* **75**, 193202 (2007).

64. Kotadiya, N. B., Mondal, A., Blom, P. W. M., Andrienko, D. & Wetzelaer, G.-J. A. H. A window to trap-free charge transport in organic semiconducting thin films. *Nat. Mater.* **18**, 1182–1186 (2019).

65. Albrecht, U. & Bässler, H. Langevin-Type Charge Carrier Recombination in a Disordered Hopping System. *Phys. status solidi* **191**, 455–459 (1995).

66. Blom, P. W. M., de Jong, M. J. M. & Breedijk, S. Temperature dependent electron-hole recombination in polymer light-emitting diodes. *Appl. Phys. Lett.* **71**, 930–932 (1997).

67. van der Holst, J. J. M., van Oost, F. W. A., Coehoorn, R. & Bobbert, P. A. Electron-hole recombination in disordered organic semiconductors: Validity of the Langevin formula. *Phys. Rev. B* **80**, 235202 (2009).

68. Kuik, M., Koster, L. J. A., Wetzelaer, G. A. H. & Blom, P. W. M. Trap-Assisted Recombination in Disordered Organic Semiconductors. *Phys. Rev. Lett.* **107**, 256805 (2011).

69. Shockley, W. & Read, W. T. Statistics of the Recombinations of Holes and Electrons. *Phys. Rev.* **87**, 835–842 (1952).

70. Wetzelaer, G. A. H., Van der Kaap, N. J., Koster, L. J. A. & Blom, P. W. M. Quantifying Bimolecular Recombination in Organic Solar Cells in Steady State. *Adv. Energy Mater.* **3**, 1130–1134 (2013).

71. Kittel, C. *Introduction to Solid State Physics*. *John Wiley & Sons, Inc*, (2005).

72. Köhler, A. & Bässler, H. What controls triplet exciton transfer in organic semiconductors? *J. Mater. Chem.* **21**, 4003–4011 (2011).

73. Köhler, A. & Bässler, H. Triplet states in organic semiconductors. *Mater. Sci. Eng. R Reports* **66**, 71–109 (2009).

74. *Physics of Organic Semiconductors*. (Wiley, 2005). doi:10.1002/3527606637.

75. Forrest, S. R. Exciton formation statistics under electrical injection in organic semiconductor thin films. *J. Lumin.* **110**, 378–383 (2004).

76. *Principles of Fluorescence Spectroscopy*. (Springer US, 2006). doi:10.1007/978-0-387-46312-4.

77. Van der Zee, B., Li, Y., Wetzelaer, G. A. H. & Blom, P. W. M. Efficiency of Polymer Light-Emitting Diodes: A Perspective. *Adv. Mater.* **34**, (2022).

78. Rörich, I. *et al.* Exciton Quenching due to Hole Trap Formation in Aged Polymer Light-Emitting Diodes. *Adv. Electron. Mater.* **6**, (2020).

79. Rörich, I., Mikhnenko, O. V., Gehrig, D., Blom, P. W. M. & Crăciun, N. I. Influence of Energetic Disorder on Exciton Lifetime and Photoluminescence Efficiency in Conjugated Polymers. *J. Phys. Chem. B* **121**, 1405–1412 (2017).

80. Köhler, A., & Bässler, H. *Electronic processes in organic semiconductors: An introduction*. (2015).

81. Braun, D. & Heeger, A. J. Visible light emission from semiconducting polymer diodes. *Appl. Phys. Lett.* **58**, 1982–1984 (1991).

82. Spreitzer, H., Becker, H., Kreuder, W., Kluge, E. & Schenk, H. From a Reaction Mechanism to New Ppv's for High Performance Polymer-Leds. *MRS Proc.* **560**, 297 (1999).

83. Neher, D. Polyfluorene Homopolymers: Conjugated Liquid-Crystalline Polymers for Bright Blue Emission and Polarized Electroluminescence. *Macromol. Rapid Commun.* **22**, 1365–1385 (2001).

84. Tang, C. W., VanSlyke, S. A. & Chen, C. H. Electroluminescence of doped organic thin films. *J. Appl. Phys.* **65**, 3610–3616 (1989).

85. Chen, C.-T. Evolution of Red Organic Light-Emitting Diodes: Materials and Devices. *Chem. Mater.* **16**, 4389–4400 (2004).

86. Toguchi, S., Morioka, Y., Ishikawa, H., Oda, A. & Hasegawa, E. Novel red organic electroluminescent materials including perylene moiety. *Synth. Met.* **111**–**112**, 57–61 (2000).

87. Huang, J., Su, J.-H. & Tian, H. The development of anthracene derivatives for organic light-emitting diodes. *J. Mater. Chem.* **22**, 10977 (2012).

88. Adachi, C., Tsutsui, T. & Saito, S. Blue light-emitting organic electroluminescent devices. *Appl. Phys. Lett.* **56**, 799–801 (1990).

89. Zheng, C.-J. *et al.* Highly efficient non-doped deep-blue organic light-emitting diodes based on anthracene derivatives. *J. Mater. Chem.* **20**, 1560 (2010).

90. Arakane, T. *et al.* 5.1: Fluorescent RGB OLEDs with High Performance. *SID Symp. Dig. Tech. Pap.* **37**, 37 (2006).

91. Chiang, C. *et al.* Ultrahigh Efficiency Fluorescent Single and Bi-Layer Organic Light Emitting Diodes: The Key Role of Triplet Fusion. *Adv. Funct. Mater.* **23**, 739–746 (2013).

92. Tang, X. *et al.* Efficient Nondoped Blue Fluorescent Organic Light-Emitting Diodes (OLEDs) with a High External Quantum Efficiency of 9.4% @ 1000 cd m −2 Based on Phenanthroimidazole−Anthracene Derivative. *Adv. Funct. Mater.* **28**, (2018).

93. Hsin, M.-H. *et al.* P-161: 89.3% Lifetime Elongation of Blue TTA-OLED with Assistant Host. *SID Symp. Dig. Tech. Pap.* **47**, 1727–1729 (2016).

94. Lin, B.-Y. *et al.* P-174: 16.1-times Elongation of Operation Lifetime in a Blue TTA-OLED by

using New ETL and EML Materials. *SID Symp. Dig. Tech. Pap.* **48**, 1928–1931 (2017).

95. Xie, F. *et al.* Achieving Simultaneously Ultrahigh Brightness, Extremely Low Efficiency Roll-Off and Ultralong Lifetime of Blue Fluorescent OLEDs by Using Donor–Acceptor-Type 5,9-Diarylamine Functionalized Pyrenes. *Adv. Opt. Mater.* **11**, (2023).

96. Tankelevičiūtė, E., Samuel, I. D. W. & Zysman-Colman, E. The Blue Problem: OLED Stability and Degradation Mechanisms. *J. Phys. Chem. Lett.* **15**, 1034–1047 (2024).

97. Baldo, M. A., Thompson, M. E. & Forrest, S. R. High-efficiency fluorescent organic light-emitting devices using a phosphorescent sensitizer. *Nature* **403**, 750–753 (2000).

98. Yang, X., Zhou, G. & Wong, W.-Y. Functionalization of phosphorescent emitters and their host materials by main-group elements for phosphorescent organic light-emitting devices. *Chem. Soc. Rev.* **44**, 8484–8575 (2015).

99. Xiang, H., Cheng, J., Ma, X., Zhou, X. & Chruma, J. J. Near-infrared phosphorescence: materials and applications. *Chem. Soc. Rev.* **42**, 6128 (2013).

100. Tuong Ly, K. *et al.* Near-infrared organic light-emitting diodes with very high external quantum efficiency and radiance. *Nat. Photonics* **11**, 63–68 (2017).

101. Yang, X. *et al.* Diarylboron-Based Asymmetric Red-Emitting Ir(III) Complex for Solution-Processed Phosphorescent Organic Light-Emitting Diode with External Quantum Efficiency above 28%. *Adv. Sci.* **5**, (2018).

102. Baldo, M. A., Lamansky, S., Burrows, P. E., Thompson, M. E. & Forrest, S. R. Very high-efficiency green organic light-emitting devices based on electrophosphorescence. *Appl. Phys. Lett.* **75**, 4–6 (1999).

103. Choy, W. C. H., Chan, W. K. & Yuan, Y. Recent Advances in Transition Metal Complexes and Light-Management Engineering in Organic Optoelectronic Devices. *Adv. Mater.* **26**, 5368–5399 (2014).

104. Kim, K., Moon, C., Lee, J., Kim, S. & Kim, J. Highly Efficient Organic Light-Emitting Diodes with Phosphorescent Emitters Having High Quantum Yield and Horizontal Orientation of Transition Dipole Moments. *Adv. Mater.* **26**, 3844–3847 (2014).

105. Chow, P. *et al.* Luminescent Pincer Platinum(II) Complexes with Emission Quantum Yields up to Almost Unity: Photophysics, Photoreductive C□C Bond Formation, and Materials Applications. *Angew. Chemie Int. Ed.* **54**, 2084–2089 (2015).

106. Au, V. K.-M. *et al.* High-Efficiency Green Organic Light-Emitting Devices Utilizing Phosphorescent Bis-cyclometalated Alkynylgold(III) Complexes. *J. Am. Chem. Soc.* **132**, 14273–14278 (2010).

107. Hashimoto, M. *et al.* Highly Efficient Green Organic Light-Emitting Diodes Containing Luminescent Three-Coordinate Copper(I) Complexes. *J. Am. Chem. Soc.* **133**, 10348–10351 (2011).

108. Adachi, C. *et al.* Endothermic energy transfer: A mechanism for generating very efficient high-energy phosphorescent emission in organic materials. *Appl. Phys. Lett.* **79**, 2082–2084 (2001).

109. Shin, H. *et al.* Controlling Horizontal Dipole Orientation and Emission Spectrum of Ir Complexes by Chemical Design of Ancillary Ligands for Efficient Deep-Blue Organic Light-Emitting Diodes. *Adv. Mater.* **31**, (2019).

110. Jung, M., Lee, K. H., Lee, J. Y. & Kim, T. A bipolar host based high triplet energy electroplex for an over 10 000 h lifetime in pure blue phosphorescent organic light-emitting diodes. *Mater. Horizons* **7**, 559–565 (2020).

111. Fleetham, T., Li, G., Wen, L. & Li, J. Efficient "Pure" Blue OLEDs Employing Tetradentate Pt Complexes with a Narrow Spectral Bandwidth. *Adv. Mater.* **26**, 7116–7121 (2014).

112. Sun, J. *et al.* Exceptionally stable blue phosphorescent organic light-emitting diodes. *Nat. Photonics* **16**, 212–218 (2022).

113. Hamze, R. *et al.* Eliminating nonradiative decay in Cu(I) emitters: >99% quantum efficiency and microsecond lifetime. *Science (80-.).* **363**, 601–606 (2019).

114. Van Der Zee, B., Li, Y., Wetzelaer, G. J. A. H. & Blom, P. W. M. Triplet-Polaron-Annihilation-Induced Degradation of Organic Light-Emitting Diodes Based on Thermally Activated Delayed Fluorescence. *Phys. Rev. Appl.* **18**, 1 (2022).

115. Wong, M. Y. & Zysman-Colman, E. Purely Organic Thermally Activated Delayed Fluorescence Materials for Organic Light-Emitting Diodes. *Adv. Mater.* **29**, (2017).

116. Zhang, Q. *et al.* Design of Efficient Thermally Activated Delayed Fluorescence Materials for Pure Blue Organic Light Emitting Diodes. *J. Am. Chem. Soc.* **134**, 14706–14709 (2012).

117. Zhang, Q. *et al.* Efficient blue organic light-emitting diodes employing thermally activated delayed fluorescence. *Nat. Photonics* **8**, 326–332 (2014).

118. Tsai, W.-L. *et al.* A versatile thermally activated delayed fluorescence emitter for both highly efficient doped and non-doped organic light emitting devices. *Chem. Commun.* **51**, 13662–13665 (2015).

119. Lin, T. *et al.* Sky-Blue Organic Light Emitting Diode with 37% External Quantum Efficiency Using Thermally Activated Delayed Fluorescence from Spiroacridine-Triazine Hybrid. *Adv. Mater.* **28**, 6976–6983 (2016).

120. Zeng, X. *et al.* High-efficiency pure blue thermally activated delayed fluorescence emitters with a preferentially horizontal emitting dipole orientation via a spiro-linked double D–A molecular architecture. *J. Mater. Chem. C* **7**, 10851–10859 (2019).

121. Chatterjee, T. & Wong, K. Perspective on Host Materials for Thermally Activated Delayed Fluorescence Organic Light Emitting Diodes. *Adv. Opt. Mater.* **7**, (2019).

122. Ihn, S. *et al.* An Alternative Host Material for Long-Lifespan Blue Organic Light-Emitting Diodes Using Thermally Activated Delayed Fluorescence. *Adv. Sci.* **4**, (2017).

123. Chan, C. Y. *et al.* Stable pure-blue hyperfluorescence organic light-emitting diodes with high-efficiency and narrow emission. *Nat. Photonics* **15**, 203–207 (2021).

124. Jeon, S. O. *et al.* High-efficiency, long-lifetime deep-blue organic light-emitting diodes. *Nat. Photonics* **15**, 208–215 (2021).

125. Nguyen, T. B., Nakanotani, H., Hatakeyama, T. & Adachi, C. The Role of Reverse Intersystem Crossing Using a TADF-Type Acceptor Molecule on the Device Stability of Exciplex-Based Organic Light-Emitting Diodes. *Adv. Mater.* **32**, (2020).

126. Zhang, K. *et al.* Carbazole-Decorated Organoboron Emitters with Low-Lying HOMO Levels for Solution-Processed Narrowband Blue Hyperfluorescence OLED Devices. *Angew. Chemie Int. Ed.* **62**, (2023).

127. Naveen, K. R. *et al.* Achieving High Efficiency and Pure Blue Color in Hyperfluorescence Organic Light Emitting Diodes using Organo-Boron Based Emitters. *Adv. Funct. Mater.* **32**, (2022).

128. Gaynor, W. *et al.* Color in the Corners: ITO-Free White OLEDs with Angular Color Stability. *Adv. Mater.* **25**, 4006–4013 (2013).

129. Kee, S. *et al.* Highly Deformable and See-Through Polymer Light-Emitting Diodes with All-Conducting-Polymer Electrodes. *Adv. Mater.* **30**, (2018).

130. Li, N. *et al.* Efficient and bright organic light-emitting diodes on single-layer graphene electrodes. *Nat. Commun.* **4**, 2294 (2013).

131. Schwartz, G., Reineke, S., Rosenow, T. C., Walzer, K. & Leo, K. Triplet harvesting in hybrid white organic light-emitting diodes. *Adv. Funct. Mater.* **19**, 1319–1333 (2009).

132. Uoyama, H., Goushi, K., Shizu, K., Nomura, H. & Adachi, C. Highly efficient organic light-emitting diodes from delayed fluorescence. *Nature* **492**, 234–238 (2012).

133. Kotadiya, N. B., Blom, P. W. M. & Wetzelaer, G.-J. A. H. Efficient and stable single-layer organic light-emitting diodes based on thermally activated delayed fluorescence. *Nat. Photonics* **13**, 765–769 (2019).

134. Kotadiya, N. B., Mondal, A., Blom, P. W. M., Andrienko, D. & Wetzelaer, G.-J. A. H. A window to trap-free charge transport in organic semiconducting thin films. *Nat. Mater.* **18**, 1182–1186 (2019).

135. Sachnik, O. *et al.* Single-Layer Organic Light-Emitting Diode with Trap-Free Host Beats Power Efficiency and Lifetime of Multilayer Devices. *Adv. Mater.* (2024) doi:10.1002/adma.202311892.

136. Sachnik, O. *et al.* Single-Layer Blue Organic Light-Emitting Diodes With Near-Unity Internal Quantum Efficiency. *Adv. Mater.* **35**, (2023).

137. Li, Y. *et al.* Enhanced Operational Stability by Cavity Control of Single-Layer Organic Light-Emitting Diodes Based on Thermally Activated Delayed Fluorescence. *Adv. Mater.* **35**, (2023).

138. Hofmann, S. *et al.* Top-emitting organic light-emitting diodes: Influence of cavity design. *Appl. Phys. Lett.* **97**, (2010).

139. Kim, S. K., Lampande, R. & Kwon, J. H. Technical status of top-emission organic light-emitting diodes. *J. Inf. Disp.* **22**, 115–126 (2021).

140. Mathine, D. L. *et al.* Heterogeneously integrated organic light-emitting diodes with complementary metal–oxide–silicon circuitry. *Appl. Phys. Lett.* **76**, 3849–3851 (2000).

141. Liao, L. S., Klubek, K. P. & Tang, C. W. High-efficiency tandem organic light-emitting diodes. *Appl. Phys. Lett.* **84**, 167–169 (2004).

142. Fung, M., Li, Y. & Liao, L. Tandem Organic Light-Emitting Diodes. *Adv. Mater.* **28**, 10381–10408 (2016).

143. Tsutsui, T., Aminaka, E., Lin, C. P. & Kim, D.-U. Extended molecular design concept of molecular materials for electroluminescence: sublimed–dye films, molecularly doped polymers and polymers with chromophores. *Philos. Trans. R. Soc. London. Ser. A Math. Phys. Eng. Sci.* **355**, 801–814 (1997).

144. Kuik, M., Koster, L. J. A., Dijkstra, A. G., Wetzelaer, G. A. H. & Blom, P. W. M. Non-radiative

recombination losses in polymer light-emitting diodes. *Org. Electron.* **13**, 969–974 (2012).

145. Chitraningrum, N., Chu, T.-Y., Huang, P.-T., Wen, T.-C. & Guo, T.-F. The triplet-triplet annihilation process of triplet to singlet excitons to fluorescence in polymer light-emitting diodes. *Org. Electron.* **62**, 505–510 (2018).

146. Kondakov, D. Y., Pawlik, T. D., Hatwar, T. K. & Spindler, J. P. Triplet annihilation exceeding spin statistical limit in highly efficient fluorescent organic light-emitting diodes. *J. Appl. Phys.* **106**, (2009).

147. Sinha, S. & Monkman, A. P. Delayed electroluminescence via triplet–triplet annihilation in light emitting diodes based on poly[2-methoxy-5-(2′-ethyl-hexyloxy)-1,4-phenylene vinylene]. *Appl. Phys. Lett.* **82**, 4651–4653 (2003).

148. Wallikewitz, B. H., Kabra, D., Gélinas, S. & Friend, R. H. Triplet dynamics in fluorescent polymer light-emitting diodes. *Phys. Rev. B* **85**, 045209 (2012).

149. Di, D. *et al.* Efficient Triplet Exciton Fusion in Molecularly Doped Polymer Light-Emitting Diodes. *Adv. Mater.* **29**, (2017).

150. Sem, S. *et al.* Determining non-radiative decay rates in TADF compounds using coupled transient and steady state optical data. *J. Mater. Chem. C* **10**, 4878–4885 (2022).

151. Zou, S.-J. *et al.* Recent advances in organic light-emitting diodes: toward smart lighting and displays. *Mater. Chem. Front.* **4**, 788–820 (2020).

152. Gu, G. *et al.* High-external-quantum-efficiency organic light-emitting devices. *Opt. Lett.* **22**, 396 (1997).

153. Hauss, J., Bocksrocker, T., Riedel, B., Lemmer, U. & Gerken, M. On the interplay of waveguide modes and leaky modes in corrugated OLEDs. *Opt. Express* **19**, A851 (2011).

154. Greenham, N. C., Friend, R. H. & Bradley, D. D. C. Angular Dependence of the Emission from a Conjugated Polymer Light-Emitting Diode: Implications for efficiency calculations. *Adv. Mater.* **6**, 491–494 (1994).

155. Ritchie, R. H. Plasma Losses by Fast Electrons in Thin Films. *Phys. Rev.* **106**, 874–881 (1957).

156. Kim, J.-S., Ho, P. K. H., Greenham, N. C. & Friend, R. H. Electroluminescence emission pattern of organic light-emitting diodes: Implications for device efficiency calculations. *J. Appl. Phys.* **88**, 1073–1081 (2000).

157. Lee, Y.-J. *et al.* A high-extraction-efficiency nanopatterned organic light-emitting diode. *Appl. Phys. Lett.* **82**, 3779–3781 (2003).

158. Bulović, V. *et al.* Weak microcavity effects in organic light-emitting devices. *Phys. Rev. B* **58**, 3730–3740 (1998).

159. Meerheim, R., Furno, M., Hofmann, S., Lüssem, B. & Leo, K. Quantification of energy loss mechanisms in organic light-emitting diodes. *Appl. Phys. Lett.* **97**, (2010).

160. Brütting, W., Frischeisen, J., Schmidt, T. D., Scholz, B. J. & Mayr, C. Device efficiency of organic light-emitting diodes: Progress by improved light outcoupling. *Phys. status solidi* **210**, 44–65 (2013).

161. van der Zee, B., Li, Y., Wetzelaer, G. A. H. & Blom, P. W. M. Origin of the Efficiency Roll-Off in Single-Layer Organic Light-Emitting Diodes Based on Thermally Activated Delayed Fluorescence. *Adv. Opt. Mater.* **9**, (2021).

162. van der Zee, B., Li, Y., Wetzelaer, G.-J. A. H. & Blom, P. W. M. Triplet-Polaron-Annihilation-Induced Degradation of Organic Light-Emitting Diodes Based on Thermally Activated Delayed Fluorescence. *Phys. Rev. Appl.* **18**, 064002 (2022).

163. Diesing, S., Zhang, L., Zysman-Colman, E. & Samuel, I. D. W. A figure of merit for efficiency roll-off in TADF-based organic LEDs. *Nature* **627**, 747–753 (2024).

164. Scholz, S., Kondakov, D., Lüssem, B. & Leo, K. Degradation Mechanisms and Reactions in Organic Light-Emitting Devices. *Chem. Rev.* **115**, 8449–8503 (2015).

2. Elimination of Charge-Carrier Trapping by Molecular Design

In this chapter, we have investigated a molecular strategy where the HOMO and LUMO orbitals are spatially separated on different parts of the molecules. By tuning their stacking by modification of the chemical structure, the LUMO orbitals can be spatially protected from impurities that cause electron trapping, increasing the electron current by orders of magnitude. In this way, the trap-free window can be substantially broadened, opening a path towards large band gap organic semiconductors with balanced and trap-free transport[1].

This chapter was 2023 published as "Elimination of charge-carrier trapping by molecular design" in Nature Materials, Volume 22, September 2023, page 1114-1120, together with Oskar Sachnik , Dehai Dou, Constantin Haese, Naomi Kinaret, Kun-Han Lin, Denis Andrienko, Martin Baumgarten, Robert Graf, Gert-Jan A. H. Wetzelaer, Jasper J. Michels & Paul W. M. Blom.

Author Contributions

O.S. and D.D. synthesized the molecules, O.S. and X.T. carried out the electrical characterization, N.K. and K.-H.L. performed the computational modelling, C.H. and R.G. carried out the SS-NMR experiments, D.A. supervised the computational work, M.B. and J.J.M. supervised the synthetic work, G.-J.A.H.W. supervised the electrical characterization and P.W.M.B. initiated and supervised the overall project and wrote the manuscript with input from the others.

2.1 Introduction

Organic semiconductors often show relatively poor charge transport properties compared with their inorganic counterparts. There are two fundamental reasons limiting their charge transport: the first one is a low carrier mobility, arising from the fact that organic molecules are held together by weak van der Waals and π–π non-covalent forces, making them susceptible to energetic and structural disorder. As a result, the charge transport is governed by hopping between localized states, which is less efficient than band conduction in crystalline inorganic semiconductors[2]. In the past three decades, by optimizing the molecular packing[3], mobility values exceeding 10 $cm^2\ V^{-1}\ s^{-1}$ for both n- and p-type organic semiconductors have been reported[4]. A second reason leading to poor charge transport, even for high mobility materials, is trapping of charge carriers by impurities. In this case, only a small fraction of the injected carriers contribute to the charge transport. Trapping of either electrons or holes is the main cause of imbalanced transport in organic semiconductors[5,6]. Recently, an energy window was identified, inside which organic semiconductors are not susceptible to charge trapping. Trap-free bipolar charge transport can be accomplished when the electron affinity (EA) of the organic semiconductor is higher than 3.5 eV and the ionization energy (IE) is lower than 6.0 eV[7]. This universal window, which applies to semiconducting polymers as well as to small molecules, indicates that the extrinsic charge traps in organic semiconductors share a common origin. Electron trapping has been attributed to oxygen-related impurities[8], whereas hole traps are linked to water clusters[7,9]. Furthermore, next to oxygen, also omnipresent water has been proposed as a possible source for electron trapping[10]. However, the relation between processing conditions and trapping is still under debate.

The fundamental question remains whether it is possible to achieve intrinsic trap-free transport of both electrons and holes for organic semiconductors with a band gap larger than the trap-free window

of 2.5 eV. In that case, either the HOMO or LUMO or both are outside the trap-free window. As trapping is detrimental to the efficiency of single-layer OLEDs[11], trap-free ambipolar charge transport is a prerequisite to achieve highly efficient devices[12–14]. The limited width of 2.5 eV of the energy window implies that for large band gap materials, as used in blue OLEDs, it is fundamentally not possible to obtain trap-free transport of both carriers, thus preventing the realization of efficient printed single-layer blue OLEDs in future. In addition, for multilayer blue OLEDs, the imbalance in electron and hole transport in the large band gap host[15] leads to an unevenly distributed emission zone as well as to unwanted interactions of excess holes with excitons, which decrease the operational lifetime of the device[16,17].

Here we demonstrate an approach on how simultaneous trap-free electron and hole transport can be intrinsically accomplished in wide band gap organic semiconductors through molecular design. The basic idea is to use donor–acceptor based molecules, with the LUMO localized on the acceptor part and the HOMO localized on the donor part. By shielding the acceptor core where the electron transport takes place with the donor moieties, the interaction of impurities with the LUMO leading to electron trapping can be effectively blocked. This work therefore represents a universal molecular bottom-up concept to eliminate the detrimental effects of external impurities in organic semiconductors.

2.2 Molecular structure

The basic structure of a series of blue-emitting molecules presented in this study consists of a triazine (Trz) acceptor linked to carbazole (Cz) donor(s) by a phenylene linker (Figure 2.1). Triazene based materials are well known for their efficient transport of electrons[18]. A similar combination of triazine and carbazole has been employed as blue emitter exploiting thermally activated delayed fluorescence, where it was demonstrated that an increase of the amount of Cz donor units from two to three led to an enhancement of the OLED efficiency[19]. However, the individual charge transport properties of these CzTrz based materials were not addressed.

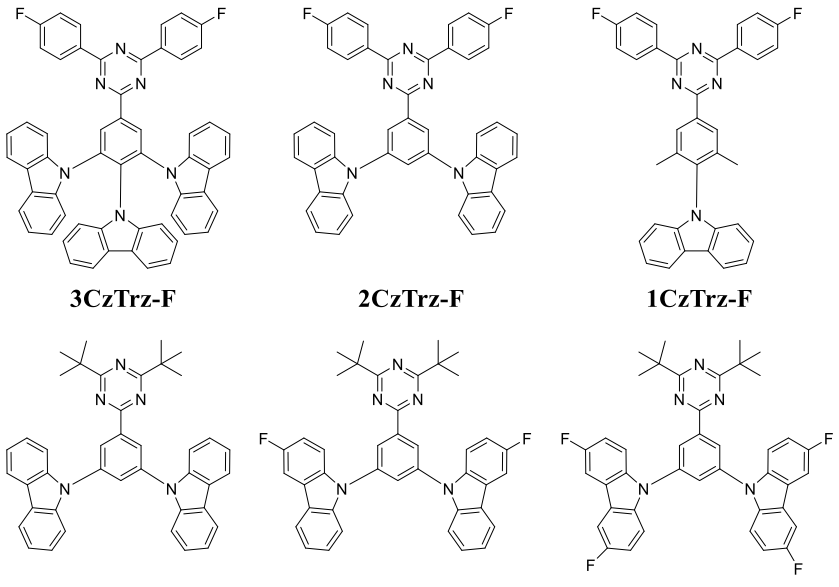

a) b)

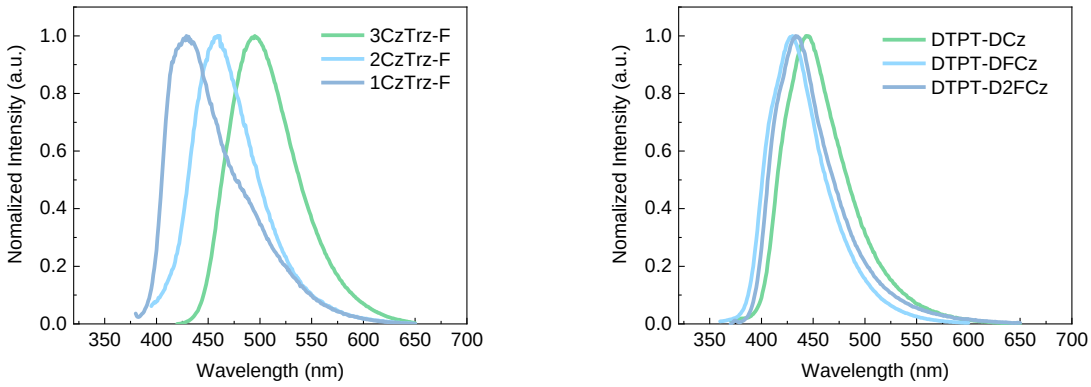

Figure 2.1: Molecular structures and photoluminescence spectra in film. Structural formulas of top series consisting of 3CzTrz-F, 2CzTrz-F and 1CzTrz-F, and bottom series consisting of DTPT-DCz, DTPT-DFCz and DTPT-D2FCz[1]. Reproduced from reference [1].

Two series of organic semiconducting blue emitters have been synthesized and were investigated in terms of electron transport and molecular arrangement in thin films. In the first series the blue emitters share the same triazine acceptor but a different number of donating carbazole units (bridged by a phenylene linker): 9-(4-(4,6-bis(4-fluorophenyl)-1,3,5-triazin-2-yl)phenyl)-9H-carbazole (1CzTrz-F), 9,9'-(5-(4,6-bis(4-fluorophenyl)-1,3,5-triazin-2-yl)-1,3-phenylene)bis(9H-carbazole) (2CzTrz-F), 9,9',9''-(5-(4,6-bis(4-fluorophenyl)-1,3,5-triazin-2-yl)benzene-1,2,3-triyl)tris(9H-carbazole) (3CzTrz-F).

The second series consists of the same triazine acceptor and two donating carbazole units, also bridged by a phenylene linker, but with different number of fluorine substituents on the carbazole unit: 9,9'-(5-(4,6-di-tert-butyl-1,3,5-triazin-2-yl)-1,3-phenylene)bis(9H-carbazole) (DTPT-DCz), 9,9'-(5-(4,6-di-tert-butyl-1,3,5-triazin-2-yl)-1,3-phenylene)bis(3-fluoro-9H-carbazole) (DTPT-DFCz) and 9,9'-(5-(4,6-di-tert-butyl-1,3,5-triazin-2-yl)-1,3-phenylene)bis(3,6-difluoro-9H-carbazole (DTPT-D2FCz).

First, we measured the IE and EA of the six compounds using a combination of ultraviolet photoelectron spectroscopy (UPS) and cyclic-voltammetry measurements (**Table 2.1**). The IE of this series of molecules of ~ 5.8 eV is within the trap-free energy window, meaning that trap-free hole transport is expected for all of these compounds[7]. The measured EA amounts to 3.0 ± 0.3 eV for all compounds, clearly well below the value of 3.6 eV for trap-free electron transport[7]. Hence, in contrast to the hole current, the electron current is expected to be strongly trap-limited in all cases based on energy-level considerations.

Table 2.1 Experimental ionization energy (IE) from ultraviolet photoelectron spectroscopy (UPS) and cyclic voltammetry (CV), and electron affinity (EA) (CV)[1].

	IE (CV) (eV)	EA (CV) (eV)	IE (UPS) (eV)	E_g (CV) (eV)
3CzTRZ-F	-5.67	-3.11	-5.90	2.56
2CzTRZ-F	-5.80	-3.12	-5.56	2.68
1CzTRZ-F	-5.61	-2.84	-5.95	2.77
DTPT-DCz	-5.49	-2.61	-5.70	3.10
DTPT-DFCz	-5.74	-2.77	-5.79	3.10
DTPT-2FCz	-5.82	-2.81	-5.89	3.10

2.3 Results and discussion on 1-3CzTrz-F

2.3.1 Charge transport study

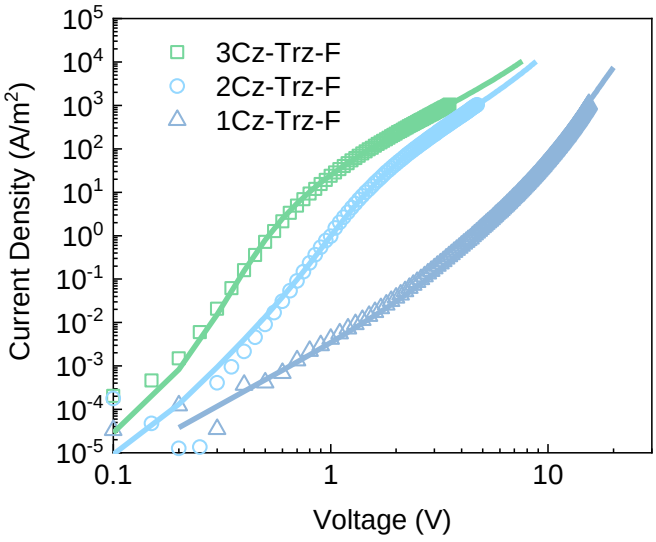

Figure 2.2: Electron current of 1-3CzTrz-F compounds. Experimental (symbols) and simulated (lines) J–V characteristics of the fluorinated compounds 3CzTrz-F (118 nm), 2CzTrz-F (91 nm) and 1CzTrz-F (95 nm)[1]. Reproduced from reference [1].

The electron transport in the emitters 1–3CzTrz-F series were investigated: the EAs as obtained from cyclic-voltammetry measurements (**Table 2.1**) range from 2.8 eV to 3.1 eV and are all far outside the trap-free window. Despite the fact that all molecules comprise the same donor and acceptor moieties, we observe a four to five orders of magnitude difference in the electron current density, depending on the number of donor substituents. Intriguingly, as shown in **Figure 2.2,** the electron current in 3CzTrz-F shows a quadratic dependence of the current on voltage, indicative of trap-free space-charge-limited electron transport, despite having its LUMO energy outside the trap-free window. The fact that the lower

current density for the other compounds is accompanied by an increased voltage dependence of the current indicates that the strong reduction in transport is caused by electron trapping[5].

However, the electron current of 1CzTrz-F is strongly reduced, showing a steep J–V curve with a slope of around 6 in the log J–log V plot. For the series an optimum electron current is reached for three Cz units, for which a nearly trap-free space-charge limited current ($J \sim V^2$) is measured. A further decrease in the number of Cz moieties results in more severe electron trapping. To quantify the trap density, the J–V characteristics are modelled (lines, **Figure 2.2**) with a previously developed drift-diffusion model[20]. The electron mobility is obtained from the quadratic trap-free regime observed for the 3CzTrz-F molecule and amounts to 7×10^{-9} m^2 V^{-1} s^{-1}. The currents of the other compounds are then described by the addition of electron traps, assuming a Gaussian energy distribution of trap states. The trap concentrations and transport parameters are given in **Table 2.2**, respectively. By studying the dependence on temperature (**Figure 2.3**), we confirmed that the observed difference of orders of magnitude in the electron current is not the result of a variation in injection barrier, since the ohmic contacts are realized by using a 1,3,5-Tris(1-phenyl-1H-benzimidazol-2-yl) benzene (TPBi) tunnel barrier to decouple the semiconductor from the electrode[21].

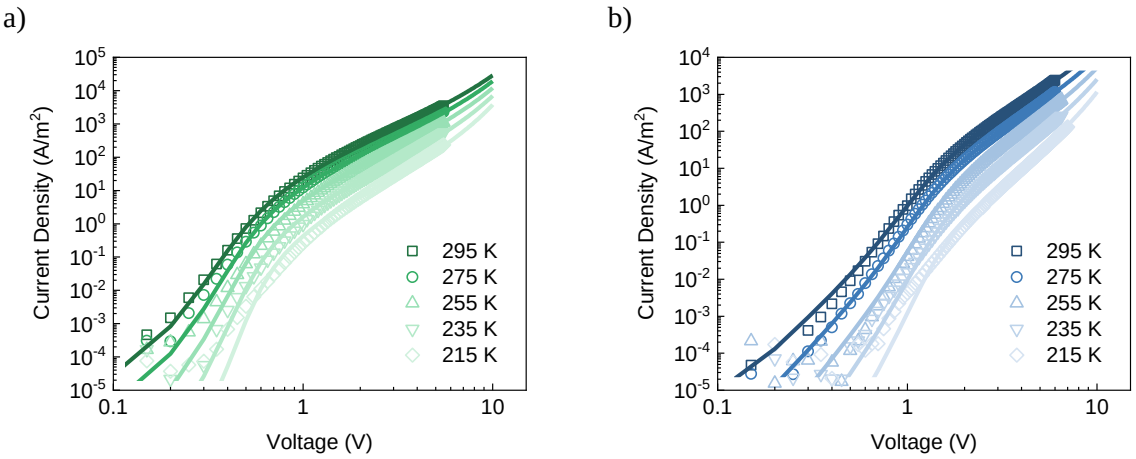

Figure 2.3: Temperature dependent electron transport of 3CzTrz-F and 2CzTrz-F. *J-V* characteristics of 3CzTrz-F (118 nm) (a) and 2CzTrz-F (91 nm) (b) electron-only devices as function of temperature. Symbols are experimental data and solid lines are fits with a numerical drift-diffusion model[1]. Reproduced from reference [1].

Table 2.2 Drift-diffusion modeling parameters for electron-only devices of 1-3CzTrz-F[1].

	1CzTrz-F	2CzTrz-F	3CzTrz-F
Trap density, N_t gauss ($\times 10^{22}$ m^{-3})	100	6.0	0.9
Trap depth, E_t (eV)	0.48	0.63	0.70
Width of Gaussian trap distribution, σ_t (eV)	0.10	0.10	0.10
Lattice constant EGDM, a ($\times 10^{-9}$ m)	1.60	1.40	1.80
DOS variance EGDM, σ (eV)	0.10	0.11	0.09
Mobility at 295 K, μ ($\times 10^{-10}$ m²/Vs)	8.12	4.15	27.92

2.3.2 Density of states (DOS) simulation of amorphous

To obtain more insight in the molecular mechanism of trapping we have as a next step computed the density of states (DOS) of the three 1–3CzTrz-F compounds assuming the films to be amorphous (disordered molecular arrangement), with traps due to molecular oxygen (**Table 2.3**). The calculated ionization energies (**Table 2.4**) agree well with the experimentally obtained numbers. However, for the fluorinated 1–3CzTrz-F compounds, the value of EA and distributions of O_2 do not notably vary, such that identical trapping is expected for all compounds (**Tables 2.4 and 2.5**). This is clearly in contrast with the strong variation in electron current study. This suggests that it is not only the energetics of the molecules being responsible for the observed large variation in electron transport of the 1-3CzTrz-F compounds. An open question is whether extrinsic electron trapping is also strongly dependent on the molecular arrangement of the molecules in the solid film. Of course, this can only be the case if the films are not fully amorphous but rather show molecular ordering to some extent, for instance in a coexisting phase comprising (nano-)crystalline domains[22,23].

Table 2.3 Concentration of interstitial oxygen gas in amorphous 1-3CzTrz-F materials[1].

	1CzTrz-F	2CzTrz-F	3CzTrz-F
Interstitial oxygen conc. (mmol dm^{-3})	112.9	91.0	71.8

Table 2.4 Material properties in amorphous phase of 1-3CzTrz-F[1].

	1CzTrz-F	2CzTrz-F	3CzTrz-F
μ_e (eV)	-1.971	-1.903	-2.036
σ_e (eV)	0.115	0.119	0.098
EA (eV)	-2.201	-2.131	-2.233
μ_h (eV)	-5.879	-6.085	-5.900
σ_h (eV)	0.210	0.113	0.139
IE (eV)	-5.459	-5.858	-5.622

Table 2.5 Oxygen trap levels in amorphous 1-3CzTrz-F[1].

	1CzTrz-F	2CzTrz-F	3CzTrz-F
μ_e (eV)	-2.014	-1.916	-1.942
σ_e (eV)	0.294	0.315	0.340
EA (eV)	-2.602	-2.546	-2.622

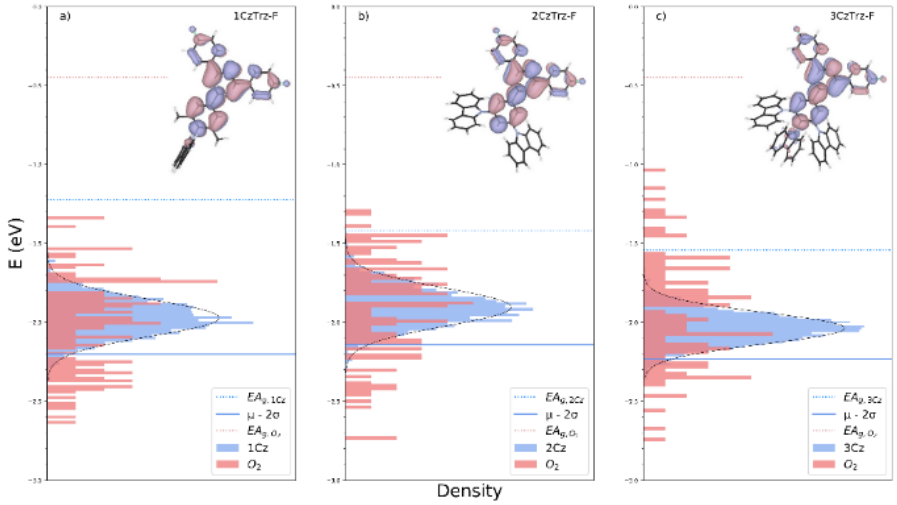

Figure 2.4: Calculated density-of-states distributions for amorphous 1-3CzTrz-F[1]. Reproduced from reference [1].

The density of states of electron affinity of molecular oxygen (red) and organic materials (blue; 1CzTrz-F, 2CzTrz-F and 3CzTrz-F) with amorphous morphology is shown in **Figure 2.4**. The dotted lines are the gas-phases electron affinity for molecular oxygen and organic materials. The blue solid line represents the energy μ_e -2σ_e, with μ_e corresponding to the average of the calculated solid-state EA values and σ_e the standard deviation of the Gaussian distribution, respectively (**Table 2.4**), the energy μ_e -2σ_e is expected to correspond to the onset of the solid-state EA from UPS measurements.

2.3.3 Molecular ordering by XRD

To investigate the molecular ordering in the compounds with three or fewer carbazole units, we subjected the fluorinated monocarbazole and tricarbazole species to a comparative analysis using two complementary experimental methods, namely, X-ray diffraction (XRD) and magic angle spinning (MAS) solid-state nuclear magnetic resonance (SS-NMR)[24,25]. XRD was applied to single crystals, grown by anti-solvent diffusion as described in Methods. The SS-NMR analysis was used to establish the extent of ordering in the evaporated thin film. The reason to select the 1CzTrz-F and 3CzTrz-F for this analysis is that the fluorine substituent provides for a highly sensitive marker, owing to the fact that its natural isotope (19F) has spin of +1/2[26]. Furthermore, the 1CzTrz-F and 3CzTrz-F show a few orders of magnitude difference in their electron transport, with the transport in 1CzTrz-F heavily trap limited and a nearly trap-free transport in 3CzTrz-F. In addition, we managed to grow crystals of sufficient quality for XRD of both 1CzTrz-F and 3CzTrz-F compounds.

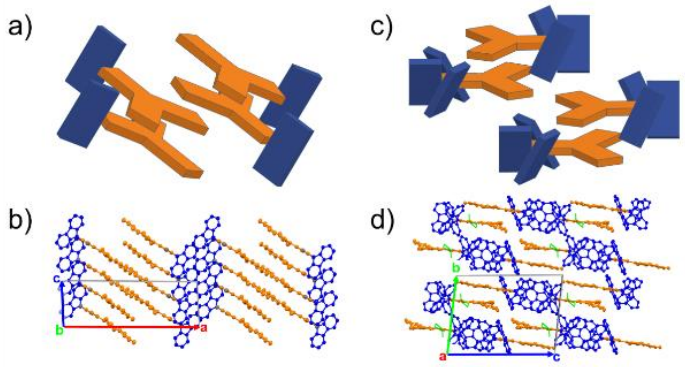

Figure 2.5: Molecular structures obtained from XRD. Crystal structures of the 1CzTrz-F (a,b) and 3CzTrz-F (c,d) compounds, determined by XRD. a,c, Diagrams of the two dimers of both crystallographic unit cells to show the molecular packing. b,d, Spatial arrangement of the acceptor–donor contacts in the 3D crystal structure. The triazine acceptor and the carbazole donor units are colored orange and blue, respectively. The green features in d indicate co-crystallized chloroform molecules[1]. Reproduced from reference [1].

To characterize the structure of the single crystals, XRD analysis revealed the space group for 1CzTrz-F to be P1 (monoclinic), with no co-crystallized solvent molecules. As displayed in **Figure 2.5** a,b, the unit cell contains four molecules, paired into two dimers with antiparallel stacking of the triazine planes and considerable spatial overlap between the outer phenyl groups. The distance between the molecular planes is 3.5 Å. The carbazole units are arranged in an angle close to 90° relative to the connecting phenyl ring, caused by the steric hindrance of the two ortho-methyl groups.

Furthermore, as shown in **Figure 2.5** a, the Cz units of the species within one dimer are rotated relative to each other by approximately 60° around the centres of the triazine rings. The three-dimensional arrangement leads to a structure with alternating two-dimensional layers of carbazole and triazine rings perpendicular to the crystallographic *a* axis. Dimer formation agrees with earlier work by Monkman et al[27]. who demonstrated that dimers are responsible for the spectral shifts observed in carbazole-based TADF emitters[27]. The 3CzTrz-F crystal structure falls in the P21/c space group (triclinic), showing solvent co-crystallization. Again, we encounter four molecules in a single unit cell showing a dimeric arrangement (**Figure 2.5** c.d).

However, now the dimers are formed by antiparallel molecular alignment, and the stacking involves not only the triazine rings but also the outer phenyl rings. The torsion angles of the carbazole groups are 120 ± 10°, possibly resulting from weak π–π interaction of neighboring units bound to the same phenyl ring. The stacking of neighboring molecules is slightly tilted, and the π systems of adjacent molecules do not perfectly superimpose. The stacking of neighboring molecular planes, however, connects molecules within a plane, forming a one-dimensional double layer of acceptor units along the crystallographic *a* axis. The distance between the molecular planes is 3.4 Å. In summary, 3CzTrz-F shows an inclined face-to-face stacking of the phenyl substituted triazine cores along the crystallographic *a* axis, which effectively may act as a 'tunnel' for electron transport, crowded by carbazole units. In contrast, in 1CzTrz-F such crowding is lacking. We therefore propose that the origin of the difference in the electron trapping between the monocarbazole and tricarbazole species is the result of the stacking geometry: 'open' for the monocarbazole species and 'closed' for the tricarbazole compounds, meaning that in the latter the electron transporting core is effectively shielded from interactions with extrinsic contaminants such as oxygen.

2.3.4 Molecular ordering by MAS SS-NMR

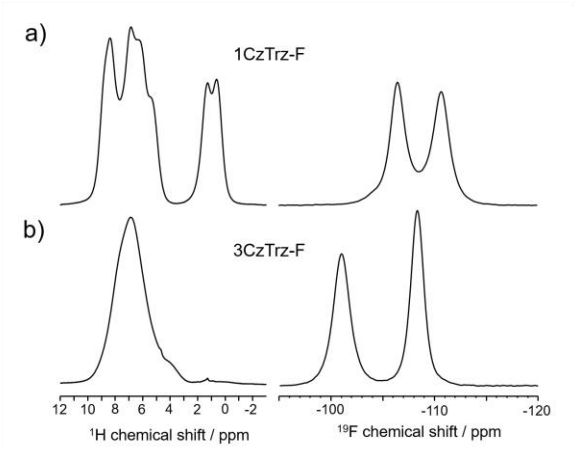

Figure 2.6: NMR spectra of the 1CzTrz-F and 3CzTrz-F compounds. 1H and 19F MAS spectra recorded at 50 kHz spinning speed of vapor deposited material of the compounds 1CzTrz-F (a) and 3CzTrz-F (b)[1]. Reproduced from reference [1].

In what follows, we confirm using MAS SS-NMR that molecular ordering indeed occurs in vapor-deposited material, supporting our explanation of differences in electron transport in terms of differences in molecular packing. The spectra of 1CzTrz-F (1H and 19F) and 3CzTrz-F (1H and 19F) are plotted in **Figure 2.6**. For 1CzTrz-F the 19F signal is split despite the symmetry in the molecular structure. This shows that there is a preferred local molecular packing arrangement that breaks the molecular symmetry of the two 19F sites in the molecule. In a random or fully amorphous arrangement, there should also be molecules where the molecular symmetry is preserved, and then only a single very broad peak should be seen. Similar as for 1CzTrz also in the 19F MAS NMR spectrum of the 3CzTrz-F compounds, two signals are observed, again pointing to a difference in the local chemical environment between the two 19F sites.

2.3.5 Density of states (DOS) simulation of crystal

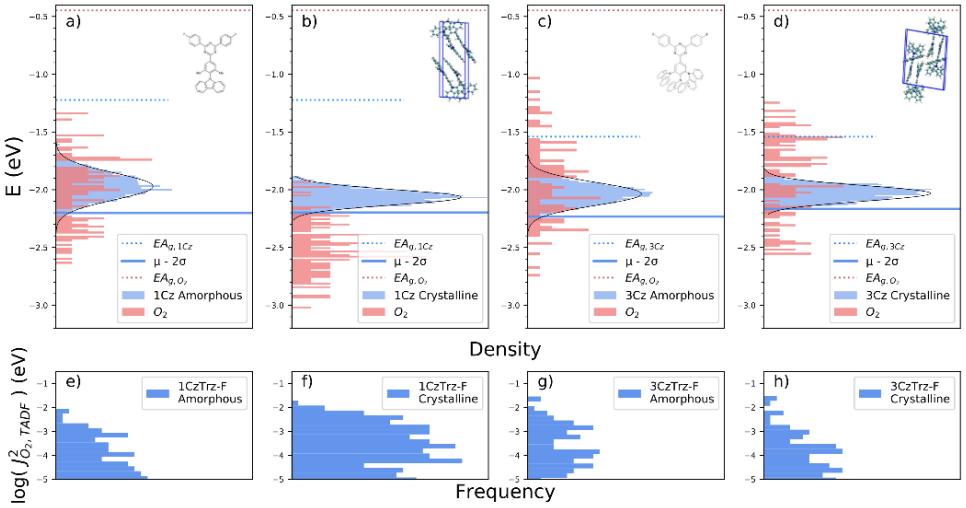

Figure 2.7: Calculated density-of-states distributions. The density of states of electron affinity of (a) amorphous 1CzTrz-F, (b) crystalline 1CzTrz-F, (c) amorphous 3CzTrz-F, and (d) crystalline 3CzTrz-F. e,f,g,h, Magnitude of electronic transfer integral vs. occurrence frequency in (e) amorphous 1CzTrz-F, (f) crystalline 1CzTrz-F, (g) amorphous 3CzTrz-F, and (h) crystalline 3CzTrz-F, respectively. The dotted lines are the gas-phases electron affinity for molecular oxygen and organic materials. The blue solid line represents the energy μ_e -2σ_e, with μ_e corresponding to the average of the calculated solid-state EA values and σ_e the standard deviation of the Gaussian distribution, respectively (Table 2.6). The energy μ_e -2σ_e is expected to correspond to the onset of the solid-state EA from UPS measurements[1]. Reproduced from reference [1].

Having established that there is a local ordering in the films, it is evident that the theoretical interpretation based on the amorphous phase of 1–3CzTrz-F should be handled with care, as the impact of molecular packing is not captured by these simulations. For this purpose, we also simulated the DOS of the crystalline phases using the structural data obtained from XRD for 1CzTrz-F and 3CzTrz-F. As shown in **Figure 2.7**, the EA distributions of oxygen are quite similar in crystalline and amorphous for 3CzTrz-F. In contrast, for 1CzTrz-F the oxygen EAs are much higher in the crystalline phase than in the amorphous phase, implying deeper traps. The energetic shift of the EA distribution in the crystalline state (**Table 2.6**) is largely attributed to a change in the electrostatic contribution to the EA, as seen in **Figure 2.8** and **Figure 2.9**. Considering the fact that there are regions in organic thin films with molecular packing resembling the crystalline state, the deep O_2 traps (**Table 2.7**) in crystalline 1CzTrz-F result in a higher overall trap density compared with 3CzTrz-F, which agrees with the trend of trap densities obtained from the drift-diffusion model.

Table 2.6 Material properties in crystalline phase of 1CzTRz-F and 3CzTrz-F[1].

	1CzTrz-F	3CzTrz-F
μ_e (eV)	-2.065	-2.031
σ_e (eV)	0.066	0.067
EA (eV)	-2.197	-2.166
μ_h (eV)	-6.028	-5.913
σ_h (eV)	0.099	0.083
IE (eV)	-5.831	-5.746

Table 2.7 Oxygen trap levels in crystalline phase of 1CzTrz-F and 3CzTrz-F[1].

	1CzTrz-F	3CzTrz-F
μ_e (eV)	-2.503	-1.900
σ_e (eV)	0.227	0.346
EA (eV)	-2.958	-2.593

However, as shown in **Figure 2.7** c-d, energetic considerations alone cannot account for the trap-free transport observed in 3CzTrz-F. This clearly suggests that the molecular packing is also an essential ingredient to obtain a trap-free current due to shielding of the electron transporting core from impurities by the stacking geometry. To further elucidate the effectiveness of the O_2 traps in the 1CzTrz-F and 3CzTrz compounds, we have evaluated the electronic transfer integrals representing the coupling between close-lying oxygen and CzTrz-F pairs (**Figure 2.7** e–h). It is shown that the total coupling strength, represented by the area under the histogram, is largest in the 1CzTrz-F crystalline phase, thereby stabilizing the oxygen and resulting in oxygen becoming a deeper and more effective trap in the crystalline 1CzTrz-F.

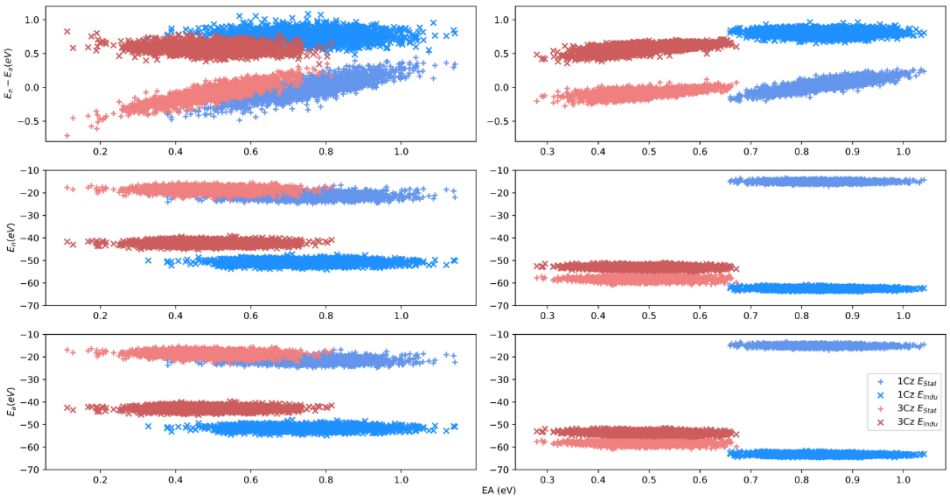

Figure 2.8: Static and inductive electronic energy contributions to site energies of 1CzTrz-F and 3CzTrz-F in amorphous, 1st column and crystalline phases, 2nd column[1]. Reproduced from reference [1].

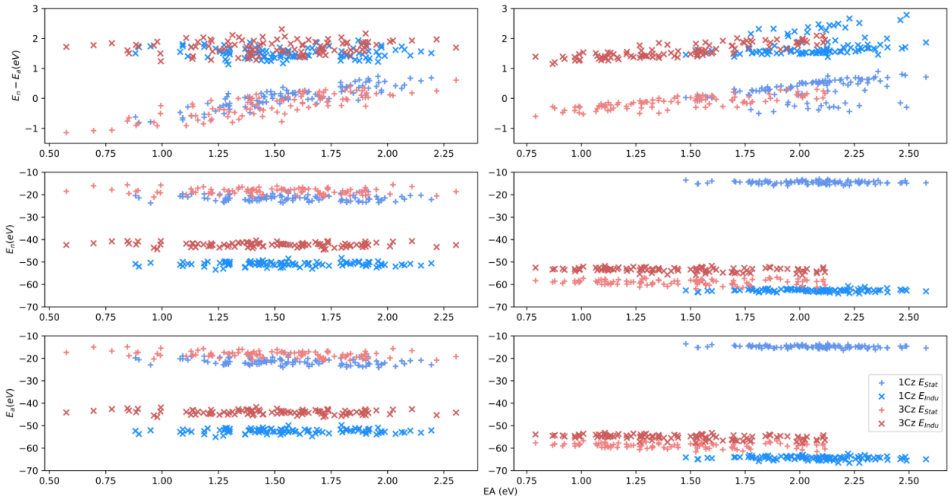

Figure 2.9: Static and inductive electronic energy contributions to site energies of interstitial oxygen in amorphous, 1st column, and crystalline, 2nd column, 1CzTrz-F and 3CzTrz-F[1]. Reproduced from reference [1].

2.4 Results and discussion on DTPT blue emitters

2.4.1 Charge transport study

To demonstrate the generality of our approach, we have applied the same strategy for obtaining trap-free transport in large energy gap organic semiconductors to a second series of blue-emitting materials, consisting of a triazine acceptor with two carbazole units with (out) fluorine constituents, DTPT-DCz, DTPT-DFCz and DTPT-D2FCz (**Figure 2.1**). It is expected that the addition of electronegative fluorine moieties will enhance both the ionization energy and EA of the molecules. This is indeed observed experimentally from cyclic-voltammetry measurements (**Table 2.1**), where the EA is enhanced from 2.6 eV (DTPT-DCz, no fluorine) to 2.8 eV (DTPT-D2FCz, 4 fluorine).

For similar oxygen levels, the strongest electron trapping is therefore expected for the non-fluorinated DTPT-DCz compound. However, experimentally, the opposite behavior is observed, as shown in **Figure 2.10**. DTPT-DCz shows nearly trap-free transport, whereas with increasing number of fluorine constituents the electron current is strongly reduced. The reduced current of the fluorinated compounds is well described by drift-diffusion simulations combining Ohmic contacts and trapping; the resulting transport and trapping parameters are given in **Table 2.8**.

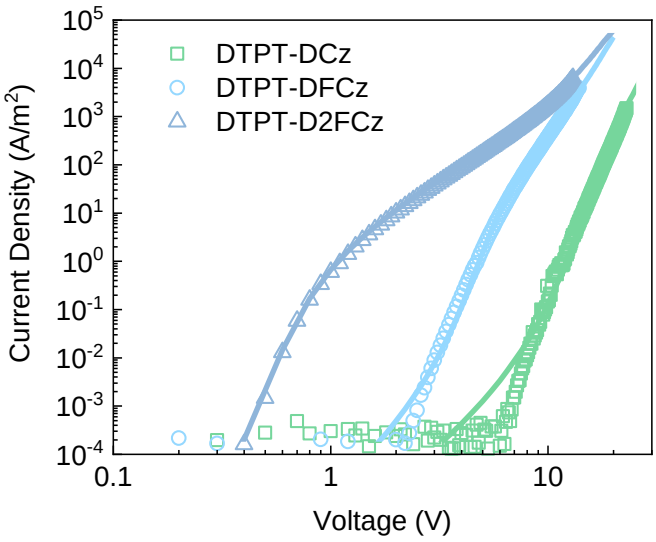

Figure 2.10: Electron current of DTPT-DFCz based compounds. Experimental (symbols) and simulated (lines) current density (J)-voltage (V) characteristics of DTPT-DCz (106 nm), DTPT-DFCz (95 nm) and DTPT-D2FCz (99 nm)[1]. Reproduced from reference [1].

Table 2.8 Drift-diffusion modeling parameters for electron-only devices of DTPT-DCz, DTPT-DFCz and DTPT-D2FCz[1].

	DTPT-DCz	DTPT-DFCz	DTPT-D2FCz
Trap density, N_t gauss ($\times 10^{22}$ m^{-3})	1.5	23	65
Trap depth, E_t (eV)	0.74	0.80	0.70
Width of Gaussian trap distribution, σ_t (eV)	0.12	0.139	0.12
Lattice constant EGDM, a ($\times 10^{-9}$ m)	1.3	1.4	1.1
DOS variance EGDM, σ (eV)	0.12	0.139	0.12
Mobility at 295 K, μ ($\times 10^{-11}$ m²/Vs)	3	0.63	1.5

2.4.2 Density of states (DOS) simulation

To obtain further insight, we simulated the DOS of both the amorphous and crystalline phases of these three compounds, shown in **Figure 2.11**. According to the amorphous phase simulations, similar trapping behaviour would be expected for all compounds, clearly in disagreement with the experiment. Similar to the 1CzTrz-F compound, the EA distribution of oxygen is considerably lowered in the crystalline phase of DTPT-D2FCz, leading to enhanced trapping. Thus, also for this compound the enhanced trapping in the crystalline phase is a result of a change in the energetics. However, similar to the 3CzTrz-F case, the occurrence of a trap-free current in DTPT-DCz cannot be explained by the simulations. In both the amorphous and crystalline phase severe trapping is predicted. This again strongly suggests that another packing-related mechanism plays an important role.

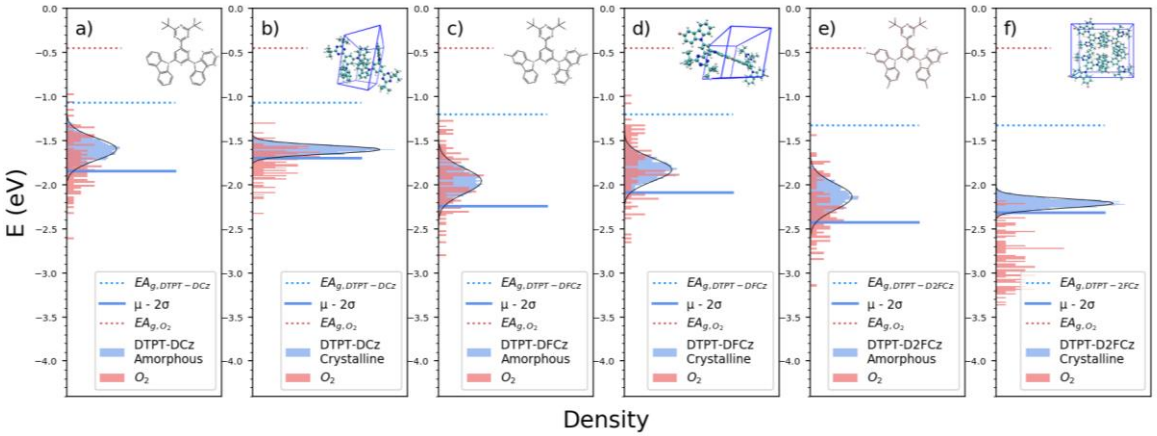

Figure 2.11: Calculated density-of-states distributions. The density of states of electron affinity of (a) amorphous DTPT-DCz, (b) crystalline DTPT-DCz, (c) amorphous DTPT-DFCz, (d) crystalline DTPT-DFCz, (e) amorphous DTPT-D2FCz and (f) crystalline DTPT-D2FCz, respectively[1]. Reproduced from reference [1].

2.4.3 Molecular ordering by XRD

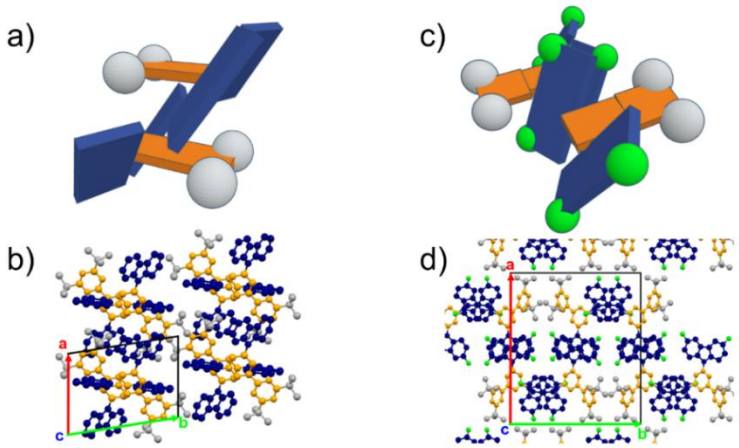

Figure 2.12: Molecular structures obtained from XRD. Crystal structures of the DTPT-DCz (a, b) and DTPT-D2FCz (c, d) compounds, determined by XRD. For a better visualization of the molecular packing, the two dimers of both crystallographic unit cells are draws schematically in a) and c). In b) and d), the triazine acceptor and the carbazole donor units are colored according to the schematic drawing a) and c) to illustrate the spatial arrangement of the acceptor-donor contacts in the 3-dimensional crystal structure. The white features indicate the tert-butyl groups, whereas the green features in d) indicate the fluorine atoms[1]. Reproduced from reference [1].

For this purpose, we have investigated the crystal structure using XRD on crystals of the tetrafluorinated DTPT-D2FCz and the non-fluorinated DTPT-DCz. In the latter sample, shown in **Figure 2.12**, the Cz substituents are arranged edge-on with a tilting angle of ~40° on top of the triazine ring. This arrangement together with the tert-butyl-groups protects the Trz rings from contact with small molecules such as O_2 or H_2O. Both the phenyl substituted triazine ring and the carbazole substituents show an in-plane arrangement with the same molecular building blocks of neighboring molecules (Cz

in-plane with Cz, Trz in-plane with Trz). Moreover, the phenyl ring and the triazine ring are in-plane, indicating an electronic conjugation between these moieties. In contrast, in the tetra-fluorinated DTPT-D2FCz the phenyl ring and the triazine ring are no longer in plane but show a relative tilt of more than 10°. Here the molecular ordering is clearly driven by pairwise π-stacking of the fluorinated carbazole substituents. In this crystal structure the triazine rings are completely unprotected against contact with small electron-trapping molecules such as O_2 or H_2O. This again shows that a 'closed' stacking geometry is a prerequisite to obtain trap-free transport by shielding the electron transporting core from extrinsic contaminants.

2.5 Experiment

Materials. 1CzTrz-F – 3CzTrz-F were synthesized by Oskar Sachnik under supervision of Dr. Jasper J. Michels, DTPT series were synthesized by Dehai Dou under supervision of Dr. Martin Baumgarten, according to procedures in literature and purified by vacuum sublimation. 1,3,5-Tris(1-phenyl-1*H*benzimidazol-2-yl)benzene (TPBi) was purchased from Luminescence Technology Corporation. Chemicals for synthetic operations were purchased from common suppliers (Sigma-Aldrich, Fisher Scientific, VWR etc.) and were used as received.

Device fabrication and measurements. Electron-only devices were fabricated on glass substrates by Xiao Tan and Oskar Sachnik under supervision of Dr. Gert-Jan A. H. Wetzelaer. The substrates were cleaned with detergent solution and were ultrasonicated in acetone and isopropyl alcohol. The substrates were heated at 140 °C for 10 min and subsequently treated with UV-ozone for 20 min. The substrates were transferred into a nitrogen-filled glove box and 30 nm of Al was thermally evaporated, followed by the organic layer (~100 nm) and a 4 nm TPBi layer. For completion a 5 nm Ba and 100 nm Al layer was evaporated on top. Electrical characterization was carried out under a N_2 atmosphere with a Keithley 2400 source meter.

Solution NMR measurements. All solution NMR spectra (^{1}H, $^{13}C\{H\}$) were measured by Constantin Haese under supervision of Dr. Robert Graf using a Bruker Avance III setup at 700.25 MHz ^{1}H Larmor frequency and were performed at 298 K with deuterated tetrachloroethane if not differently specified. Chemical shift values δ are given in ppm und coupling constants J are given in Hz. The multiplicity of signals is described using following shortcuts: s (singlet), d (doublet), dd (doublet of doublets), t (triplet), q (quartet), m (multiplet).

Solid state NMR measurements. All solid state NMR spectra were measured by Constantin Haese under supervision of Dr. Robert Graf. The solid samples were packed into Bruker BioSpin zirconia rotors with 1.3 mm outer diameter. ^{1}H MAS NMR spectra were acquired with 4 scans of direct excitation using a 2.0 µs 90 degree excitation pulse and a recycle delay of 30 s on a Bruker Avance NEO spectrometer operating at 850.27 MHz ^{1}H Larmor frequency at a MAS spinning speed of 50 kHz. ^{19}F MAS NMR spectra were acquired with 16 scans of direct excitation using a 2.5 µs 90 degree excitation pulse and a recycle delay of 30 s on a Bruker Avance III spectrometer at 470.61 MHz ^{19}F Larmor frequency and 25 kHz MAS spinning frequency.

Photoelectron Spectroscopy. Ionization energies were measured by Oskar Sachnik with an atmospheric photoemission yield spectrometer (AC-2) from Riken Keiki Co., Ltd.

Cyclic Voltammetry. Cyclic Voltammetry (CV) was carried out by Oskar Sachnik on a computer-controlled GSTAT12 in a three-electrode cell in anhydrous acetonitrile solution of *n*-Bu4NPF6 (0.05 M) with a scan rate of 100 mV/s at room temperature under argon. Pt wires were used as the counter and working electrodes, a silver wire applied was as reference electrode.

Theory calculation. All the DOS simulation for amorphous and crystal are done by Naomi Kinaret and Kun-Han Lin under supervision of Dr. Denis in the Theory Department of MPIP.

2.6 Conclusion

Due to stack integrity issues, printed blue OLEDs consist preferably of only one or two solution-processed layers. However, the absence of simultaneous trap-free transport of both electrons and holes in large band gap organic semiconductors so far has prevented the realization of efficient single-layer blue OLEDs (3 eV band gap), as trapping has a strong negative effect on their efficiency. The approach presented here shows that by manipulating the molecular structure of donor– acceptor molecules the trapping by defects can be prevented. As a result, this work paves the way towards efficient printed blue OLEDs in future.

Reference

1. Sachnik, O. *et al.* Elimination of charge-carrier trapping by molecular design. *Nat. Mater.* **22**, 1114–1120 (2023).
2. Bässler, H. Charge Transport in Disordered Organic Photoconductors a Monte Carlo Simulation Study. *Phys. status solidi* **175**, 15–56 (1993).
3. Brédas, J. L., Calbert, J. P., da Silva Filho, D. A. & Cornil, J. Organic semiconductors: A theoretical characterization of the basic parameters governing charge transport. *Proc. Natl. Acad. Sci.* **99**, 5804–5809 (2002).
4. Schweicher, G. *et al.* Molecular Semiconductors for Logic Operations: Dead-End or Bright Future? *Adv. Mater.* **32**, (2020).
5. Nicolai, H. T. *et al.* Unification of trap-limited electron transport in semiconducting polymers. *Nat. Mater.* **11**, 882–887 (2012).
6. Haneef, H. F., Zeidell, A. M. & Jurchescu, O. D. Charge carrier traps in organic semiconductors: a review on the underlying physics and impact on electronic devices. *J. Mater. Chem. C* **8**, 759–787 (2020).
7. Kotadiya, N. B., Mondal, A., Blom, P. W. M., Andrienko, D. & Wetzelaer, G.-J. A. H. A window to trap-free charge transport in organic semiconducting thin films. *Nat. Mater.* **18**, 1182–1186 (2019).
8. Zhuo, J. *et al.* Direct Spectroscopic Evidence for a Photodoping Mechanism in Polythiophene and Poly(bithiophene- alt -thienothiophene) Organic Semiconductor Thin Films Involving Oxygen and Sorbed Moisture. *Adv. Mater.* **21**, 4747–4752 (2009).
9. Nikolka, M. *et al.* High-mobility, trap-free charge transport in conjugated polymer diodes. *Nat. Commun.* **10**, 2122 (2019).
10. Zuo, G., Linares, M., Upreti, T. & Kemerink, M. General rule for the energy of water-induced traps in organic semiconductors. *Nat. Mater.* **18**, 588–593 (2019).
11. Van der Zee, B., Li, Y., Wetzelaer, G. A. H. & Blom, P. W. M. Efficiency of Polymer Light-Emitting Diodes: A Perspective. *Adv. Mater.* **34**, (2022).
12. Kotadiya, N. B., Blom, P. W. M. & Wetzelaer, G.-J. A. H. Efficient and stable single-layer organic light-emitting diodes based on thermally activated delayed fluorescence. *Nat. Photonics* **13**, 765–769 (2019).
13. Abbaszadeh, D. *et al.* Elimination of charge carrier trapping in diluted semiconductors. *Nat. Mater.* **15**, 628–633 (2016).
14. Sachnik, O. *et al.* Single-Layer Blue Organic Light-Emitting Diodes With Near-Unity Internal Quantum Efficiency. *Adv. Mater.* **35**, (2023).
15. Cui, L., Kim, J. U., Nomura, H., Nakanotani, H. & Adachi, C. Benzimidazobenzothiazole-Based Bipolar Hosts to Harvest Nearly All of the Excitons from Blue Delayed Fluorescence and Phosphorescent Organic Light-Emitting Diodes. *Angew. Chemie* **128**, 6978–6982 (2016).
16. Niu, Q., Rohloff, R., Wetzelaer, G.-J. A. H., Blom, P. W. M. & Crăciun, N. I. Hole trap formation in polymer light-emitting diodes under current stress. *Nat. Mater.* **17**, 557–562 (2018).

17. Chen, Y. *et al.* n-Doping-induced efficient electron-injection for high efficiency inverted organic light-emitting diodes based on thermally activated delayed fluorescence emitter. *J. Mater. Chem. C* **5**, 8400–8407 (2017).

18. Chen, H.-F. *et al.* 1,3,5-Triazine derivatives as new electron transport–type host materials for highly efficient green phosphorescent OLEDs. *J. Mater. Chem.* **19**, 8112 (2009).

19. Lee, D. R. *et al.* Design Strategy for 25% External Quantum Efficiency in Green and Blue Thermally Activated Delayed Fluorescent Devices. *Adv. Mater.* **27**, 5861–5867 (2015).

20. Koster, L. J. A., Smits, E. C. P., Mihailetchi, V. D. & Blom, P. W. M. Device model for the operation of polymer/fullerene bulk heterojunction solar cells. *Phys. Rev. B* **72**, 085205 (2005).

21. Kotadiya, N. B. *et al.* Universal strategy for Ohmic hole injection into organic semiconductors with high ionization energies. *Nat. Mater.* **17**, 329–334 (2018).

22. Noriega, R. *et al.* A general relationship between disorder, aggregation and charge transport in conjugated polymers. *Nat. Mater.* **12**, 1038–1044 (2013).

23. Han, G., Guo, Y., Song, X., Wang, Y. & Yi, Y. Terminal π–π stacking determines three-dimensional molecular packing and isotropic charge transport in an A–π–A electron acceptor for non-fullerene organic solar cells. *J. Mater. Chem. C* **5**, 4852–4857 (2017).

24. Seifrid, M., Reddy, G. N. M., Chmelka, B. F. & Bazan, G. C. Insight into the structures and dynamics of organic semiconductors through solid-state NMR spectroscopy. *Nat. Rev. Mater.* **5**, 910–930 (2020).

25. DeLongchamp, D. M., Kline, R. J., Fischer, D. A., Richter, L. J. & Toney, M. F. Molecular Characterization of Organic Electronic Films. *Adv. Mater.* **23**, 319–337 (2011).

26. Harris, R. K. & Jackson, P. High-resolution fluorine-19 magnetic resonance of solids. *Chem. Rev.* **91**, 1427–1440 (1991).

27. Etherington, M. K. *et al.* Persistent Dimer Emission in Thermally Activated Delayed Fluorescence Materials. *J. Phys. Chem. C* **123**, 11109–11117 (2019).

3. Inverted device architecture for high efficiency single-layer OLEDs with imbalanced charge transport

In this chapter, we have investigated the inverted single-layer OLEDs performance with a wide color range of organic emitters. Generally, wide-gap organic semiconductors exhibiting imbalanced electron and hole transport, therefore efficient organic light-emitting diodes require a multilayer architecture of electron- and hole-transport materials to confine charge recombination to the emissive layer. Here, it is proven that it is possible to obtain highly efficient single-layer OLEDs, without the need for additional charge-transport and blocking layers, even for emitters with imbalanced charge transport. For hole-dominated emitters, an inverted single-layer device architecture with ohmic bottom-electron and top-hole contacts moves the emission zone away from the metal top electrode, thereby more than doubling the optical outcoupling efficiency. Finally, a blue-emitting inverted single-layer OLED based on thermally activated delayed fluorescence is achieved, exhibiting a high external quantum efficiency of 19% with little roll-off at high brightness, demonstrating that balanced charge transport is not a prerequisite for highly efficient single-layer OLEDs[1].

This chapter was 2024 published as “Inverted device architecture for high efficiency single-layer organic light-emitting diodes with imbalanced charge transport” in Nature Communications, Volume 15, 2024 May, page 4107 together Xiao Tan, Dehai Dou, Lay-Lay Chua, Rui-Qi Png, Daniel G. Congrave, Hugo Bronstein, Martin Baumgarten, Yungui Li, Paul W. M. Blom & Gert-Jan A. H. Wetzelaer.

Author Contributions

G.-J.A.H.W. proposed the project. G.-J.A.H.W. and X.T. designed the experiments. X.T. carried out the experiments, simulations and wrote the manuscript. Y.L. performed the optical simulations. D.D. and D.G.C. synthesized the compound 2tCz2CzBN, H.B. and M.B. supervised the synthetic work, L.C. and R.P. synthesized the compound n-doped TFB, G.-J.A.H.W. and P.W.M.B. supervised the project.

3.1 Introduction

Most organic semiconductors exhibit highly imbalanced charge transport with differences between the electron and hole transport up to several orders of magnitude. Recently, we found that charge transport is closely related to the energy levels of the organic semiconductor with respect to a trap-free energy window spanning approximately 2.4 eV[2]. As opposed to narrow-gap organic semiconductors as used in efficient organic photovoltaics, mostly obeying to this energy window, the wide-gap materials needed for OLEDs rarely fit within this energy window. An immediate consequence is that charge transport in OLED emitters is often imbalanced due to charge trapping, especially in blue emitters having a wide energy gap of close to 3 eV. From an energy-level perspective, most known TADF emitters have their ionization energy inside the trap-free window (< 6.0 eV), whereas the electron affinity is outside. As a result, charge transport in most current emitters is expected to be hole dominated, with electron transport being limited by charge trapping. Using the known (hole-dominated) emitters in a single-layer OLED would therefore often result in a recombination zone close to the metallic cathode, which leads to direct quenching of excitons, as well as coupling of photons to SPP modes[3]. Consequently, light extraction would be highly suppressed[4]. This would imply that for most TADF emitters a high efficiency in a single-layer architecture is not possible.

A potential solution to shift the recombination zone away from the metallic top electrode in a single-layer OLED is to invert the device structure. In this case, the faster holes are injected into the emitter from the top metallic electrode, while the slower electrons are injected from the bottom transparent electrode[5]. However, it is still unclear if this is a viable solution or if imbalance charge-transport excludes efficient single-layer OLEDs fundamentally. For a single-layer OLED, efficient charge injection via ohmic contacts is a crucial prerequisite, since blocking layers are absent[6]. For an inverted OLED, a low work function transparent bottom electrode is thus required[7]. Several attractive options for such bottom electrodes have been published, among which a ZnO electrode with a thin polyethyleneimine layer to reduce the work function down to 3.1 eV[8]. Although such an injection structure has been applied successfully in combination with a low-LUMO emitter, it is unclear if the work function is low enough to achieve an ohmic electron contact to emitters with a high LUMO[9,10]. Another possibility to achieve electron injection in an inverted OLED is the use of n-type dopants, but the options for dopants with a sufficiently low IE are limited[11]. Recently, a family of self-compensated n-doped polymers was developed with effective work functions as low as 2.4 eV, based on solution-casting of air-stable materials followed by *in-device* activation on the n-doped state[12]. These n-doped polymers have been successfully applied in conventional OLED structures with electron injection from the top electrode. Recently, bottom electron-injecting blue inverted multilayer quantum-dot LEDs have been demonstrated with such n-doped polymers, in which charge confinement is achieved with additional blocking layers[13]. However, it is still unclear if these n-doped polymers can also be successfully applied in inverted OLEDs in the single-layer architecture without change transport or confinement layers.

3.2 Device concept

Here, we demonstrate that highly efficient single-layer OLEDs can be realized, despite imbalanced charge transport of the emitter. For hole-dominated emitters, this is accomplished in an inverted OLED architecture, where efficient electron injection from the transparent bottom electrode is achieved with an n-doped polymer layer. By inverting the device structure, the charge-recombination zone is moved away from the metal top electrode, eliminating severe light loss due to the coupling of photons to SPP modes. Based on this concept, blue inverted single-layer OLEDs with an EQE of up to 19% are demonstrated, using an emitter with imbalanced transport and in the complete absence of high-triplet-energy host or blocking layers.

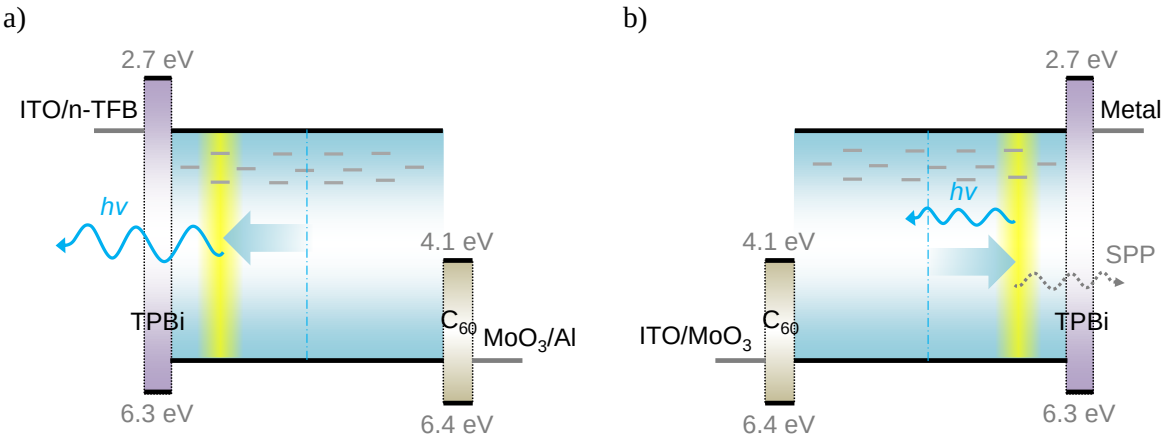

Figure 3.1: Device design principle. a) Schematic energy band diagram of the inverted single-layer OLED. Photon losses to SPP modes are indicated in b) for the conventional structure[1]. Reproduced from reference [1]

In **Figure 3.1**, the device layout of our inverted single-layer OLED is shown. The emissive layer is sandwiched between a MoO_3/Al top anode and an ITO/TFB bottom cathode, using a thin C60 and TPBi interlayer for the formation of an ohmic hole and electron contact, respectively. The diagrams schematically show the presence of electron traps, which slow down electron transport. As a result, the emission zone (yellow) shifts toward the electron-injecting contact.

For electron injection, the bottom electrode is coated with the n-doped polymer TFB[12] (Poly[(9,9-di-n-octylfluorene-2,7-diyl)-alt-(1,4-phenylene-(4-sec-butylphenylimino)-1,4-phenylene)]) by means of spin coating. Although TFB is often associated with hole transport, it can be n-doped *in-device* by oxalate electron transfer induced by hole sensitization in a self-compensated polymer to an ultralow effective of work function of 2.4 eV. The work function of these self-compensated polymers is set by the electronic structure of the polymer semiconductor backbone together with the local Coulomb (Madelung) potential effects of the ions, both counter-balancing and spectator[14,15]. For hole injection we use a layer of the high work function metal oxide MoO_3. To ensure ohmic charge injection, thin (3-4 nm) tunneling interlayers of TPBi and C_{60} are being used at the respective electrodes. These interlayers decouple the electrode and the organic semiconductor electrostatically, restoring the Fermi-level alignment[16]. It should be noted that while still multiple layers are being used, these are part of the charge-injection structure. These thin layers are transparent for charges[16] and are too thin to prevent energy transfer of excitons[17]. Charge-transport and blocking layers are absent, which in conventional multilayer OLEDs have to be tuned to the emitter in terms of energy levels and triplet energy. Here, charges are directly injected into the emitter and thus the balance in charge-transport properties of the emitter controls the position of the emission zone. This balance should not be confused with the "charge-balance factor" in multilayer OLEDs[18], which is a measure of the recombination yield of electrons and holes. In a single-layer OLED on the other hand, the high density of majority carriers near the ohmic contacts ensures that minority carriers cannot exit the device without recombining, resulting in negligible leakage of charges[19].

3.3 Results and discussion

3.3.1 Inverted OLED with CzDBA

To test the newly designed inverted device structure, we first selected the yellow TADF emitter CzDBA[20] for the emissive layer, as shown in **Figure 3.2 a)**. CzDBA has been successfully applied in a conventional single-layer OLED and has fairly balanced charge transport[21]. As such, it is excellently suited to assess the proper functioning of the charge-injection structure. The measured electroluminance soectrum, current density and luminance as a function of voltage and EQE are shown in **Figure 3.2 b-c)**. The EQE reaches a maximum of 15.5% as shown in **Figure 3.2 d)**, which is a decent value, but somewhat lower compared to the conventional OLED structure, which reaches an EQE of 19%[6]. The lower EQE can be explained by the electron transport being slightly superior to the hole transport in CzDBA, resulting in a recombination zone closer to the metallic top electrode in an inverted OLED, which slightly reduces optical outcoupling. To put the sensitivity to charge injection into perspective, a single-layer CzDBA OLED with a conventional non-ohmic LiF/Al cathode reaches an EQE of only 0.3%[6]. Therefore, the high EQE for the inverted device indicates that electron injection is efficient.

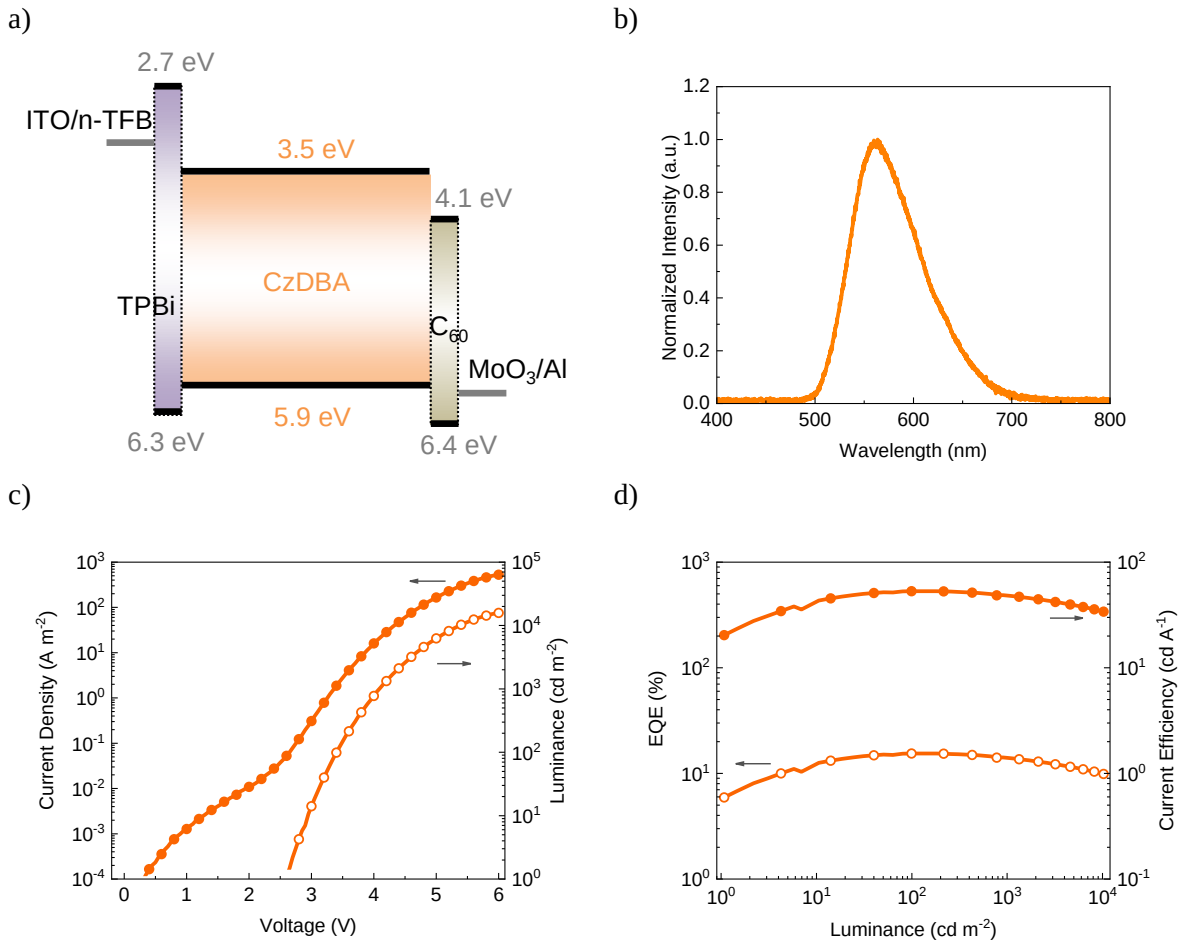

Figure 3.2: Device configuration and performance of a single-layer CzDBA inverted OLED. a) Device structure with energy diagram, b) electroluminescence spectrum, c) current density–voltage and luminance–voltage characteristic, d) corresponding EQE and current efficiency as a function of luminance[1]. Reproduced from reference [1].

3.3.2 Inverted OLED with DMAC-BP

With the successful fabrication of an inverted single-layer CzDBA OLED, the next step is to apply the inverted device structure to an emitter with a higher LUMO and imbalanced charge transport. To this end, we selected the green TADF emitter bis[4-(9,9-dimethyl-9,10-dihydroacridine)phenyl]methanone (DMAC-BP) with a HOMO energy level of -5.8 eV and LUMO energy level of -3.1 eV[22,23]. This emitter has been successfully used in a non-doped multilayer OLED, reaching a maximum EQE of 18.9%. However, in the same study, a single-layer DMAC-BP OLED achieved an EQE of only 0.06%, which is expected to be due to a combination of imbalanced charge transport and suboptimal charge injection. Since the charge-transport characteristics of DMAC-BP are unknown, we fabricated hole-only and electron-only devices with ohmic contacts. The measured current density-voltage characteristics are showed in **Figure 3.3 a-b)**.

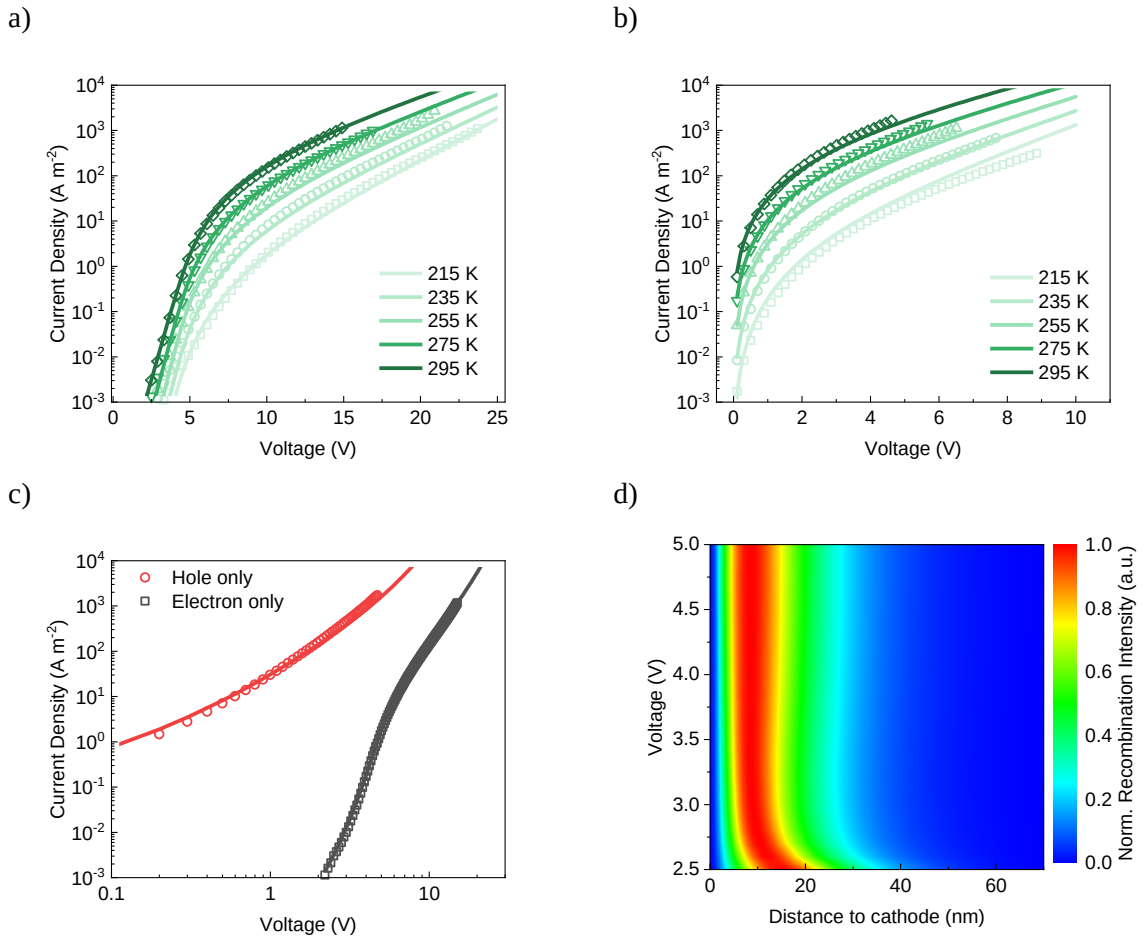

Figure 3.3: Current density–voltage characteristics of DMAC-BP a) electron- (110 nm) and b) hole-only (119 nm) devices (symbols) with temperature dependences, solid lines are fits with a numerical drift-diffusion model, c) JV comparison of HOD and EOD at 295 K, d) voltage-dependent recombination profile normalized to the total rate with 70 nm emissive layer[1]. Reproduced from reference [1].

The hole current is orders of magnitude higher than the electron current, indicating imbalanced charge transport. The charge-transport properties were quantified by fitting the hole and electron currents with numerical drift-diffusion simulations[24]. The electron and hole mobility amounted to 1 ×

10^{-7} cm^2 V^{-1} s^{-1} and 4×10^{-7} cm^2 V^{-1} s^{-1}, respectively. However, while hole transport is trap free, the electron transport is severely reduced due to the presence of electron traps with a density of 2×10^{23} m^{-3}, which can be seen from the steep voltage-dependence of the current, before reaching the trap-filled limit. The presence of electron traps, rather than the mobility of free electrons, results in an electron current that is orders of magnitude lower than the hole current (**Figure 3.3 c**). This is unlike the situation in emitters with balanced transport, such as CzDBA, where the electron and hole current are almost equal due to the near absence of charge traps. As a result of the highly imbalanced charge transport due to severe electron trapping in DMAC-BP, bimolecular recombination in a single-layer DMAC-BP OLED occurs close to the cathode interface, as shown by the drift-diffusion simulations of the recombination profile in **Figure 3.3 d)**. Therefore, it is expected that an inverted OLED architecture could be of benefit to the performance in case of DMAC-BP as the emitter.

Table 3.1: Drift-diffusion modeling parameters for single-carrier devices of DMAC-BP[1].

	DMAC-BP HOD	DMAC-BP EOD
Trap density, N_t gauss ($\times 10^{23}$ m^{-3})	\	1.6
Trap depth, E_t (eV)	\	0.8
Width of Gaussian trap distribution, σ_t (eV)	\	0.1
Lattice constant EGDM, a ($\times 10^{-9}$ m)	1.7	1.0
DOS variance EGDM, σ (eV)	0.144	0.14
Mobility at 295 K, μ ($\times 10^{-13}$ m^2/Vs)	428.9	95

Using a previously developed procedure, the optical outcoupling efficiency into air can be simulated based on the calculated recombination profile, together with the position-dependent optical-outcoupling efficiency at every recombination site[25]. The recombination profile is simulated based on the experimental charge-transport parameters, as outlined above in **Table 3.1**. The optical-outcoupling model includes the measured optical constants of all layers, and the orientation of emitting dipoles are measured by the angular dependence of photoluminescence (**Figure 3.4**), and the anisotropy factor is determined as 0.325 in terms of vertical dipoles.

a) b)

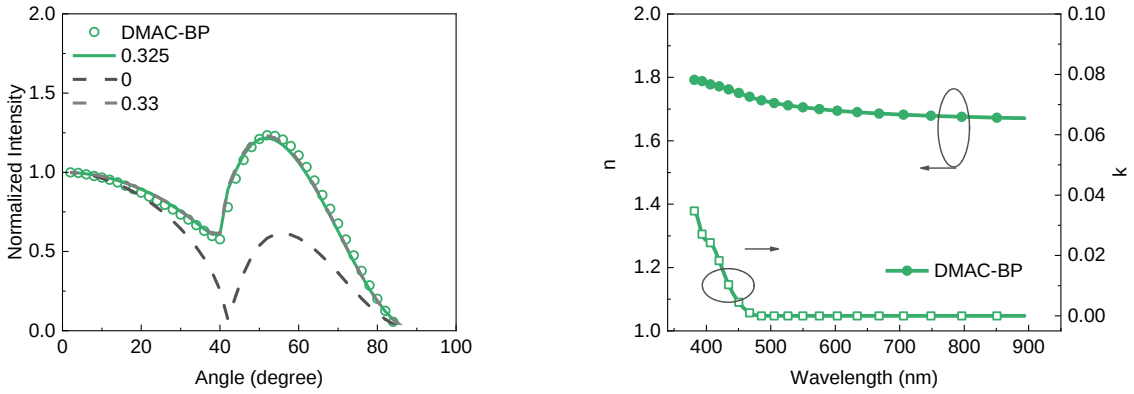

Figure 3.4: Optical characterization for DMAC-BP. a) Anisotropy factor determined from the angular-dependent photoluminescence, b) refractive index determined from the ellipsometry[1]. Reproduced from reference [1].

As a next step, DMAC-BP is applied in both conventional OLED and inverted OLED structures with an emissive layer thickness of 70 nm (**Figure 3.5**). The inverted OLED shows a maximum EQE of 15.9%, compared to 8.9% for the conventional OLED configuration, as shown in **Figure 3.6 a-b)**. The higher efficiency of the inverted device is a direct consequence of the superior hole transport, enhancing the optical outcoupling by shifting the recombination zone away from the metallic top electrode. Furthermore, the inverted OLED shows very little efficiency roll-off at high brightness. The higher efficiency roll-off for the conventional device structure is attributed to the emission zone moving closer to the metallic cathode at higher driving voltages. This effect is absent in the inverted OLED, as the bottom cathode is nonmetallic and therefore does not lead to coupling to SPP modes. It is noted that the EL spectrum of the inverted OLED is broadened by 7 nm **Figure 3.6 c)**, which we consider to be due to the different position of the emission zone with respect to the optical microcavity. Nevertheless, it is worth mentioning that the efficiency of the inverted single-layer OLEDs is not far off the efficiency of published multilayer DMAC-BP OLEDS[22].

a) b)

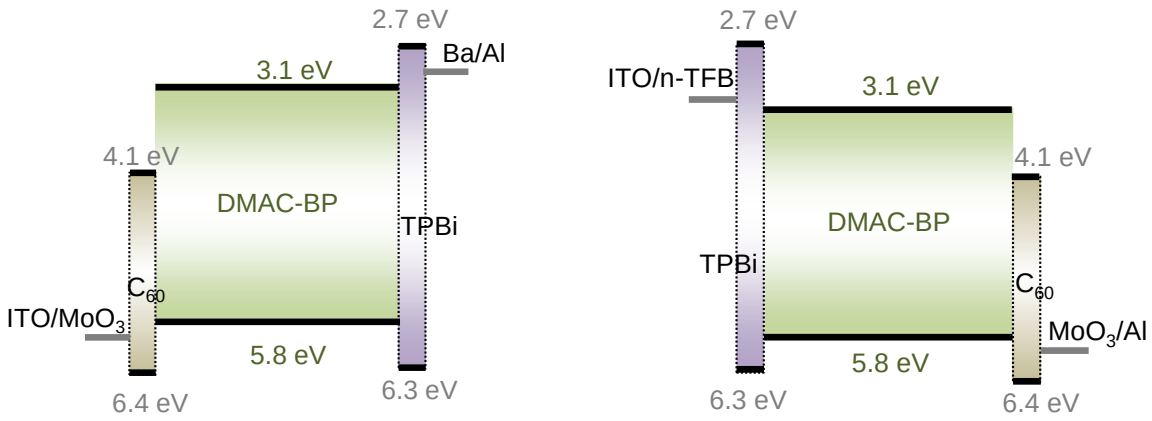

Figure 3.5: Device configuration of single-layer DMAC-BP OLEDs with energy diagram a) conventional and b) inverted OLEDs. Reproduced from reference [1].

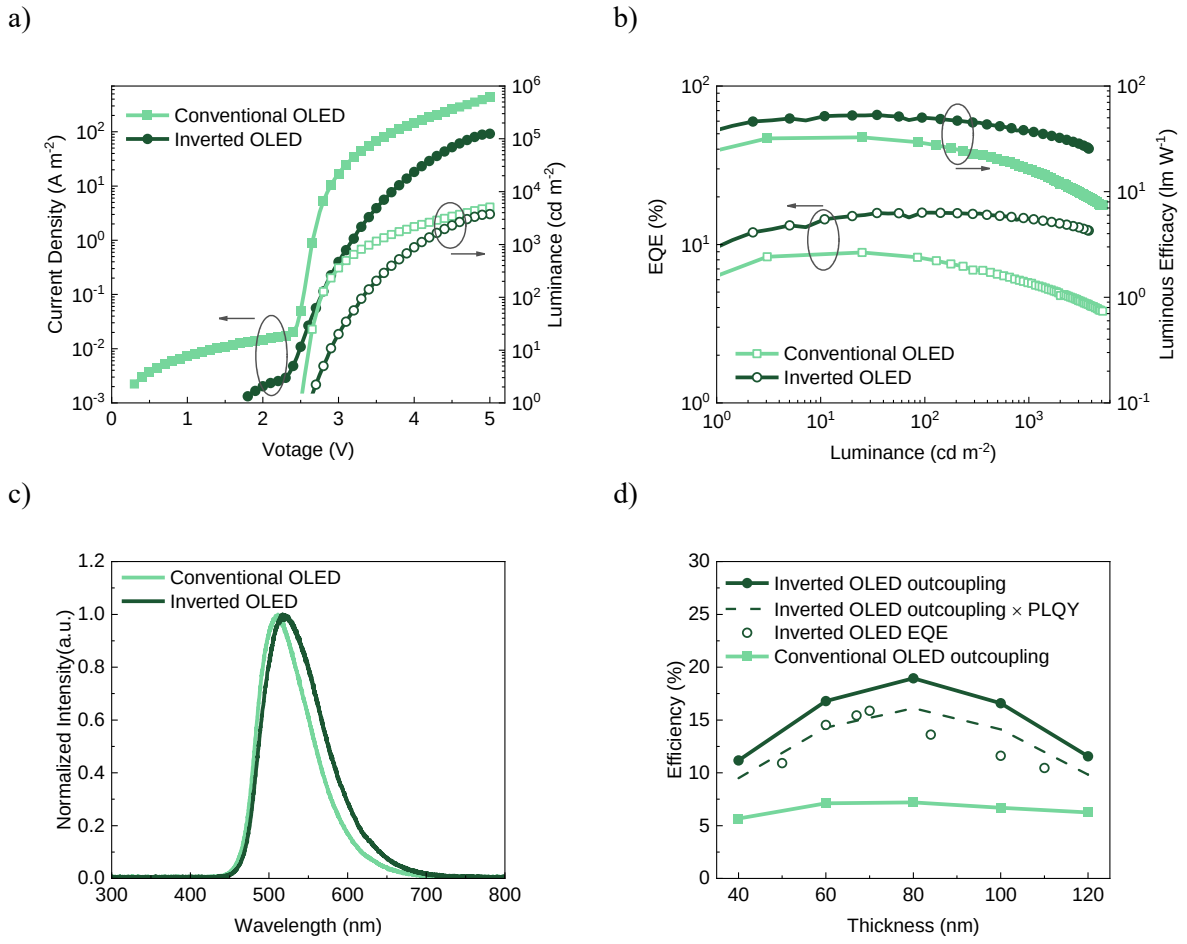

Figure 3.6: Device performance of single-layer DMAC-BP. a) current density–voltage and luminance–voltage characteristic, b) corresponding EQE and current efficiency as a function of luminance, c) electroluminescence spectra, d) emissive layer thickness-dependent outcoupling efficiency simulated at an applied voltage of 2.7 V and experimental EQE[1]. Reproduced from reference [1].

The improvement in EQE by inverting the device structure is also rationalized by optical outcoupling simulations. As shown in **Figure 3.6 d)**, the maximum outcoupling efficiency for an inverted DMAC-BP device equals 19%. The measured EQE of 15.9% therefore indicates a high IQE, when considering the PLQY of neat DMAC-BP of 85%[22].

Furthermore, the thickness dependence of the outcoupling efficiency is shown in **Figure 3.6 d)**. For single-layer OLEDs, changing the layer thickness modifies the optical cavity, while the recombination profile for any thickness can be simulated with the same set of charge transport parameters[25,26]. The experimental EQE with thickness dependence follows the same trend as the simulated optical outcoupling efficiency. It is also quantitatively well described when further considering the PLQY of the DMAC-BP neat film. The agreement in the thickness dependence confirms that the simulated recombination profile, based on the experimental transport parameters, is accurate. Qualitatively, one can understand the thickness dependence considering that a maximum in outcoupling is achieved when emission takes place at a specific distance from the metal, which is about 70 nm for a green emitter[27]. Since the optimal layer thickness is close to this value, the recombination zone must be close to the transparent cathode. The outcoupling efficiency for the conventional device is calculated to be only 7.2%, slightly lower than the experimental EQE. A possible explanation for this discrepancy

could be that the outcoupling model is highly sensitive to the exact position of the emission zone when it is in close vicinity to the metal interface[4]. In that case, a minor inaccuracy in the exact recombination profile may lead to a substantial difference in the simulated outcoupling efficiency for the conventional device architecture, where the recombination zone is very close to the cathode.

3.3.3 Inverted OLED with 2tCz2CzBN

The results of the green inverted DMAC-BP OLED demonstrate that efficient single-layer OLEDs are feasible even for emitters with highly imbalanced charge transport. Taking into account the energy-level considerations of the trap-free window, imbalanced charge transport appears to be a major problem especially with regard to blue emitters, having a wide energy gap of close to 3 eV. Therefore, as a next step, we investigate the feasibility of an inverted blue single-layer OLED, despite imbalanced charge transport. Here, we chose 2tCz2CzBN—a reported TADF blue emitter with a HOMO energy level of -6.0 eV showing promising performance (EQE_{max} of 21.6%) in an undoped multilayer OLED[28]. The reported LUMO energy of -3.1 eV is expected to be accessible for electron injection from n-TFB. It should be noted that direct evaluation of the electron-injection properties of n-TFB is not possible in an electron-only device, as hole sensitization is required for n-doping[12]. However, the built-in voltages of the inverted and conventional OLEDs are equal, implying that the n-TFB contact is close to ohmic. Using the same procedure as outlined previously for DMAC-BP, the charge transport properties of 2tCz2CzBN were obtained (**Figure 3.7**).

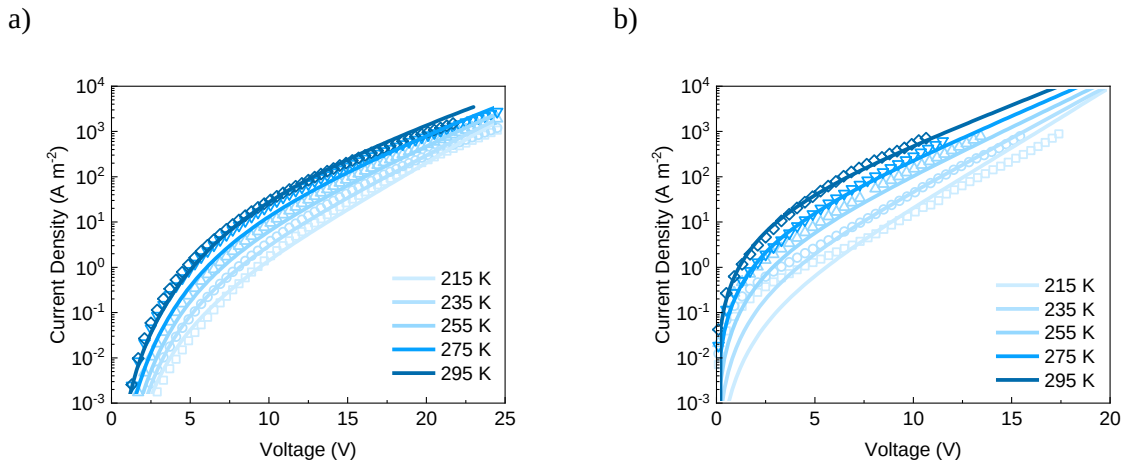

Figure 3.7: Current density–voltage characteristics of 2tCz2CzBN, a) electron- (97 nm) and b) hole-only (108 nm) devices (symbols) with temperature dependences, solid lines are fits with a numerical drift-diffusion model[1]. Reproduced from reference [1].

a) b)

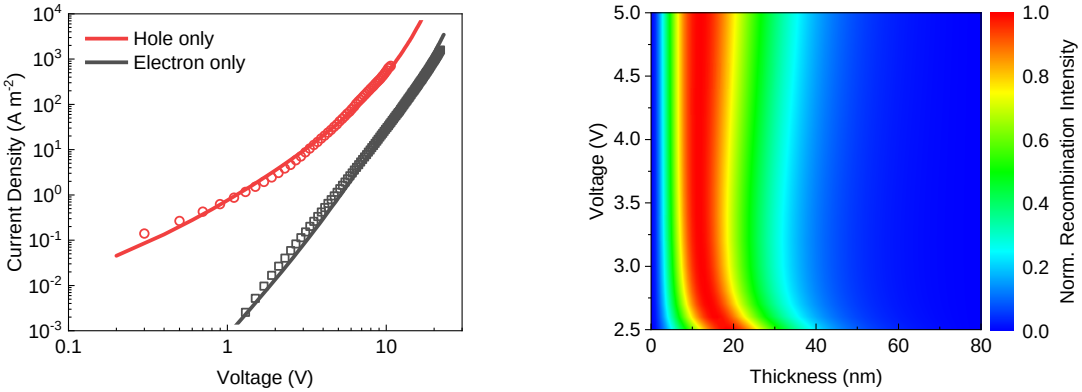

Figure 3.8: Current density–voltage characteristics of 2tCz2CzBN, a) JV comparison of of 2tCz2CzBN HOD and EOD at 295 K, b) voltage-dependent recombination profile normalized to the total rate with 80 nm emissive layer[1]. Reproduced from reference [1].

Also in this case, hole transport is clearly superior to electron transport, as observed from the substantial difference in electron and hole current (**Figure 3.8 a**). The extracted electron and hole mobility amounted to 2×10^{-9} cm^2 V^{-1} s^{-1} and 6×10^{-9} cm^2 V^{-1} s^{-1}, respectively.

Table 3.2: Drift-diffusion modeling parameters for single-carrier devices of 2tCz2CzBN[1].

	2tCz2CzBN HOD	2tCz2CzBN EOD
Trap density, N_t gauss ($\times 10^{23}$ m^{-3})	\	4
Trap depth, E_t (eV)	\	0.6
Width of Gaussian trap distribution, σ_t (eV)	\	0.1
Lattice constant EGDM, a ($\times 10^{-9}$ m)	1.4	1.0
DOS variance EGDM, σ (eV)	0.15	0.15
Mobility at 295 K, μ ($\times 10^{-13}$ m^2/Vs)	5.61	2

While hole transport is trap free, electron transport is limited by traps with a density of 4×10^{23} m^{-3}, giving rise to highly imbalanced transport. Similar to the case of DMAC-BP, the imbalance in charge transport is not so much caused by a difference in mobility, but by the presence of a considerable electron-trap density. These charge-transport parameters (**Table 3.2**) are subsequently used to simulate the voltage-dependent recombination profile numerically in a double carrier device, as shown in **Figure 3.8 b)**. The recombination zone is, as expected, close to the cathode. Furthermore, the recombination zone shifts closer to the cathode with increasing driving voltage, while slightly broadening due to spreading of the charge concentration.

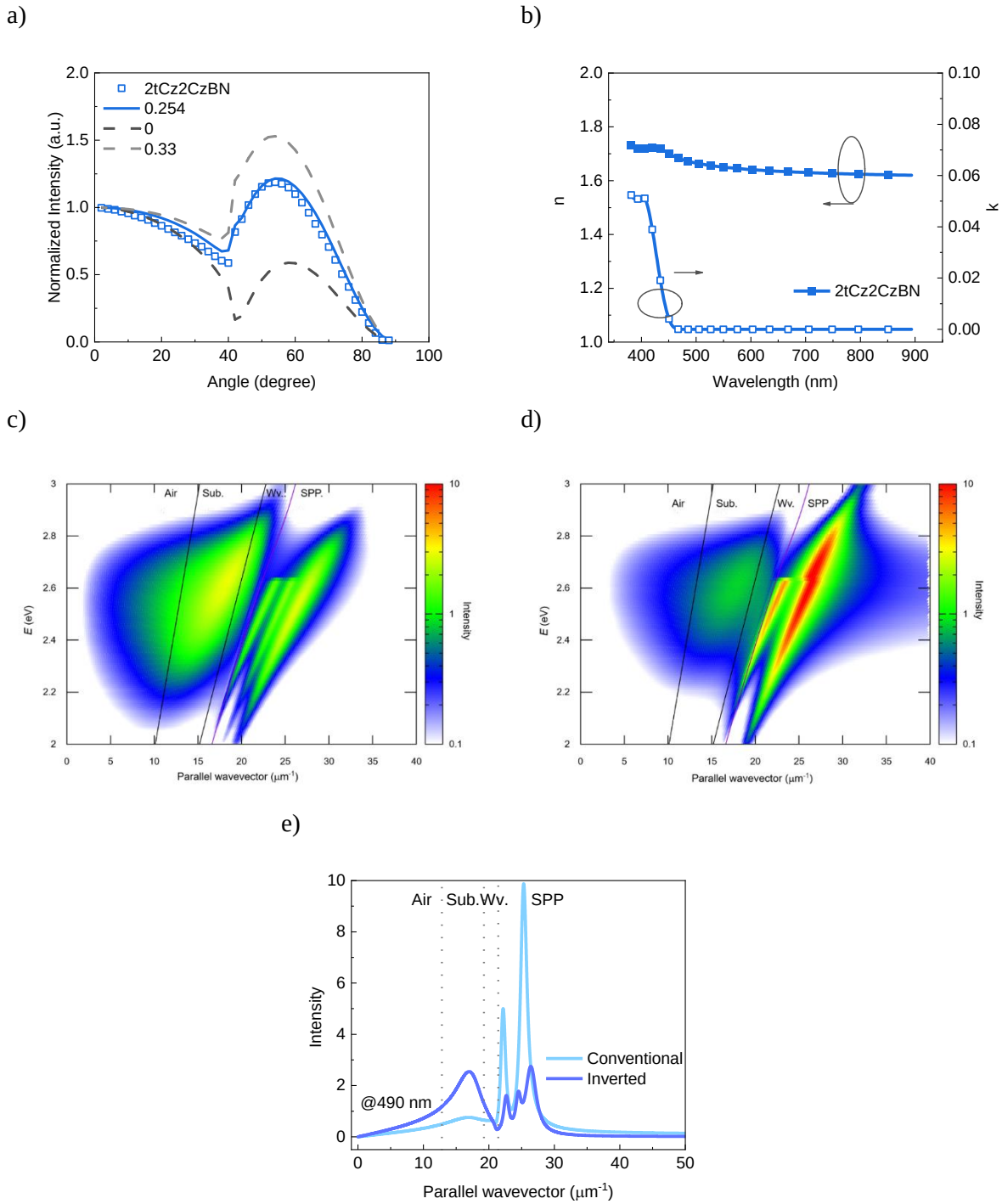

Figure 3.9: Optical characterization for 2tCz2CzBN. a) Anisotropy factor determined from the angular-dependent photoluminescence, b) refractive determined from the ellipsometry. Power dissipation for single-layer blue OLED with c) conventional device structure, d) inverted device structure. The air, substrate, waveguide, and SPP mode are indicated, e) the power dissipation for all wavelengths[1]. Reproduced from reference [1].

Based on the simulated recombination profile, the optical outcoupling efficiency is calculated for different emissive layer thicknesses. For the inverted OLED, a maximum outcoupling efficiency to air of 20% is determined for the optimal emissive layer thickness range of 60-80 nm. For the conventional OLED, an outcoupling efficiency of up to only 7% is simulated. The outcoupling efficiency is slightly

higher than for the DMAC-BP inverted OLED, which attributed to a higher fraction of horizontally oriented emitters, with a measured anisotropy factor of 0.254 in terms of vertical dipoles **Figure 3.9 a)** and **b)**.

As shown in **Figure 3.9 c-e)**, the optical power dissipated inside the inverted and conventional device structure at the peak wavelength, and the power dissipation for all wavelengths. These results demonstrate that the fraction of photons coupled to non-radiative SPP modes is drastically reduced in the inverted structure, where the emission zone is no longer in close vicinity to the metal top electrode. This is the main reason for the increased efficiency of the inverted single-layer OLEDs, exhibiting a much higher fraction of generated photons coupled into air.

Based on the optical simulations, inverted and conventional single-layer blue OLEDs based on 2tCz2CzBN were fabricated and the device performance is shown in **Figure 3.10**.

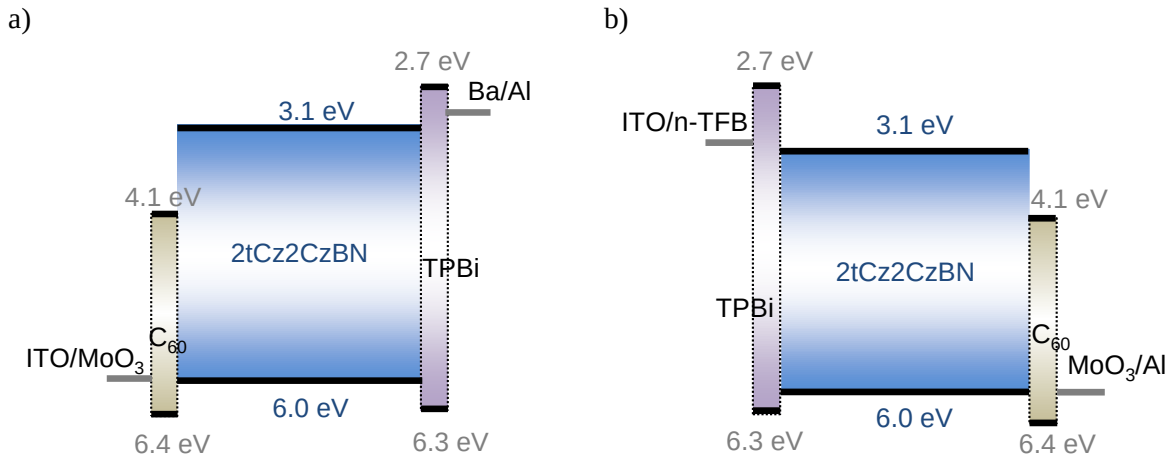

Figure 3.10: Device structure of single-layer 2tCz2CzBN OLEDs with energy diagram a) conventional and b) inverted OLEDs[1]. Reproduced from reference [1].

The inverted single-layer blue OLED shows an impressive EQE of 16.9%, which can even be increased to 18.7% when using an additional PEDOT:PSS layer to further tune the device optics underneath the TFB layer as shown in **Figure 3.11 a-b)**. The PEDOT:PSS layer does not influence the built-in voltage and thus does not compromise the electron injection. However, the device current is slightly lower, possibly due to the added resistance of the layer. The high EQE confirms the maintained electron injection, as even a small injection barrier would drastically compromise the efficiency[6]. This EQE approaches the maximum outcoupling efficiency and points to a very high internal quantum efficiency, considering the measured PLQY for a 2tCz2CzBN film of 86%. Furthermore, the efficiency roll-off at high brightness is very minor, showing that efficient blue single-layer OLEDs at practical luminance are feasible. At 1000 cd m^{-2}, the corresponding EQE of 15.5% for the inverted OLED is even higher than the reported value (10.8%[28]) for a multilayer OLED with the same emitter. On the other hand, the conventional single-layer OLED shows a maximum EQE of 8.7%, which is expected based on the outcoupling simulations. The EL spectra are shown in **Figure 3.11 c)** with maxima at 490 nm.

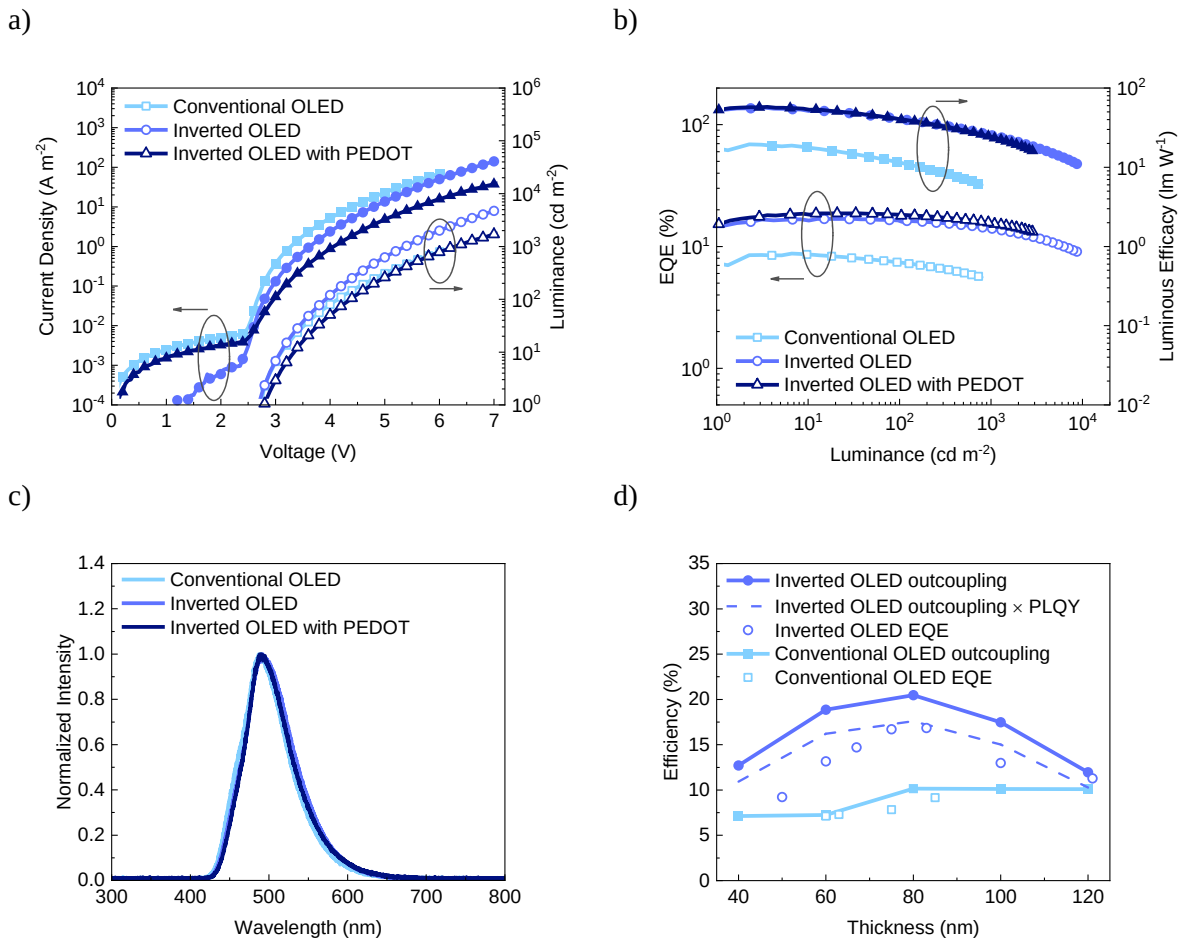

Figure 3.11: Device performance of single-layer 2tCz2CzBN OLEDs. a) Current density–voltage and luminance–voltage characteristic, b) corresponding EQE and current efficiency as a function of luminance, c) electroluminescence spectra, d) emissive layer thickness-dependent outcoupling efficiency and experimental EQE[1]. Reproduced from reference [1].

Figure 3.11 d) shows that the experimental EQE as a function of emissive layer thickness follows the trend of the simulated optical outcoupling efficiency. Compared to inverted devices, both the measured EQE and simulated outcoupling efficiency of conventional devices are less sensitive to thickness. The main reason is that the recombination zone is always close to the metallic cathode, implying that changing the layer thickness will not induce major changes in outcoupling efficiency. By contrast, in the inverted OLEDs, changing the layer thickness directly shifts the position of the recombination zone with respect to the metal electrode, to which outcoupling is very sensitive. Overall, the agreement between the simulated outcoupling efficiency and the experimental EQE as a function of layer thickness confirms the calculated position of the recombination zone. The device-performance parameters of all OLEDs in this study are summarized in **Table 3.3**.

Table 3.3: Device performance of OLEDs based on different TADF emitters[1].

Device	V_{on}[b)] [V]	EQE_{max}[c)] [%]	EQE[d)] [%]	CE_{max}[e)] [cd A^{-1}]	PE_{max}[f)] [lm W^{-1}]	λ_{EL}[g)] [nm]
CzDBA inverted	2.6	15.5	14.0	53.2	50.2	560
DMAC-BP conventional	2.6	8.9	5.7	27.6	32.7	511
DMAC-BP inverted	2.6	15.9	14.5	52.8	53.2	518
2tCz2CzBN conventional	2.7	8.7	\	17.9	18.7	490
2tCz2CzBN inverted	2.7	16.9	14.1	52.3	57.0	490
2tCz2CzBN inverted[a)]	2.8	18.7	15.5	58.1	57.7	490

a)Inverted OLED based on 2tCz2CzBN with an additional 40 nm PEDOT layer on top of the ITO cathode, **b)** Turn-on voltage (V_{on}) at 1 cd m^{-2}, **c)** External quantum efficiency (EQE) and at maximum and **d)** at 1000 cd m^{-2}, **e)** Current efficiency (CE) and **f)** Power efficiency at their maximum, **g)** EL peak.

3.4 Device stability analysis

As we have demonstrated that efficient single-layer OLEDs are feasible, even with imbalanced charge transport of the emitter, a question that may arise is whether imbalanced charge transport would affect the operational stability. Fundamentally, single-layer OLEDs have shown increased lifetimes with respect to multilayer OLEDs, due to a broadened recombination zone.

a) b)

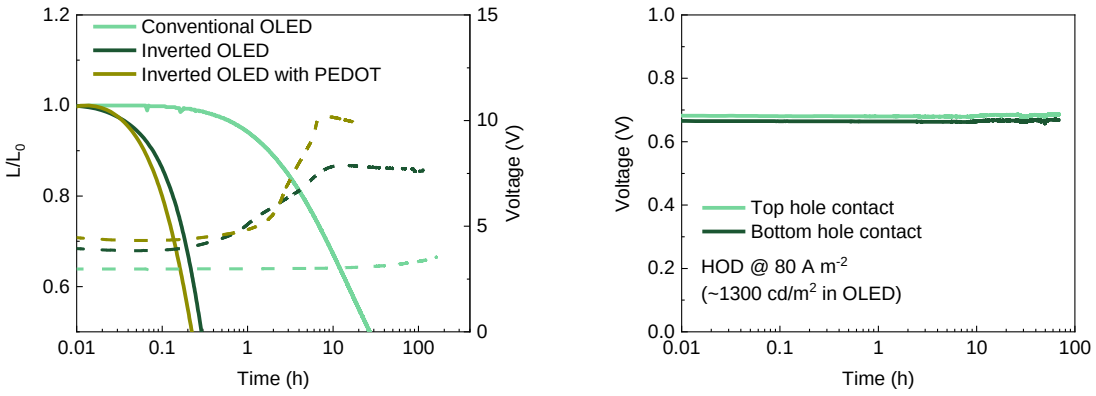

Figure 3.12: Device lifetime of DMAC-BP in single-layer conventional (70 nm) and inverted (70 nm) OLEDs. a) stressed at a constant current with initial luminance of 1000 cd m^{-2}, dush lines represent the increasing operating voltage, b) hole-only device (HOD) of DMAC-BP (90 nm), stressed at constant current density (80 A m^{-2}) which is equivalent to a luminance of 3300 cd m^{-2} for an inverted OLED and 1300 cd m^{-2} for a conventional OLED[1]. Reproduced from reference [1].

The lifetime measurements on DMAC-BP as shown in **Figure 3.12 a**) indicate that in the conventional device structure, the stability is improved compared to reported multilayer devices, despite

imbalanced transport. In the inverted devices, the electron-injection layer is limiting the lifetime. This is apparent from the fact that the voltage remains stable until at least LT_{50}. Since these OLEDs are hole-dominated devices, a stable voltage means that the hole current is unaffected, implying that the degradation is either due to reduced electron injection or reduced electron transport.

As the only difference between the conventional and the inverted device is the used electron-injection layer, this is the source of the faster degradation in the inverted OLED. When stressed under constant current, reduced electron injection will hardly affect the driving voltage, since the current is mainly carried by holes from the start. The increase in voltage observed near the end of life is most likely caused by the inability of the electron-injection layer to extract holes, possibly due to de-doping of the n-TFB layer. The experiment on the stressing of the hole-only devices, **Figure 3.12 b**), confirms that the hole-contact (MoO_3/C_{60}) is stable under current stress, both in top and bottom configuration, excluding degradation of this contact as the source of the voltage rise near the end of life in OLEDs. The inverted devices with an extra PEDOT:PSS layer are similarly stable to the inverted OLEDs without PEDOT:PSS. The observed difference is not considered significant and within the experimental variation of these results.

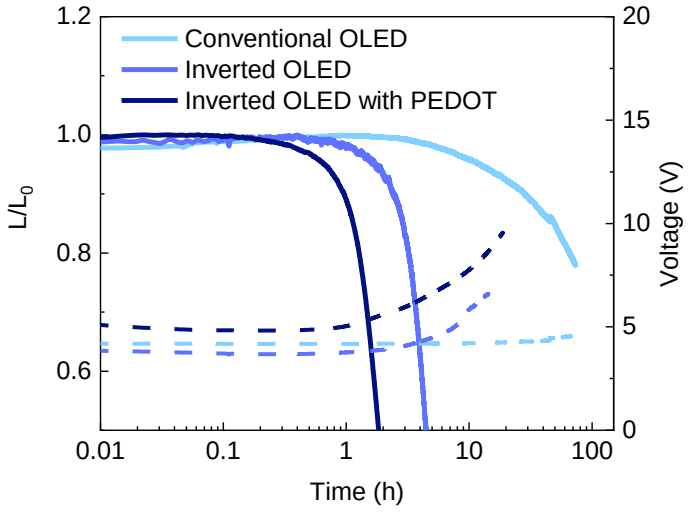

Figure 3.13: Device lifetime of 2tCz2CzBN in single-layer conventional (85 nm) and inverted (79 nm) OLEDs stressed at a constant current, at an initial luminance of 100 cd m^{-2}.[1] Reproduced from reference [1].

It is demonstrated that the conventional OLED based on DMAC-BP have a lifetime that is a factor ~2.5 higher than a previously reported multilayer OLED based on a non-doped DMAC-BP emissive layer[22]. Similar results have been proven with blue OLEDs as shown in **Figure 3.13**. Therefore, as the electron-injection layer for the inverted structure is not yet optimized for stability, the lifetime of these devices is reduced. Nevertheless, it is apparent from the conventional single-layer OLEDs that imbalanced transport and the resulting recombination zone still leads to stability advantages compared to multilayer devices, demonstrating that the single-layer concept is a promising route towards more stable OLEDs.

3.5 Experiment

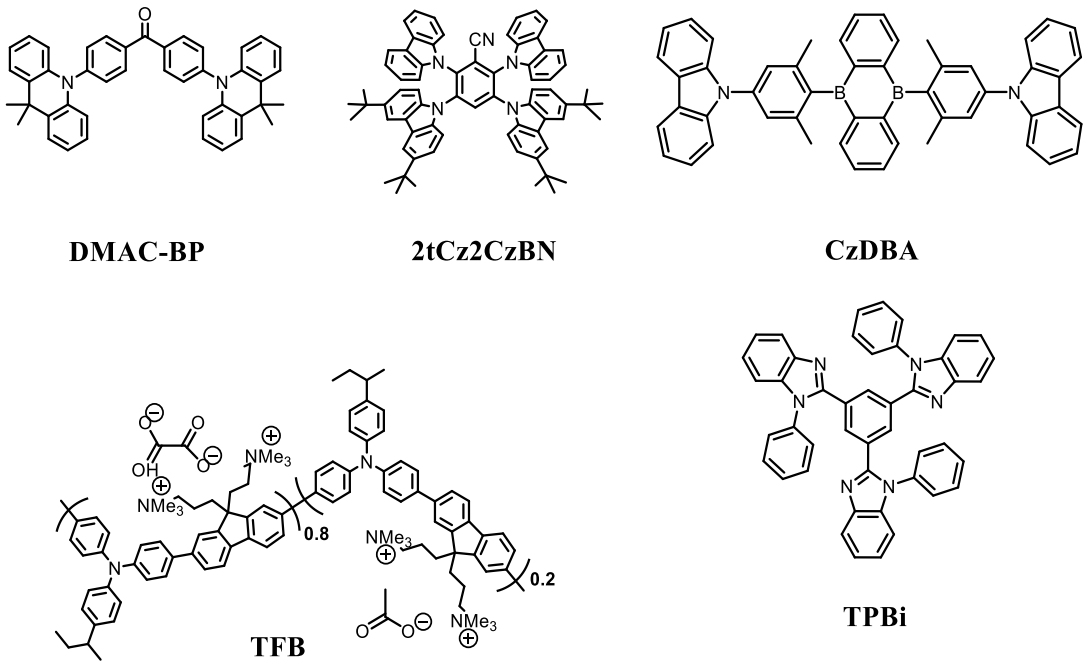

Figure 3.14: Chemical structure of organic compounds used in this work[1].

Pre-patterned ITO-covered glass substrates were cleaned with detergent solution and ultrasonicated in acetone and subsequently in isopropyl alcohol for 5 min. The substrates were then heated at 140 °C for 10 min and subsequently treated with UV-ozone for 20 min. For some devices, PEDOT:PSS (Heraeus AI 4083) layers of 45 nm were spin coated on the ITO substrates, which were annealed at 140 °C for 10 min subsequently. For inverted OLEDs, a solution of n-TFB was prepared using a TFE(2,2,2-trifluoroethanol):OFP(2,2,3,3,4,4,5,5-octafluoro-1-pentanol) solvent mixture in a volume ratio of 3:1, which was spin cast in a nitrogen-filled glovebox to form a film with a thickness of 14 nm, on top of either ITO or PEDOT:PSS. Organic tunneling interlayers of 4 nm (C_{60} and TPBi) were thermally evaporated under high vacuum. Layers of MoO_3 (10 nm), Ba (5 nm) and Al (100 nm) were thermally evaporated under high vacuum. For electron-only devices, glass substrates were used, with a thermally evaporated Al (30 nm) bottom electrode.

Table 3.4: Device structures of based on different TADF emitters[1].

	Device structures
Conventional OLED structure	ITO/ PEDOT:PSS (40 nm)/ MoO_3 (7 nm)/ C_{60} (4 nm)/ emissive layer/ TPBi (4 nm)/ Ba (5 nm)/Al (100 nm)
Inverted OLED structure	ITO/ n-TFB (14 nm)/ TPBi (4 nm)/ emissive layer/ C_{60} (4 nm)/ MoO_3 (10 nm)/Al (100 nm) ITO/ PEDOT:PSS (40 nm)/ n-TFB (14 nm)/ TPBi (4 nm)/ emissive layer/ C_{60} (4 nm)/ MoO_3 (10 nm)/Al (100 nm)
Electron only device	Al (30 nm)/ active layer/ TPBi (4 nm)/Ba (5 nm)/Al (100 nm)
Hole only device	ITO/ PEDOT:PSS (40 nm)/ MoO_3 (7 nm)/ C_{60} (4 nm)/ active layer/ C_{60} (4 nm)/ MoO_3 (10 nm)/Al (100 nm)

Electrical characterization was carried out under nitrogen atmosphere with a Keithley 2400 source meter and light output was recorded with a Si photodiode with NIST-traceable calibration, with a detector area (1 cm^2) larger than the emitting area of the OLED[29] (0.16 cm^2). The photodiode was placed close to (but not in contact with) the OLED to capture all photons emitted in a forward hemisphere. To avoid any light detection emitted from the substrate edges, the edges were masked by the sample holder and the substrate size (3 × 3 cm^2) was considerably larger than the photodetector area. The EQE, the luminance and power efficiency were calculated from the measured photocurrent, the device current, and the electroluminescence spectrum. Electroluminescence spectra were obtained with a USB4000-UV–VIS-ES spectrometer.

3.6 Conclusion

In summary, we have demonstrated a strategy to design highly efficient single-layer OLEDs despite imbalanced charge transport of the emitter. For the most common case of a hole-dominated emitter, this is achieved with a newly designed inverted device structure. Due to the superior hole transport, the emission zone is situated far away from the metallic hole-injecting electrode, thereby enhancing light extraction by suppressing photon coupling into SPP modes. A blue single-layer OLED with an EQE of 18.7% with small roll-off at high brightness was demonstrated, on par with multilayer OLEDs. This demonstrates that balanced transport is not a prerequisite to realize highly efficient single-layer blue OLEDs, extending the single-layer OLED concept to a wide range of TADF emitters of all colors, without the need for high-triplet-energy blocking and host layers.

Reference

1. Tan, X. *et al.* Inverted device architecture for high efficiency single-layer organic light-emitting diodes with imbalanced charge transport. *Nat. Commun.* **15**, 1–7 (2024).
2. Kotadiya, N. B., Mondal, A., Blom, P. W. M., Andrienko, D. & Wetzelaer, G.-J. A. H. A window to trap-free charge transport in organic semiconducting thin films. *Nat. Mater.* **18**, 1182–1186 (2019).
3. Barnes, W. L., Dereux, A. & Ebbesen, T. W. Surface plasmon subwavelength optics. *Nature* **424**, 824–830 (2003).
4. Li, Y., Van der Zee, B., Wetzelaer, G. J. A. H. & Blom, P. W. M. Optical Outcoupling Efficiency in Polymer Light-Emitting Diodes. *Adv. Electron. Mater.* **7**, 1–8 (2021).
5. Lu, L. P., Kabra, D., Johnson, K. & Friend, R. H. Charge-carrier balance and color purity in polyfluorene polymer blends for blue light-emitting diodes. *Adv. Funct. Mater.* **22**, 144–150 (2012).
6. Kotadiya, N. B., Blom, P. W. M. & Wetzelaer, G. J. A. H. Efficient and stable single-layer organic light-emitting diodes based on thermally activated delayed fluorescence. *Nat. Photonics* **13**, 765–769 (2019).
7. Chen, G. *et al.* Efficient organic light emitting diodes using solution-processed alkali metal carbonate doped ZnO as electron injection layer. *Front. Chem.* **7**, 1–9 (2019).
8. Zhou, Y. *et al.* A Universal Method to Produce Low–Work Function Electrodes for Organic Electronics. **873**, 327–332 (2012).
9. Kim, Y. H. *et al.* Polyethylene imine as an ideal interlayer for highly efficient inverted polymer light-emitting diodes. *Adv. Funct. Mater.* **24**, 3808–3814 (2014).
10. Fukagawa, H. *et al.* Long-Lived Flexible Displays Employing Efficient and Stable Inverted Organic Light-Emitting Diodes. *Adv. Mater.* **30**, (2018).
11. Lin, X. *et al.* Beating the thermodynamic limit with photo-activation of n-doping in organic semiconductors. *Nat. Mater.* **16**, 1209–1215 (2017).
12. Tang, C. G. *et al.* Multivalent anions as universal latent electron donors. *Nature* **573**, 519–525 (2019).
13. Wang, L. X. *et al.* Double-type-I charge-injection heterostructure for quantum-dot light-emitting diodes. *Mater. Horizons* **9**, 2147–2159 (2022).
14. Ang, M. C. Y. *et al.* Bulk ion-clustering and surface ion-layering effects on work function of self-compensated charged-doped polymer semiconductors. *Mater. Horizons* **7**, 1073–1082 (2020).
15. Ang, M. C. Y. *et al.* Spectator cation size effect on the work function and stability of self-compensated hole-doped polymers. *J. Mater. Chem. C* **8**, 124–131 (2019).
16. Kotadiya, N. B. *et al.* Universal strategy for Ohmic hole injection into organic semiconductors with high ionization energies. *Nat. Mater.* **17**, 329–334 (2018).
17. Cnossen, G., Drabe, K. E. & Wiersma, D. A. Fluorescence properties of submonolayers of rhodamine 6G in front of a mirror. *J. Chem. Phys.* **98**, 5276–5280 (1993).
18. Tsutsui, T., Aminaka, E., Lin, C. P. & Kim, D. U. Extended molecular design concept of

molecular materials for electroluminescence: sublimed–dye films, molecularly doped polymers and polymers with chromophores. *Philos. Trans. R. Soc. London. Ser. A Math. Phys. Eng. Sci.* **355**, 801–814 (1997).

19. Wetzelaer, G.-J. A. H. & Blom, P. W. M. Comment on "Enhanced Charge Selectivity via Anodic-C 60 Layer Reduces Nonradiative Losses in Organic Solar Cells". *ACS Appl. Mater. Interfaces* **14**, 7523–7526 (2022).

20. Wu, T. L. *et al.* Diboron compound-based organic light-emitting diodes with high efficiency and reduced efficiency roll-off. *Nat. Photonics* **12**, 235–240 (2018).

21. Liu, W., Kotadiya, N. B., Blom, P. W. M., Wetzelaer, G. J. A. H. & Andrienko, D. Molecular Origin of Balanced Bipolar Transport in Neat Layers of the Emitter CzDBA. *Adv. Mater. Technol.* **6**, 1–7 (2021).

22. Zhang, Q. *et al.* Nearly 100% internal quantum efficiency in undoped electroluminescent devices employing pure organic emitters. *Adv. Mater.* **27**, 2096–2100 (2015).

23. Zhang, D. *et al.* Highly Efficient Full-Color Thermally Activated Delayed Fluorescent Organic Light-Emitting Diodes: Extremely Low Efficiency Roll-Off Utilizing a Host with Small Singlet-Triplet Splitting. *ACS Appl. Mater. Interfaces* **9**, 4769–4777 (2017).

24. Koster, L. J. A., Smits, E. C. P., Mihailetchi, V. D. & Blom, P. W. M. Device model for the operation of polymer/fullerene bulk heterojunction solar cells. *Phys. Rev. B* **72**, 085205 (2005).

25. Li, Y., Kotadiya, N. B., van der Zee, B., Blom, P. W. M. & Wetzelaer, G. A. H. Optical Outcoupling Efficiency of Organic Light-Emitting Diodes with a Broad Recombination Profile. *Adv. Opt. Mater.* **9**, 2001812 (2021).

26. Li, Y. *et al.* Enhanced Operational Stability by Cavity Control of Single-Layer Organic Light-Emitting Diodes Based on Thermally Activated Delayed Fluorescence. *Adv. Mater.* **2304728**, 1–8 (2023).

27. Furno, M., Meerheim, R., Hofmann, S., Lüssem, B. & Leo, K. Efficiency and rate of spontaneous emission in organic electroluminescent devices. *Phys. Rev. B* **85**, 115205 (2012).

28. Zou, S. J. *et al.* High-Performance Nondoped Blue Delayed Fluorescence Organic Light-Emitting Diodes Featuring Low Driving Voltage and High Brightness. *Adv. Sci.* **7**, (2020).

29. Forrest, S. R., Bradley, D. D. C. & Thompson, M. E. Measuring the efficiency of organic light-emitting devices. *Adv. Mater.* **15**, 1043–1048 (2003).

4. Highly efficient pure-blue single-layer organic light-emitting diodes without high triplet energy auxiliary materials

In this chapter, we have investigated efficient pure-blue single-layer OLEDs utilizing DMAC-DPS as TADF emitter, achieving high efficiency without a high-triplet-energy host material. By incorporating a narrow-band terminal emitter (v-DABNA) into a DMAC-DPS matrix, we attained balanced charge transport and superior color purity. Our devices demonstrated a maximum EQE of 21.1% with pure blue emission and reduced roll-off at higher luminance levels. Detailed charge transport analysis revealed that the hole trapping caused by v-DABNA could be regulated via the doping concentration, and 0.5 wt% doping provided optimal charge balance. This work underscores the potential of single-layer hyperfluorescent OLEDs in achieving high efficiency and color purity, providing a pathway to efficient blue OLEDs for commercial applications.

Author Contributions

Gert-Jan A. H. Wetzelaer proposed the project. X.T. designed and carried out the experiments, simulations and wrote the manuscript. Manish Kumar helped with the experiments, Oskar Sachnik shared the PEDOT:PSS:PFI recipe. Gert-Jan A. H. Wetzelaer and Paul W. M. Blom supervised the project.

4.1 Introduction

Recently, a highly efficient sky-blue OLED has been demonstrated in a single-layer structure by our group[1]. Although a virtually 100% internal quantum efficiency was achieved without charge- or exciton-confinement layers, a high-triplet-energy host material was still required. Furthermore, as is common with TADF emitters, the emission spectrum was broad, compromising color purity. To obtain a narrow emission spectrum while still harvesting triplet excitons via TADF, the concept of hyperfluorescence can be used[2,3]. In this concept, the excited stated created on the TADF sensitizer is transferred to a fluorescent terminal emitter with a narrow emission spectrum via Förster resonance energy transfer (FRET). By using a low concentration of the terminal emitter, typically around 1%, short-range Dexter transfer of triplet excitons can be minimized.

However, since the terminal emitter is required to have a smaller gap than the TADF sensitizer does, the addition of a fluorescent emitter is expected to cause charge trapping of either electrons, holes, or both. It is known that charge trapping can drastically reduce the charge transport in organic semiconductors, even if the concentration of charge traps is in the order of only 10^{23} m^{-3}, which equates to a relative concentration of only 0.01-0.1%. Surprisingly, this fundamental issue with hyperfluorescence has been hardly addressed to date. Only a qualitative effect of charge trapping has been reported, with no systematic analysis of the charge transport. It is therefore still unclear to what extent charge trapping affects the device performance in hyperfluorescent OLEDs. In single-layer OLEDs, charge transport solely takes place via the emissive layer, which opens up the opportunity to disentangle the effect of charge trapping from all other effects that normally affect the current flow and charge balance in multilayer OLEDs, such as charge-transport layers, blocking layers, barriers at heterojunctions and charge-injection barriers.

Here, we demonstrate efficient pure-blue single-layer OLEDs based on hyperfluorescence, without the use of high triplet energy auxiliary materials. By using a terminal emitter with a lower ionization energy than the neat TADF matrix, the hole transport is slowed down, which improves the charge balance with respect to the neat TADF emitter, which exhibits hole-dominated transport. By balancing the charge transport upon varying the terminal-emitter concentration, EQEs of above 20% are demonstrated for single-layer pure-blue OLEDs, without host, charge-transport, or charge- and exciton blocking materials.

4.2 Single-layer OLED with DMAC-DPS

As a first step, DMAC-DPS was selected as a blue TADF emitter, which has an electroluminescence peak at 480 nm, and exhibits exceptional concentration insensitive properties, with a PLQY of 0.88 in the neat film[4]. Single-layer OLED based on DMAC-DPS were fabricated with a device structure of ITO/PEDOT:PSS:PFI/DMAC-DPS(92 nm)/Ba(5 nm)/Al (100 nm) (inset in **Figure 4.1 a)**.

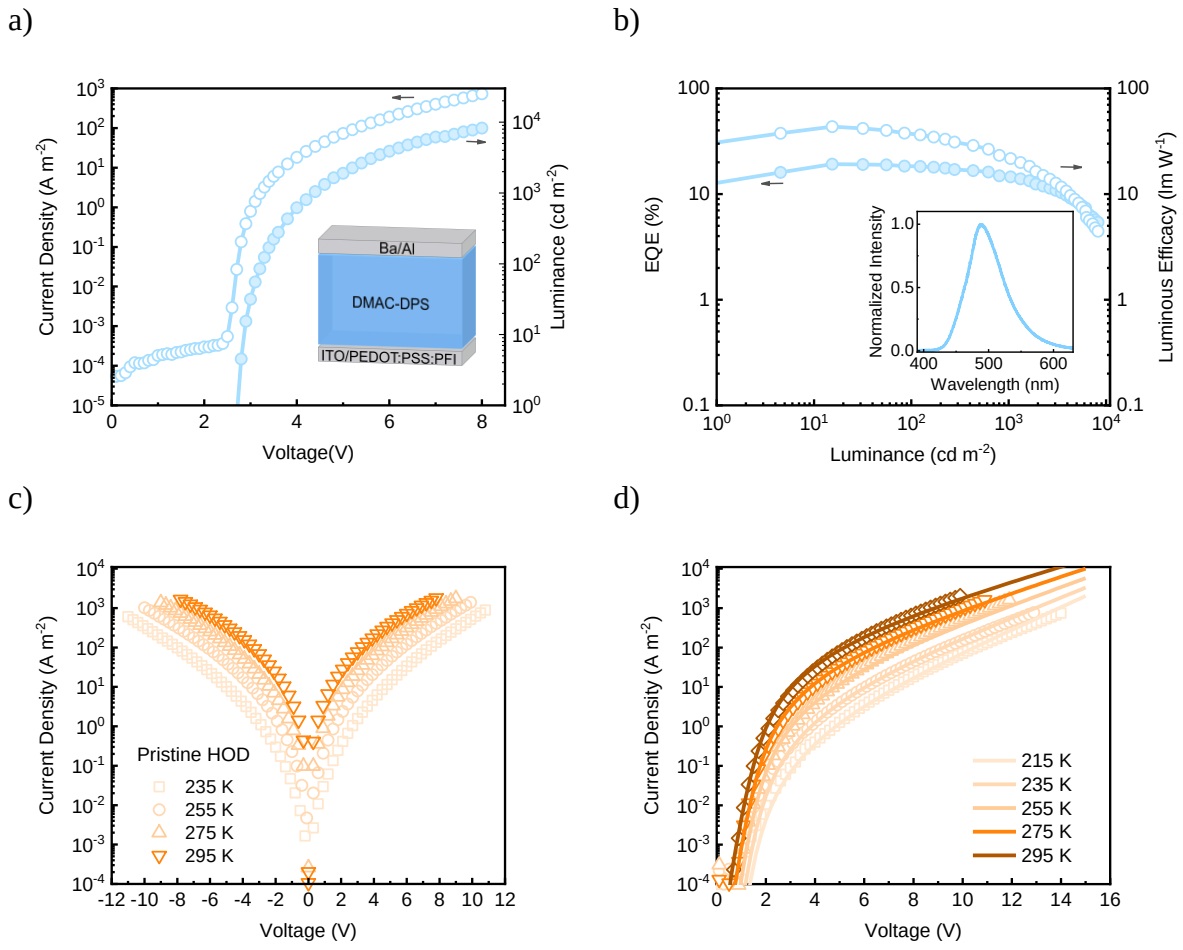

Figure 4.1: Device performance of a single-layer DMAC-DPS OLED with no high E_T materials. a) *J-V-L* characteristics of DMAC-DPS OLED with emissive layer thickness of 92 nm, inserted the device structure. b) EQE and luminous efficacy versus luminance, inserted the electro-luminance spectrum. *J-V* characteristics with temperature dependence of HOD (c) and EOD (d)

with pristine DMAC-DPS at 94 nm thickness, solid lines are fitted with a numerical drift-diffusion model.

Essentially, the active layer (DMAC-DPS) is directly sandwiched between the anode and cathode, without any high triplet energy surrounding layers. The spin-coated PEDOT:PSS:PFI has a high work function of 5.9 eV and forms and ohmic hole contact with DMAC-DPS, which has an IE of 5.9 eV. Our single-layer OLED with a pristine DMAC-DPS emissive layer showed a maximum EQE of 19.2% as shown in **Figure 4.1 b)**, without the use of high E_T functional layers. This is mainly attributed to the efficient charge injection. **Figure 4.1 c)** demonstrates that the bottom contact is indeed ohmic. In addition, the direct charge injection results in low operating voltages, with a turn-on voltage of only 2.8 V, resulting in a high luminous efficacy of 43 lm/W as shown in **Figure 4.1 b)**. For comparison, a reported single-layer OLED with DMAC-DPS neat film showed an EQE_{max} of only 0.11%, which we ascribe to the non-ohmic contacts used. Reported multilayer OLEDs based on neat DMAC-DPS showed an EQE of up to 19.5% by including a high E_T charge and exciton confinement layers, which however increased the operating voltage, resulting in a lower luminous efficacy of 19 lm/W[5]. Our results therefore demonstrate that high efficiency TADF OLEDs are feasible even without any high E_T auxiliary materials.

Table 4.1 Drift-diffusion modeling parameters for hole-only and electron-only devices with a pristine DMAC-DPS layer of 94 nm.

Device	P_t/N_t a) ($\times 10^{22}$ m^{-3})	E_t b) (eV)	σ_t c) (eV)	a d) ($\times 10^{-9}$ m)	σ e) (eV)	μ_0 f) ($\times 10^{-12}$ m^2/Vs)
HOD	0	0	0	1.4	0.15	2.4
EOD	8	0.78	0.1	1.35	0.14	6.9

a) Trap density, b) Trap depth, c) Width of Gaussian trap distribution, d) Lattice constant EGDM, e) DOS variance EGDM, f) Mobility at 295 K.

To assess why this very simple blue OLED performs so well, it is necessary to characterize the charge transport. In a single-layer OLED, only the charge transport of the emitter is responsible for the charge balance. Therefore, we fabricated hole-only (HOD) and electron-only (EOD) devices with ohmic contacts sandwiching the pristine DMAC-DPS film. As shown in **Figure 4.1 d)**, the charge transport was quantified by fitting the temperature-dependent currents with drift-diffusion simulations incorporating the extended Gaussian disorder model for the mobility[6,7], and parameters are listed in **Table 4.1**. The zero-field and zero-density hole mobility amounted to 2.4×10^{-12} m^2 V^{-1} s^{-1}. The electron mobility at zero field and zero-density amounted to 6.9×10^{-12} m^2 V^{-1} s^{-1}, which is comparable to the hole mobility. However, the electron transport is further hindered by deep electron traps with a density of 8×10^{22} m^{-3}, which makes DMAC-DPS a hole-dominated emitter. In **Figure 4.2**, the measured *J-V* characteristics of the single-carrier devices are compared. At high voltages, the hole and electron current are close to each other, indicating quite balanced charge transport[8]. To summarize, the high EQE of the single-layer DMAC-DPS OLEDs can be explained by the ohmic charge injection and the mobility are fairly balanced, but the presence of electron trapping demonstrates that there is still room for improvement with regard to charge balance.

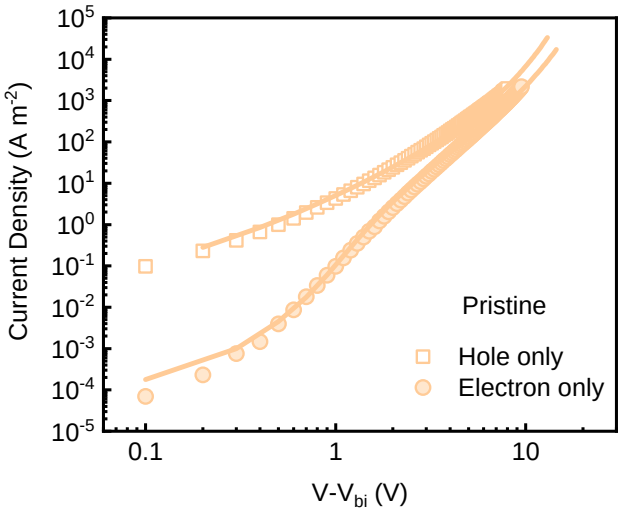

Figure 4.2: Current density-voltage characteristics at 295 K for hole-only and electron-only devices with a pristine DMAC-DPS layer of 94 nm. For electron-only devices, the built-in voltage equals 0.5 V, while hole-only devices are symmetric and thus have no built-in voltage. Solid lines are fitted with a numerical drift-diffusion model.

4.3 Single-layer OLED with pure blue emission

4.3.1 Device concept

The demonstration of 19% EQE achieved in a single-layer blue OLED shows that high efficiency is feasible without any high E_T host materials. However, the EL spectrum of DMAC-DPS has a FWHM of 62 nm, which compromises color purity. Therefore, we incorporated v-DABNA as a narrow-band blue terminal emitter[9], which has a singlet excited state S_1 of 2.65 eV and can be excited by energy transfer from DMAC-DPS (S_1 = 2.7 eV)[4]. v-DABNA is a multi-resonance TADF emitter with a reported photoluminescence peak at 468 nm and a FWHM of 14 nm in toluene solution[9]. For a single-layer OLED based on DMAC-DPS doped with a small concentration of v-DABNA, the energy-level diagram is shown in **Figure 4.3**. Since the IE of v-DABNA (5.4 eV)[9] is lower than the IE of DMAC-DPS (5.9 eV)[4], it is expected that this terminal emitter would cause hole trapping, while the electron transport should not be affected based on the energy levels.

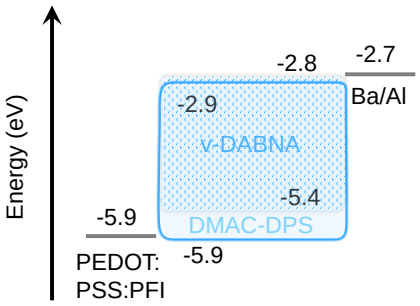

Figrue 4.3： The energy level diagram of related materials in single–layer hyperfluorescence OLED.

4.3.2 Hole trapping analysis

To verify this experimentally, we fabricated HODs and EODs of DMAC-DPS with different doping concentrations of v-DABNA. It is immediately clear that the hole current drops by a factor of 20, just by incorporating 0.5% of v-DABNA. This is a clear sign of hole trapping on the v-DABNA molecules. By increasing the v-DABNA concentration, the hole current drops further, which is expected when the hole-trap concentration is increased. To quantify the amount of hole traps due to the incorporation of v-DABNA, the hole currents were fitted with drift-diffusion simulations, based on the charge-transport parameters for pristine DMAC-DPS, with additional hole traps **(Table 4.2)**. The extracted hole-trap densities are displayed in the inset of **Figure 4.4**.

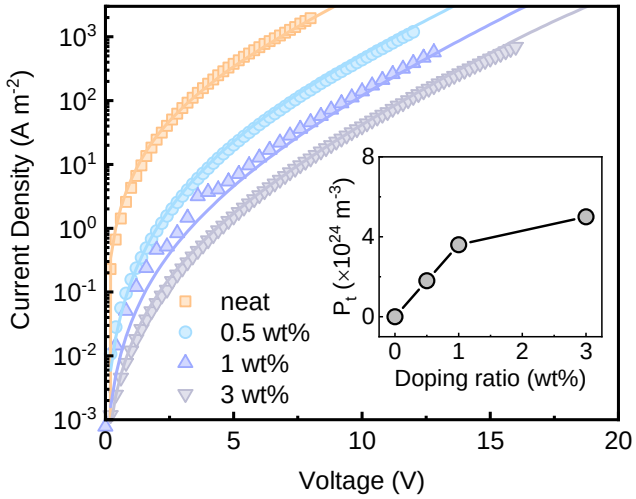

Figure 4.4: Charge transport in DMAC-DPS as a function of the v-DABNA doping concentration. Current density-voltage characteristics of HODs at different doping concentrations (symbols). Solid lines are the corresponding drift-diffusion simulations, with the use hole-trap concentration displayed in the inset. The thickness of the active layers of both HODs and EODs are 94 nm (0 wt%), 101 nm (0.5 wt%), 101 nm (1 wt%), and 103 nm (3 wt%).

Table 4.2 Drift-diffusion modeling parameters for hole-only devices of v-DABNA. Doped in DMAC-DPS.

Doping concentration	P_t [a] ($\times 10^{24}$ m^{-3})	E_t [b] (eV)	σ_t [c] (eV)	a [d] ($\times 10^{-9}$ m)	σ [e] (eV)	μ_0 [f] ($\times 10^{-12}$ m^2/Vs)
pristine	0	0	0	1.4	0.15	2.4
0.5 wt%	1.8	0.51	0.1	1.4	0.15	2.4
1 wt%	3.6	0.51	0.1	1.4	0.15	2.4
3 wt%	5	0.51	0.1	1.4	0.15	2.4

a) Trap density, b) Trap depth, c) Width of Gaussian trap distribution, d) Lattice constant EGDM, e) DOS variance EGDM, f) Mobility at 295 K at zero field and zero density.

For example, the hole-trap energy was determined to be 0.51 eV which is equivalent to the offset in ionization energy between DMAC-DPS and v-DABNA as indicated in **Figure 4.3**, the hole-trap

density was determined to be 1.8×10^{24} m^{-3} for a doping concentration of 0.5% of v-DABNA. In the simulations, a hopping distance of 1.4 nm for pristine DMAC-DPS was found, which corresponds to a density of states of 3.6×10^{26} m^{-3}. As a result, the extracted trap density 1.8×10^{24} m^{-3} equates to a relative trap concentration of 0.5%, practically the same as the doping concentration of v-DABNA. For a high v-DABNA concentration of 3%, the trap density is lower than expected, which could be due to the tendency of v-DABNA to aggregate[10], implying that one trap site corresponds to multiple v-DABNA molecules.

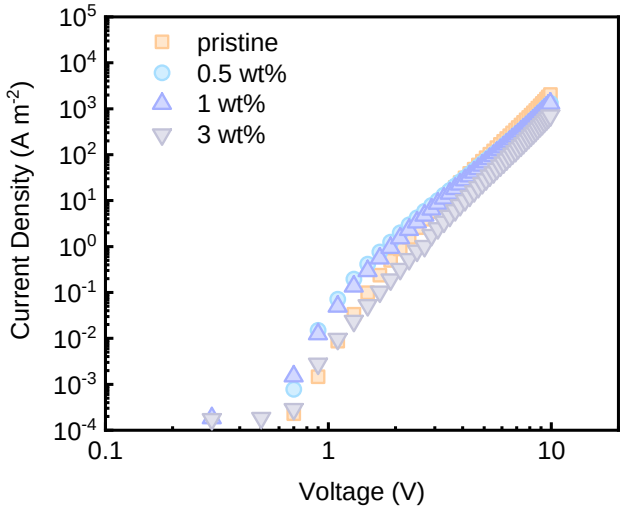

Figure 4.5: Current density- voltage characteristics at 295 K for electron-only devices with different doping ratio of emissive layer, thickness of pristine film is 94 nm, 0.5 wt% of 101 nm, 1 wt% of 101 nm, and 3 wt% of 103 nm.

As hole trapping on v-DABNA is confirmed by analyzing the hole transport in single-carrier devices, the electron transport is now assessed. The electron currents, as displayed in **Figure 4.5**, show only a minor dependence on doping with v-DABNA, which is expected from the lower EA of v-DABNA compared to DMAC-DPS.

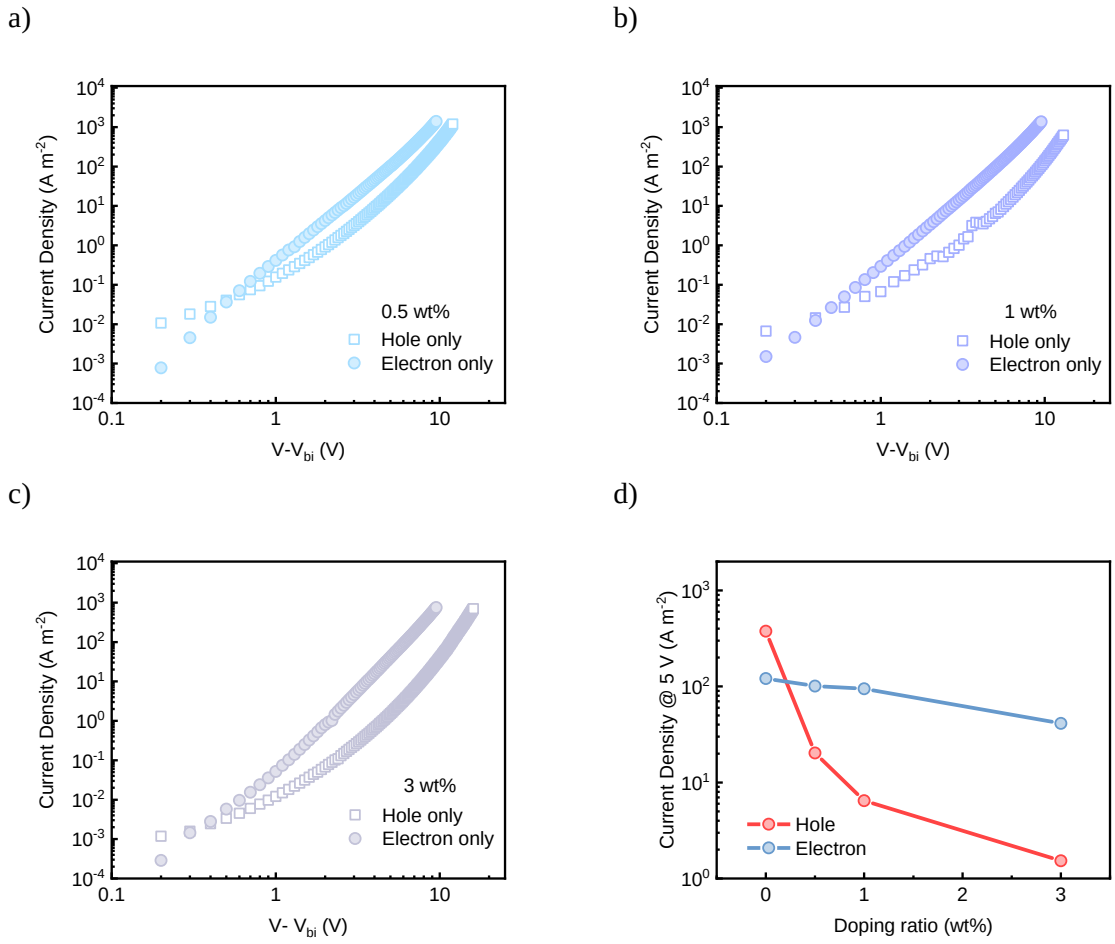

Figure4.6: Comparison of the hole and electron current in DMAC-DPS doped with v-DABNA a) 0.5 wt%, b) 1 wt%, and c)3 wt%. The voltage of the electron-only devices is corrected for a built-in voltage of 0.5 V. d) Current density in HODs and EODs at a voltage of 5 V.

The charge balance comparison of different doping ratios is showed in **Figure 4.6 a-c)**, and **d)** shows the electron and hole current density at 5 V, as a function of the doping concentration. While there is a large drop in the hole current densities due to hole trapping on v-DABNA, the electron current density remains stable, which means that v-DABNA has almost no effect on the electron transport of DMAC-DPS. This further implies that doping with v-DABNA can shift the charge balance from hole dominated to electron dominated in DMAC-DPS.

4.3.3 OLED performance

To investigate what effect this change in charge balance has on the OLED performance, single-layer OLEDs of DMAC-DPS with different v-DABNA doping concentrations were fabricated. The *J-V-L* and EQE as function of luminance, and EL spectra are shown in **Figure 4.7**, with the performance parameters listed in **Table 4.3**.

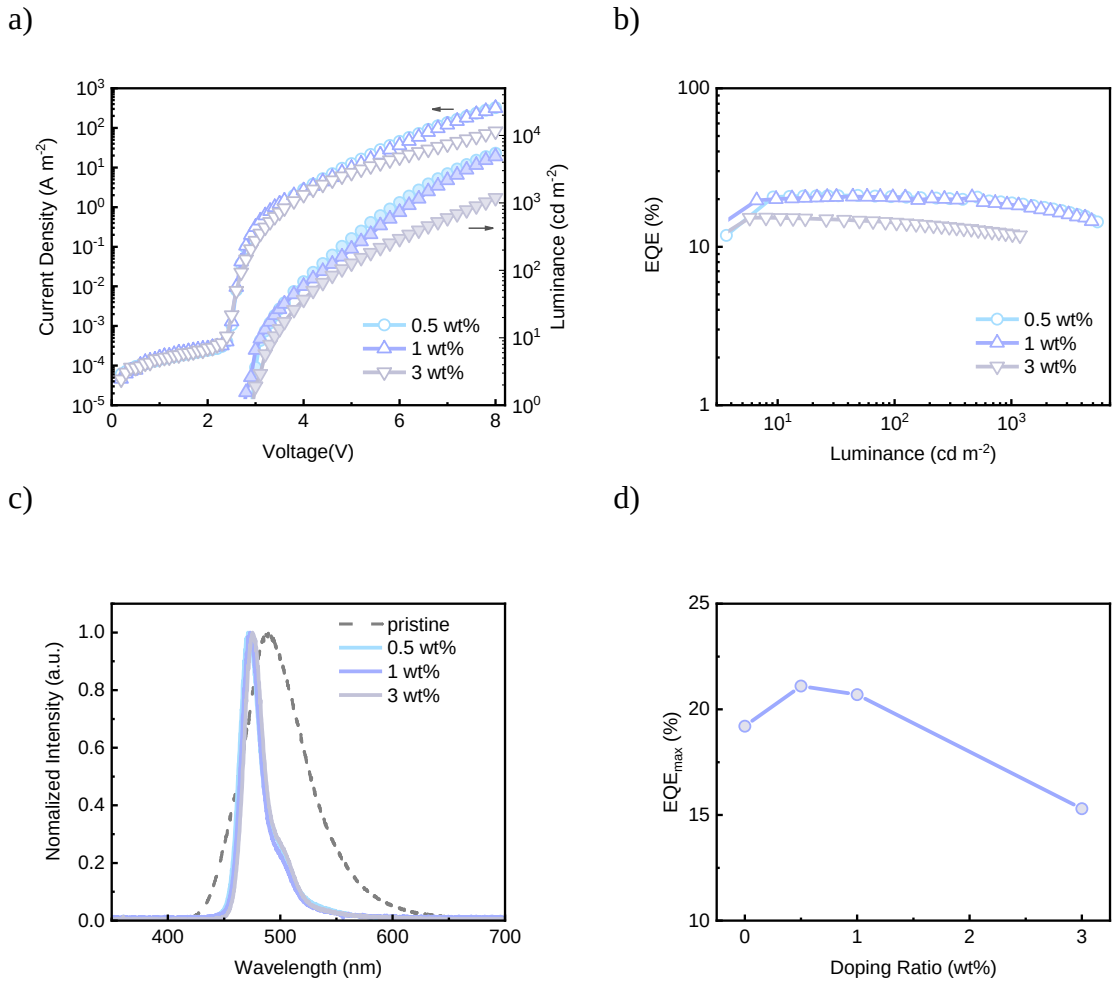

Figure 4.7: OLED performance of hyperfluorescent OLEDs under different doping ratio. a) current density-voltage-luminance characteristics, b) EQE as a function of luminance, c) normalized EL spectra with grey dash of pristine DMAC-DPS EL as reference, d) maximum EQE of OLEDs versus different doping ratios with the neat DMAC-DPS as reference.

Firstly, the hyperfluorescent OLEDs exhibit narrow-band blue emission with an FWHM of 21 nm, confirming full energy transfer to v-DABNA. The 0.5 wt% doped OLED achieves the highest EQE_{max} of 21.1% and remains above 20% at 1,000 cd/m^2, demonstrating both improved efficiency and lower roll-off compared to neat DMAC-DPS. We conjecture that the small roll-off is caused by the high-energy excitons being largely consumed by v-DABNA through radiative decay rather than participating in annihilation processes that reduce the efficiency at high brightness. The EQE characteristics of the OLED with 1% v-DABNA concentrations are rather similar, whereas the EQE decreases to 15.3% for a 3 wt% doping concentration.

Table 4.3 Device performance of single-layer OLEDs with v-DABNA doped in DMAC-DPS.

Doping Ratio	V_{on} [a] (V)	EQE_{max} (%)	EQE_{100} [b] (%)	EQE_{1000} [c] (%)	λ_{EL} [d] (nm)	FWHM [e] (nm)	LT_{50} [f] (min)
pristine	2.8	19.2	18.3	14.5	490	62	0.5
0.5 wt%	2.9	21.1	20.7	18.9	471	21	7
1 wt%	2.8	20.7	20.5	18.2	473	21	18
3 wt%	2.9	15.3	14.2	12.0	475	21	128

a) Turn-on voltage at 1 cd/m^2. b) EQE at 100 cd/m^2. c) EQE at 1000 cd/m^2. d) EL peak wavelength. f) Device lifetime to 50% of the initial luminance under constant current stress of 10 A/m^2, corresponding to a luminance of around 200 cd/m^2.

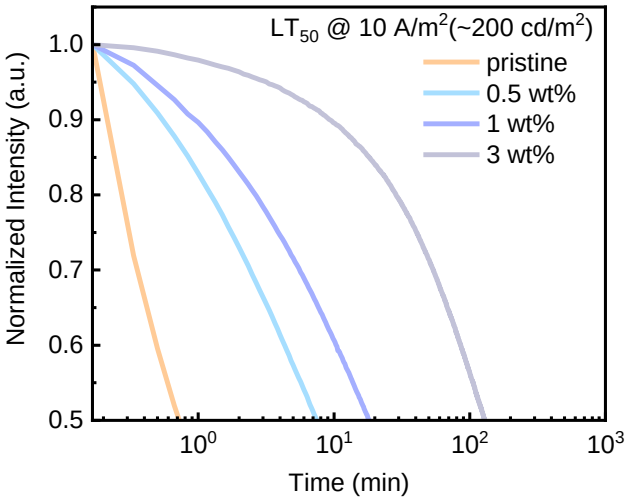

Figure 4.8: Device lifetime measurements of OLEDs with different doping ratio under 10 A/m^2 stressing.

A possible explanation is that at 3 wt% doping ratio, hole trapping becomes so severe that free charges would recombine directly on v-DABNA rather than FRET energy transfer from DMAC-DPS matrix. In this scenario, DMAC-DPS would no longer be electrically excited, which is in line with the operational stability measurements on these OLEDs, as reported in **Table 4.3**. With increasing v-DABNA concentration, the lifetime of the OLEDs improves substantially as shown in **Figure 4.8**. As DMAC-DPS is a very unstable emitter, transferring the excited state to v-DABNA leads to considerable lifetime improvements. At a v-DABNA concentration of 3% though, the lifetime improvement comes at the expense of quantum efficiency and driving voltage, being the result of heavy hole trapping. The slight shift in peak emission wavelength further confirms the tendency of v-DABNA to aggregate at higher doping concentrations[11].

4.4 Experiment

Fabrication: OLED devices were fabricated on pre-patterned ITO on top of glass substrates. The substrates were cleaned by ultrasonication in acetone (5 min) and isopropyl alcohol (5 min) each, followed by UV–ozone treatment (50 min). PEDOT: PSS: PFI blends were prepared by mixing

PEDOT:PSS (CLEVIOS P VP AI 4083) with Nafion in a 1:6:14 ratio and diluted in deionized water (1:1), stirring it overnight. PEDOT:PSS:PFI was spin coated on fresh UV-treated ITO substrates, annealed at 130 °C for 12 min, resulting in films of ~20 nm thickness. The substrates were then transferred to high vacuum chamber for thermal evaporation of the emissive layer under the operation pressure of 2×10^{-6} to 3×10^{-6} mbar. Barium (5 nm) and aluminum (100 nm) were evaporated to build the top electrode. For hole-only devices, a top contact consisting of C_{60} (4 nm), MoO_3 (10 nm) and aluminum (100 nm) was evaporated. For electron-only devices, aluminum (30 nm) was vacuum deposited on cleaned glass substrates then exposed in air for 5 min oxidation, followed by thermal evaporation of the emissive layer and a TPBi (4 nm) interlayer and the barium (5 nm) and aluminum (100 nm) for top electrode.

Table 4.4 Device structure and fabrication.

	Device Structure
OLED	ITO/ PEDOT:PSS:PFI (15 nm)/ emissive layer (~100 nm)/ Ba (5 nm)/Al (100 nm)
EOD	Al (30 nm)/ emissive layer (~100 nm)/ TPBi (4 nm)/ Ba (5 nm)/Al (100 nm)
HOD	ITO/ PEDOT:PSS:PFI (15 nm)/ emissive layer (~100 nm)/ C_{60} (4 nm)/MoO_3 (10 nm)/Al (100 nm)

Measurements: Electrical characterization was carried out in glovebox with a Keithley 2400 source meter and light output was recorded with a Si photodiode with NIST-traceable calibration. The photodiode was placed close to (but not in contact with) the OLED to capture all photons emitted in a forward hemisphere, and no light captured from the substrate edges. The EQE, the luminance and power efficiency were calculated from the measured photocurrent, the device current, and the electroluminescence spectrum. Electroluminescence spectra were obtained with a USB4000-UV–VIS-ES spectrometer.

4.5 Conclusion

In summary, high efficiency and blue emission were simultaneously achieved in a single-layer OLED without high E_T materials. The blue emission was narrowed by doping the terminal emitter v-DABNA into a DMAC-DPS emitter layer, which simultaneously plays the role of pure blue emission and charge balancing. By comparing the device transport under different doping ratios, the hole trapping effect due to the shallower HOMO of v-DABNA has been fully investigated, we succeed in tuning the charge balance of hyperfluorescent OLED in a single layer structure and successfully achieve a pure blue emission OLED with EQE_{max} up to 21%. Aiming for state-of-the-art performance in hyperfluorescent OLEDs, a relatively low doping ratio of the terminal emitters, especially those with shallower HOMO, is a necessity to avoid massive hole trapping obstacle so that the host matrix would still dominate the charge recombination for efficient FRET energy transfer. We believe that device stability is no longer limited by the myriad of high E_T materials, but can be addressed with a stable TADF emitter.

Reference

1. Sachnik, O. *et al.* Single-Layer Blue Organic Light-Emitting Diodes With Near-Unity Internal Quantum Efficiency. *Adv. Mater.* **35**, 1–6 (2023).
2. Nakanotani, H. *et al.* High-efficiency organic light-emitting diodes with fluorescent emitters. *Nat. Commun.* **5**, 4016 (2014).
3. Furukawa, T., Nakanotani, H., Inoue, M. & Adachi, C. Dual enhancement of electroluminescence efficiency and operational stability by rapid upconversion of triplet excitons in OLEDs. *Sci. Rep.* **5**, 8429 (2015).
4. Zhang, Q. *et al.* Efficient blue organic light-emitting diodes employing thermally activated delayed fluorescence. *Nat. Photonics* **8**, 326–332 (2014).
5. Zhang, Q. *et al.* Nearly 100% internal quantum efficiency in undoped electroluminescent devices employing pure organic emitters. *Adv. Mater.* **27**, 2096–2100 (2015).
6. Koster, L. J. A., Smits, E. C. P., Mihailetchi, V. D. & Blom, P. W. M. Device model for the operation of polymer/fullerene bulk heterojunction solar cells. *Phys. Rev. B* **72**, 085205 (2005).
7. Pasveer, W. F. *et al.* Unified Description of Charge-Carrier Mobilities in Disordered Semiconducting Polymers. *Phys. Rev. Lett.* **94**, 206601 (2005).
8. Kotadiya, N. B., Mondal, A., Blom, P. W. M., Andrienko, D. & Wetzelaer, G.-J. A. H. A window to trap-free charge transport in organic semiconducting thin films. *Nat. Mater.* **18**, 1182–1186 (2019).
9. Kondo, Y. *et al.* Narrowband deep-blue organic light-emitting diode featuring an organoboron-based emitter. *Nat. Photonics* **13**, 678–682 (2019).
10. Stavrou, K., Danos, A., Hama, T., Hatakeyama, T. & Monkman, A. Hot Vibrational States in a High-Performance Multiple Resonance Emitter and the Effect of Excimer Quenching on Organic Light-Emitting Diodes. *ACS Appl. Mater. Interfaces* **13**, 8643–8655 (2021).
11. Kim, H. S. *et al.* Toward highly efficient deep-blue OLEDs: Tailoring the multiresonance-induced TADF molecules for suppressed excimer formation and near-unity horizontal dipole ratio. *Sci. Adv.* **9**, 1–9 (2023).

List of Publications

1. Tan, X., Dou, D., Chua, L. L., Png, R. Q., Congrave, D. G., Bronstein, H., ... & Wetzelaer, G. J. A. (2024). Inverted device architecture for high efficiency single-layer organic light-emitting diodes with imbalanced charge transport. Nature Communications, 15(1), 4107.

2. Tan, X., Kumar, M., Sachnik, O., Blom, P. W., Wetzelaer, G. J. A. Highly efficient pure-blue single-layer organic light-emitting diodes without high triplet energy auxiliary materials. (in preparation)

3. Sachnik, O., Ie, Y., Ando, N., Tan, X., Blom, P. W., & Wetzelaer, G. J. A. (2024). Single-Layer Organic Light-Emitting Diode with Trap-Free Host Beats Power Efficiency and Lifetime of Multilayer Devices. Advanced Materials, 36(16), 2311892.

4. Sachnik, O., Tan, X., Dou, D., Haese, C., Kinaret, N., Lin, K. H., ... & Blom, P. W. (2023). Elimination of charge-carrier trapping by molecular design. Nature Materials, 22(9), 1114-1120.

5. Sachnik, O., Li, Y., Tan, X., Michels, J. J., Blom, P. W., & Wetzelaer, G. J. A. (2023). Single-layer blue organic light-emitting diodes with near-unity internal quantum efficiency. Advanced Materials, 35(26), 2300574.

6. Li, Y., Van der Zee, B., Tan, X., Zhou, X., Wetzelaer, G. J. A., & Blom, P. W. (2023). Enhanced Operational Stability by Cavity Control of Single-Layer Organic Light-Emitting Diodes Based on Thermally Activated Delayed Fluorescence. Advanced Materials, 35(49), 2304728.